Title: Research and Education of CO_2 Separation from Coal Combustion Flue Gases with Regenerable Magnesium Solutions

Final Technical Report

Organization: University of Cincinnati, Cincinnati, OH 45221

PI: Dr. Joo-Youp Lee

Chemical Engineering Program
Department of Biomedical, Chemical, and Environmental Engineering

December, 2013

Project Number: DE-FE0001834

Disclaimer

Abstract

A novel method using environment-friendly chemical magnesium hydroxide ($Mg(OH)_2$) solution to capture carbon dioxide from coal-fired power plants flue gas has been studied under this project in the post-combustion control area. The project utilizes the chemistry underlying the CO_2-$Mg(OH)_2$ system and proven and well-studied mass transfer devices for high levels of CO_2 removal. The major goals of this research were to select and design an appropriate absorber which can absorb greater than 90% CO_2 gas with low energy costs, and to find and optimize the operating conditions for the regeneration step. During the project period, we studied the physical and chemical characteristics of the scrubbing agent, the reaction taking place in the system, development and evaluation of CO_2 gas absorber, desorption mechanism, and operation and optimization of continuous operation. Both batch and continuous operations were performed to examine the effects of various parameters including liquid-to-gas ratio, residence time, lean solvent concentration, pressure drop, bed height, CO_2 partial pressure, bubble size, pH, and temperature on the absorption.

The dissolution of $Mg(OH)_2$ particles, formation of magnesium carbonate ($MgCO_3$), and vapor-liquid-solid equilibrium (VLSE) of the system were also studied. The dissolution of $Mg(OH)_2$ particles and the steady release of magnesium ions into the solution was a crucial step to maintain a level of alkalinity in the CO_2 absorption process. The dissolution process was modeled using a shrinking core model, and the dissolution reaction between proton ions and $Mg(OH)_2$ particles was found to be a rate-controlling step. The intrinsic surface reaction kinetics was found to be a strong function of temperature, and its kinetic expression was obtained. The kinetics of $MgCO_3$ formation was also studied in terms of different pH values and temperatures, and was enhanced under high pH and temperatures.

Notation

a = surface area per unit volume, cm^2/cm^3
A_b = surface area of bubble, cm^2
A' = surface area of particle, cm^2
BFD = block flow diagram
CO_2 = Carbon dioxide
C_{Ai} = interfacial con. of CO_2 in the liquid, mol/cm^3
C_{AT} = conc. of CO_2 in the bulk liquid, mol/cm^3
C_{eq} = equilibrium concentration of total dissolved carbon, mol/cm^3
C_s = equilibrium concentration of $Mg(OH)_2$, mol/cm^3
Ca:S = molar ratio of Ca and S
C/Mg = molar ratio of C and Mg
C_B = concentration of $Mg(OH)_2$ in liquid, mol/cm^3
CSTR = continuous stirred-tank reactor
D_{Al} = liquid diffusivity of the dissolved CO_2, cm^2/sec
D_{Bl} = liquid diffusivity of the dissolved magnesium ions, cm^2/sec
$D_{CO2\ in\ air}$ = diffusivity of CO_2 in the air, cm^2/sec
$D_{CO2\ in\ water}$ = diffusivity of CO_2 in the water cm^2/sec
FGD = flue gas desulfurization
FGDC = flue gas de-carbonation
H_{CO2} = Henry's law constant, atm-cm^3/mole
He_{CO2} = Effective Henry's law constant
H = bed expansion, inch
h_L = Liquid hold-up, inch
K_w = dissociation constant of water, mol/cm^3
K_1, K_2 = dissociation constants for reactions (5.12) and (5.13), mol/cm^3
K_G = overall mass transfer coefficient, mol/cm^2-sec-atm
$k_G = k_g$ = gas-side mass transfer coefficient, mol/cm^2-sec-atm
kA_g = gas-side mass transfer coefficient for CO_2, mol/cm^2-sec-atm
kA_l = liquid-side mass transfer coefficient for CO_2, mol/cm^2-sec-atm
$k_L = k_l$ = liquid-side mass transfer coefficient, mol/cm^2-sec-atm
k_s = dissolution mass transfer coefficient for $Mg(OH)_2$, cm/sec
k_{Bl} = liquid side mass transfer coefficient for Mg^{2+}, cm/sec
MEA = monoethanolamine
MW = mega watts
M_{Mg} = mole of Mg, mole
M_{CO2} = mole of CO_2, mole
M_B = molecular weight of flue gas= 28.1 kg/kgmol
L = height of liquid, cm or liquid flow rate mol/s
L/G = liquid-to-gas ratio, gal liquid/1000acf gas
$(L/G)_{min}$ = minimum liquid-to-gas ratio, gal liquid/1000acf gas
$(L/G)_{act}$ = actual liquid-to-gas ratio, gal liquid/1000acf gas
n_p = number of particles of $Mg(OH)_2$ in container
p_A = concentration of CO_2 in the bulk gas, atm
p_{Ai} = interfacial concentration of CO_2 in the gas, atm
p_{avg} = average CO_2 partial pressure in bubble, atm

p_o = inlet CO_2 partial pressure in the gas stream (bubble), atm
p_{eq} =CO_2 partial pressure at equilibrium, atm
p_{in}, p_{out} = inlet and outlet gas pressure
PRO/II =steady state chemical simulation software
Ppm = part per million
G = gas flow rate, acfm
G_{mf} = gas fluidization velocity, kg/(m^2.s)
Q_g = volumetric flow rate of the gas, cm^3/sec
Q_{in}, Q_{out} = inlet and outlet gas flow rate, cm^3/sec
R = gas constant, atm-cm^3/mol-K
r = r_A = absorption rate, mol/cm^3-sec
S = column cross-sectional area, cm^2
T = temperature, K
TCA= Turbulent contact absorber
TGA-MS= thermo gravimetric analyzer- mass spectrometer
t = time, second
Δt_i = time interval
u = superficial gas velocity, cm/sec
V_L = volume of liquid (without bubbles), cm^3
VLE= vapor liquid equilibrium
VLSE= vapor-liquid-solid equilibrium
x_0 = liquid film thickness, cm
x = distance of dissolved CO_2 travel from gas-liquid interface to the reaction zone, cm
$x_{direction}$ = x direction of the column
$y_{in,i}$, $y_{out,i}$ = inlet and outlet CO_2 volume fraction at during time interval i
z = normalized column height, from 0 to 1
φ = chemical enhancement factor
δ = film thickness around the solid particle, cm
$\delta_{gas\ film}$ = gas film thickness, cm
$\delta_{liquid\ film}$ = liquid film thickness, cm
$K_g a$ = overall mass transfer coefficient, kg mole of solute/(m^3·s·atm)
P = operating pressure, atm
M_B = molecular weight of flue gas, kg/kg mole
H_0 = static bed height, m
L, G = liquid and gas mass flux, kg/(m^2·s)
d_p = packing diameter, m
μ_l = liquid viscosity, kg/(m·s)
ρ_l = liquid density, kg/m^3
g = gravitational acceleration, m/s^2
y_1, y_2 = mole fraction of CO_2 at the inlet and outlet of the absorber

$\overline{(\Delta p)}_{\ln} = \dfrac{\Delta p_{top} - \Delta p_{bottom}}{\ln \Delta p_{top} - \ln \Delta p_{bottom}}$ = log mean pressure difference

Table of Contents

1. Executive Summary

A novel method using environment-friendly chemical magnesium hydroxide ($Mg(OH)_2$) solution to capture carbon dioxide from coal-fired power plants flue gas has been studied under this project in the post-combustion control area. The project utilizes the chemistry underlying the CO_2-$Mg(OH)_2$ system and proven and well-studied mass transfer devices for high levels of CO_2 removal. The major goals of this research were to select and design an appropriate absorber which can absorb greater than 90% CO_2 gas with low energy costs, and to find and optimize the operating conditions for the regeneration step. During the project period, we studied the physical and chemical characteristics of the scrubbing agent, the reaction taking place in the system, development and evaluation of CO_2 gas absorber, desorption mechanism, and operation and optimization of continuous operation. A turbulent contact absorber (TCA) and a bubble column absorber were tested as primary mass-transfer devices for CO_2 gas absorption into $Mg(OH)_2$ solution. Both batch and continuous operations were performed to examine the effects of various parameters including liquid-to-gas ratio, residence time, lean solvent concentration, pressure drop, bed height, CO_2 partial pressure, bubble size, pH, and temperature on the absorption of CO_2. A tanks-in-series (n-CSTR) model was developed to analyze the TCA absorption data. It was found that the TCA reactor used in this research could be adequately modeled with n=7 (i.e., seven CSTR tanks in series). In addition, a rate-limiting step for CO_2 absorption in the TCA was examined. The absorption in the TCA could be divided into two regimes in terms of $Mg(OH)_2$ concentration. From 0.1 to 1 M $Mg(OH)_2$ solution, the CO_2 removal efficiency significantly increased, indicating that the liquid phase is a controlling step. At the concentrations greater than 1 M, the CO_2 removal efficiency was not greatly enhanced under given conditions.

The bubble column absorber results showed that the scrubbing performance heavily depends on gas residence time and bubble size. It was found that >90% CO_2 removal efficiency could be achieved at a liquid-to-gas (L/G) ratio of 120 gal liquid/1000 acf gas, an 8-sec gas residence time, and an average 2–3 mm bubble diameter. A bubble column reactor model was developed for CO_2 removal data analysis based on the assumptions of the laminar flow for the liquid phase and plug flow for the gas phase. The model took into account the physical absorption between CO_2 and water, dissolution of $Mg(OH)_2$ solid particles, diffusion between the gas and liquid phases, and ionic reactions based on the film theory. The overall mass-transfer coefficient, a key designing parameter, is found to be a function of the hydrodynamic parameters, Henry's law constant, CO_2 partial pressure in the gas phase, diffusivities, solid dissolution constant, and temperature. The overall mass-transfer coefficients found from this study are comparable to the values of other scrubbing solvents, such as MEA and ammonia solutions.

The dissolution of $Mg(OH)_2$ particles, formation of magnesium carbonate ($MgCO_3$), and vapor-liquid-solid equilibrium (VLSE) of the system were also studied. The dissolution of

$Mg(OH)_2$ particles and the steady release of magnesium ions into the solution was a crucial step to maintain a level of alkalinity in the CO_2 absorption process. The dissolution process was modeled using a shrinking core model, and the dissolution reaction between proton ions and $Mg(OH)_2$ particles was found to be a rate-controlling step. The intrinsic surface reaction kinetics was found to be a strong function of temperature, and its kinetic expression was obtained. The kinetics of $MgCO_3$ formation was also studied in terms of different pH values and temperatures, and was enhanced under high pH and temperatures. The vapor-liquid-solid equilibrium data was also obtained for the design and operation of CO_2 absorber and desorber.

The CO_2 desorption in rich magnesium slurry solutions was studied to find the best operating conditions. A temperature swing regeneration process has been shown to be effective in recovering CO_2 and regenerating $Mg(OH)_2$. $Mg(HCO_3)_2$ is completely soluble and CO_2 gas is regenerable from bicarbonate ions (HCO_3^-) by raising the temperature during the desorption process. However, a fraction of carbonate ions (CO_3^{2-}) increased with an increase in pH during the desorption process, and it started to form $MgCO_3$, which is rarely soluble in water and energy intensive to regenerate. The $MgCO_3$ formation kinetics was accelerated under high pH and temperature conditions required for the desorption. The separation of magnesium slurry particles followed by desorption of a rich solution at a temperature greater than 100 °C was found to be a reliable regeneration method. The separated slurry is subject to calcination for the regeneration of $Mg(OH)_2$. Two selected adsorbents of activated alumina and a resin of Amberlite have been tried to adsorb the bicarbonate ions in the rich slurry solution, but their adsorption capacities were not significantly high.

2. Magnesium Hydroxide Solution-Based CO_2 Capture System

2.1 Process overview

The magnesium-based flue gas de-carbonation (FGDC) system mainly consists of a scrubber and a stripper. The lean magnesium hydroxide slurry with high pH is introduced to the top of the absorber to contact with the flue gas bubbles which are injected from the bottom of the absorber. As a result, CO_2 gas is captured by the magnesium slurry solution and rich magnesium slurry solution will be sent to the stripper for CO_2 gas recovery and solvent regeneration. Regeneration is accomplished by applying the means of thermal-pressure swing in the stripper. As a result, the concentrated CO_2 gas will be separated and regenerated magnesium solution will be returned to the absorber. A schematic block flow diagram is shown in Figure 2.1.

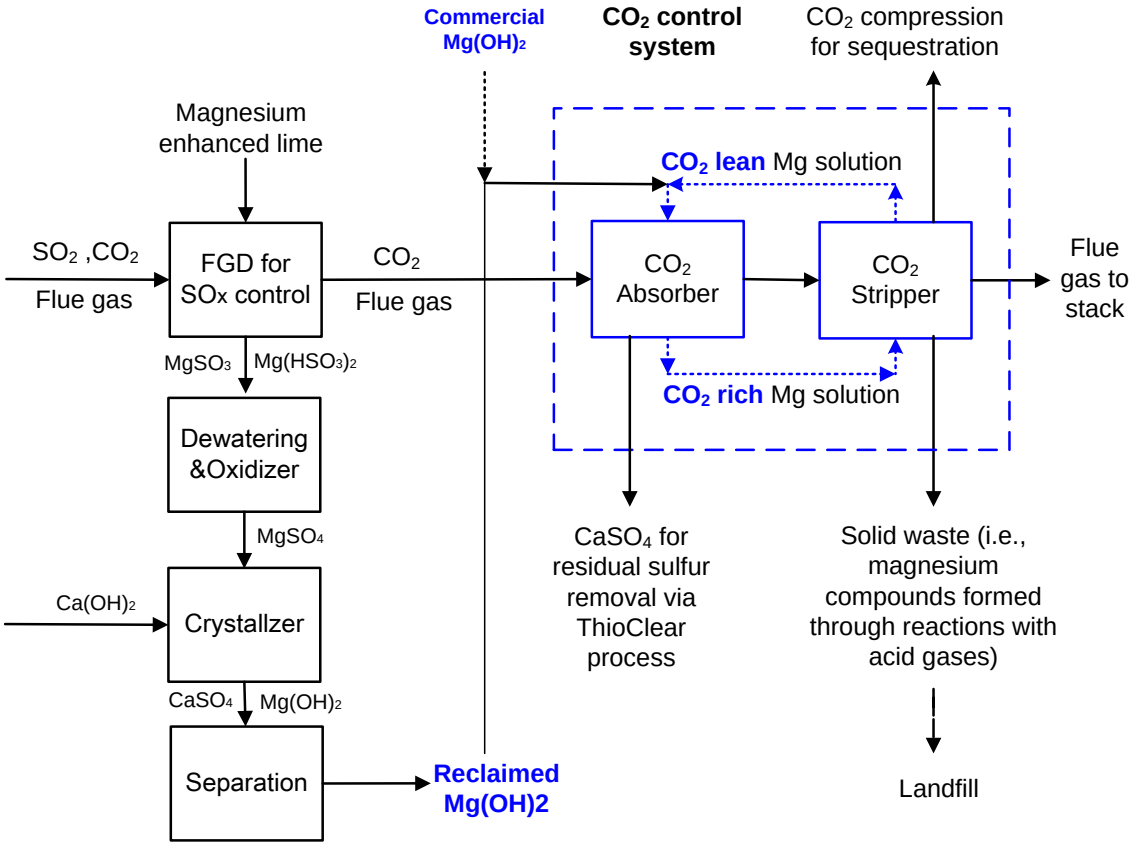

Figure 2.1. Block Flow Diagram (BFD) of $Mg(OH)_2$-based CO_2 separation process.

2.2 Process chemistry

$Mg(OH)_2$-CO_2 system

In comparison with a widely used MEA or ammonia solvent, magnesium hydroxide solution poses several advantages with regards to operation and handling as it is a non-toxic, odorless, non-flammable and less corrosive. The system seeks to utilize the chemistry underlying the $Mg(OH)_2$-CO_2 system and incorporate appropriate mass-transfer devices to achieve a high level of CO_2 removal with a small amount of make-up magnesium solutions. The chemistry for CO_2-$Mg(OH)_2$ absorption and desorption is based on the following reactions taking place in the gas, liquid, and solid phases.

$$\mathbf{H_2O + CO_2(g) \overset{H_{CO2}}{\longleftrightarrow} H_2CO_3^*} \quad (2.1)$$

$$\mathbf{H_2CO_3^* \overset{K_1}{\leftrightarrow} H^+ + HCO_3^-} \quad (2.2)$$

$$\mathbf{HCO_3^- \overset{K_2}{\leftrightarrow} H^+ + CO_3^{2-}} \quad (2.3)$$

$$\mathbf{Mg(OH)_2 \leftrightarrow Mg^{2+} + 2OH^-} \quad (2.4)$$

$$\mathbf{2HCO_3^- + Mg^{2+} \leftrightarrow Mg(HCO_3)_2} \quad (2.5)$$

$$\mathbf{CO_3^{2-} + Mg^{2+} \leftrightarrow MgCO_3} \quad (2.6)$$

Magnesium bicarbonate is completely soluble and has the potential to recover the CO_2 and reclaim the magnesium hydroxide in the stripper when a temperature and pressure swing method applied. The magnesium carbonate is a solid and requires significantly more energy to recover CO_2 gas. However, the precipitation of magnesium carbonate is kinetically controlled and requires longer time to complete than the magnesium solution hydraulic residence time in the system. In addition, magnesium carbon species are highly dependent on the system pH.

Equilibrium calculation for CO_2-water system

Based on Equations (2.1)-(2.3), inorganic carbon concentrations in equilibrium can be written as:

$$[H_2CO_3^*] = \mathrm{H_{CO2}} P_{eq} \quad (2.7)$$

$$[HCO_3^-] = \frac{K_1}{[H^+]} \mathrm{H_{CO2}} P_{eq} \quad (2.8)$$

$$[CO_3^{2-}] = \frac{K_1 K_2}{[H^+]^2} \mathrm{H_{CO2}} P_{eq} \quad (2.9)$$

Therefore, the equilibrium concentration of total dissolved inorganic carbon, C_{eq}, can be written as a sum of these species:

$$C_{eq} = (1 + \frac{K_1}{[H^+]} + \frac{K_1 K_2}{[H^+]^2}) \mathrm{H_{CO2}} P_{eq} \quad (2.10)$$

Also, as CO_2-water system, the electro-neutrality equation can be written as:

$$[H^+] = [OH^-] + [HCO_3^-] + 2[CO_3^{2-}] \quad (2.11)$$

This neutrality equation is only valid for pure CO_2-water system. If any other ions are present in the solution, then these ions need to be considered. Substitute the equilibrium equations and it becomes:

$$[H^+] = \frac{K_w}{[H^+]} + \frac{K_1}{[H^+]} \mathrm{H_{CO2}} P_{eq} + 2\frac{K_1 K_2}{[H^+]^2} \mathrm{H_{CO2}} P_{eq} \quad (2.12)$$

Rearrange as:

$$[H^+]^3 - \left(K_w + \mathrm{H_{CO2}} P_{eq} K_1\right)[H^+] - 2\mathrm{H_{CO2}} P_{eq} K_1 K_2 = 0 \quad (2.13)$$

where K_1, K_2, K_w, and H_{CO2} are temperature-dependent equilibrium constants. Therefore, the equilibrium pH and C_{eq} can be determined once these constants are given.

2.3 Summary of technical challenges

Because our scrubbing agent is slurry, the first challenge is to select and design an appropriate mass-transfer absorber, which can offer a >90% CO_2 removal efficiency without plugging issues. The pH and gas/liquid residence time of the slurry solution can highly affect the dissolution of $Mg(OH)_2$ and the formation of $MgCO_3$. Low pH will help dissolve $Mg(OH)_2$ more efficiently and prevent the formation of carbonate ion, but this will also decrease the CO_2 absorption rate. Long solution residence time will help dissolve $Mg(OH)_2$ particles, but also lead to the undesired precipitation of $MgCO_3$ solid at high pH. Therefore, the second challenge is to adequately control the pH and temperature for the faster dissolution of $Mg(OH)_2$ particles and slower formation of $MgCO_3$ solids during absorption and desorption.

In general, $Mg(OH)_2$ is a relatively safe material in terms of operational and handling issues, and does not present major toxic and hazardous issues. Another major economical and technical consideration is to test whether the reclaimed $Mg(OH)_2$ itself from FGD by-products can energy efficiently capture more than 90% of CO_2 gas in the flue gas. At a typical 500 MW coal-fired power plant, 3,000 ppm SO_2 and 10-12% CO_2 in the flue gases have 219,000 mol/hr and 8,760,000 mol/hr of flow rates, respectively, and are directed to a wet FGD scrubber, requiring 219,000 moles/hr calcium to achieve 99% SO_2 removal. Hence a CO_2 removal capacity of magnesium requires M_{Mg}:M_{CO2}=1:46 for dolomitic limestone, 1:114 for magnesium limestone, 1:600 for high calcium limestone in order to achieve 90% CO_2 removal. Therefore, the third

challenge is to maximize the utilization of Mg in order to make the process self-sustainable by applying reasonable desorption conditions.

Table 2.1 Basis for reclaimed magnesium hydroxide slurry for a typical 500-MW coal-fired power plant with dolomitic limestone-based wet FGD.

Item	Value
Plant electricity output	500 MW
Thermal efficiency	34%
High volatile coal	4% sulfur, 60% carbon
FGD scrubber efficiency	99%
Dolomitic limestone	35-45% $MgCO_3$
SO_2 released	219,000 mol/hr
SO_2 removed (at 99% removal)	217,000 mol/hr
CO_2 released	8,760,000 mol/hr
CO_2 removed (at 90% removal)	7,890,000 mol/hr
$CaCO_3$ required (at Ca:S=1:1 ratio)	217,000 mol/hr
Amount of magnesium available for recovered $Mg(OH)_2$ (at 95% recovery)	207,000 mol/hr
Moles of CO_2 to be removed per mole of magnesium (C/Mg)	46

3. CO_2 Absorption in Turbulent Contact Absorber (TCA)

Turbulent contact absorber (TCA) is a mass-transfer enhanced device in which a bed of low density packing is fluidized by upward flowing gas and downward flowing liquid streams in a counter-current flow mode. This counter-current flow of gas and liquid will fall into the turbulent flow regime and consequently promotes the mass-transfer rate by providing high interfacial mass-transfer rates. Compared with a traditional packed column reactor, TCA has many advantages for gas-liquid-solid mass transfer systems, such as relatively low pressure drop across the absorber, a high interfacial area, an ability to handle large volume of gases, and the suppression of fouling build-up inside the absorber, which is ideal for $Mg(OH)_2$ slurry.

3.1 Design procedure

The CO_2 turbulent contact absorber was designed by following a procedure summarized given below.

Given data:
G: 26.37 acfm = 0.467 mole/s, Wg=0.0132 kg/s, (T = 52 °C, P = 1.01atm),
CO_2 concentration: $y_1 = 0.15$, $y_2 = 0.015$, removal efficiency (η)=90%.

1) Calculation for $(L/G)_{min}$
$(L/G)_{min}$ = 64 gal/1000 acf.

2) Calculation of operating $(L/G)_{act}$
A packed tower is designed to operate at a liquid flow rate, which is typically 30–70% greater than a minimum liquid flow rate (Wark and Warner 1981). A higher liquid flow rate such as twice as high as $(L/G)_{min}$ is typically used to design a turbulent contact absorber (Visvanathan and Leung 1985).
$A = (L/G)_{act.}/(L/G)_{min} = 2$
$(L/G)_{act.}$ = 128 gal/1,000acf = 25.35 mol/mol
L = 11.84 mole/s = 0.008 acf/s = 0.2131 kg/s

3) Flooding mode
There are two operating flooding modes for TCA (Fan, Muroyama et al. 1982).
Type I TCA: fluidization without flooding; Type II TCA: fluidization due to incipient flooding.
Type II mode is typically preferred due to its superior mass-transfer performance (O'Neill, Nicklin et al. 1972). Thus, Type II mode has been selected for the design.

4) Column diameter (D_c in inches)

When a column diameter is selected, the wall effect is an important factor for the consideration. A ratio of column diameter to ball diameter (D_c/d_p) greater than 10 is recommended in the literature (Muroyama and Fan 1985). In our design, a 5-inch internal diameter (D_c) for the absorber has been chosen with the polypropylene hollow balls with 1-cm diameter (d_p) and 0.9 g/cm^3 density.

5) Find liquid (L) and gas (G) mass flux in kg/(m^2·s)
$G = W_g/(\pi D_c^2/4) = 1.05$ kg/(m^2·s), $V_g = 0.98$ m/s
$L = 16.82$ kg/(m^2·s), $V_l = 0.017$ m/s

6) Diameter and density of fluidized ball
A packing density greater than 170 kg/m^3 in the range of 100~1,200 kg/m^3 is required (Vunjak-Novakovic, Vukovic et al. 1987) in order for a turbulent contact absorber to be operated in Type II mode shown in Figure 3.1. The selected polypropylene hollow ball meets the requirements with a 10-mm diameter and a 900 kg/m^3 density.

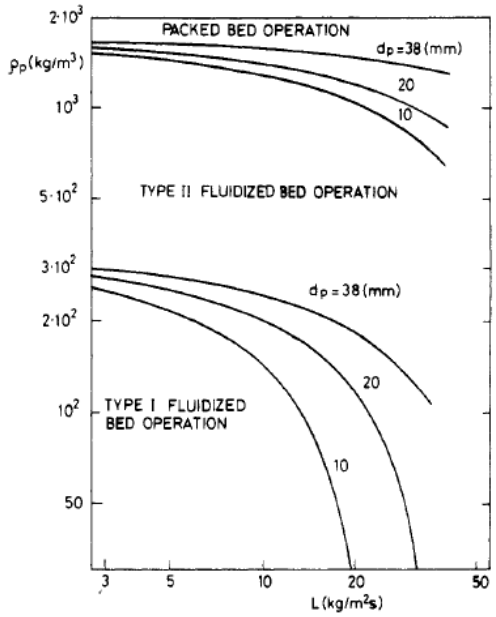

Figure 3.1 Operating flooding zones in TCA. (Vunjak-Novakovic, Vukovic et al. 1987)

7) Calculation of a minimum gas fluidization velocity G_{mf} (Fan, Muroyama et al. 1982)

$$G_{mf} = 526.47 \times d_p^{1.5} \times 10^{-0.0317L} \qquad (3.1)$$

$G_{mf} = 0.16$ kg/(m^2·s)

8) $G > G_{mf}$

Since G = 1.05 kg/(m^2·s) > G_{mf} = 0.16 kg/(m^2·s), the selection of the diameters for the absorber column and fluidized balls is acceptable.

9) Estimation of static bed height, H_0

According to Equation (3.2) (Fan 1989) and (3.3) (Visvanathan and Leung 1985),

$$\frac{M_B P K_g a H_0}{L} = 0.0819\left(\frac{d_p L}{\mu_l}\right)^{0.025}\left(\frac{L^2}{d_p g \rho_l^2}\right)^{-0.169}\left(\frac{L}{G}\right)^{-0.248}\left(\frac{H_0}{d_p}\right)^{0.309} \quad (3.2)$$

$$H_0 = \frac{G(y_1 - y_2)}{K_g a (\Delta p)_{\ln} M_B} \quad (3.3)$$

The equations (3.2) and (3.3) were simultaneously solved for H_0 and K_ga.

H_0 = 2.5 inches

K_ga = 2.1 kgmol of solute/(m^3·s·atm)

10) Liquid hold-up (h_L) and bed expansion (H)

According to Equation (3.4) (Visvanathan and Leung 1985),

$$h_L = 7.326\,\mathrm{Re}^{-0.0591} Fr^{0.4354}\left(\frac{H_0}{D_c}\right)^{-0.4328}\left(\frac{\rho_p}{\rho_l}\right)^{0.0904} + 0.02 \quad (3.4)$$

h_L = 0.57 m^3/m^3

$h_{L0} = h_L$ - 0.02 = 0.55 m^3/m^3

According to Equation (3.5) (Fan, Muroyama et al. 1982),

$$\frac{H}{H_0} = 1 + 0.414\left(\frac{G - G_{mf}}{G_{mf}}\right)^{1.2} \quad (3.5)$$

H = 11” = 0.28 m, H/H_0 = 4.4.

11) Pressure drop in bed

ε_0: initial bed voidage, it is assumed to be 0.5. (0.48~0.50 is recommended (Fan 1989)).

According to Equation (3.6), (Vunjak-Novakovic, Vukovic et al. 1987),

$$\Delta P = \left((1 - \varepsilon_0)\rho_p + h_{L0}\rho_l\right) g H \quad (3.6)$$

ΔP = 2730 Pa = 11” water.

3.2 Experimental set-up

The TCA CO_2 absorption system includes a gas furnace, a heat exchanger, and a CO_2 turbulent contact absorber (TCA) as shown in Figure 3.2. The gas furnace has 125,000 Btu/hr of an input heating rate with an 80+% efficiency, and has been modified to burn propane gas in order to obtain a higher CO_2 gas concentration close to a typical concentration level present in typical coal combustion flue gases. The flue gas with a flow rate of 26.4 acfm and CO_2 gas concentration of 10%, which was fed to the absorber operated at 52 °C when air was injected at a stoichiometric ratio. The flue gas temperature was controlled at 52 °C with a heat exchanger before the absorber, and a fan was installed in order to supply an additional positive pressure to overcome 1~2 inches of a pressure drop across the absorber column. The CO_2 turbulent contact absorber was designed to operate in the Type II fluidized-bed operation regime (Vunjak-Novakovic, Vukovic et al. 1987; Vunjak-Novakovic, Vukovic et al. 1987; Fan 1989) with hollow balls with 1-cm diameter (d_p) and 0.9 g/cm^3 density in the column with a 5-inch internal diameter (D_c). The column diameter was selected in order to minimize the wall effect, and a ratio of column diameter to ball diameter (D_c/d_p) greater than 10 was recommended in the literature.(Muroyama and Fan 1985) The bed height was estimated to be ~1 ft based on the hydrodynamic correlation data available in the literature. (Muroyama and Fan 1985) However, the column was designed to have an adjustable height between 1 and 4 ft (0.30 and 1.22 m) with three sections. Most sensors for pressure, temperature, and flow measurements were installed and calibrated at various locations. A mass balance closure greater than 99.3% was ensured across the absorber. A data acquisition system was also installed to store process data including temperature, CO_2 concentrations, and flow rates. Figure 3.2 shows the experimental setup for TCA test, and Table 3.1 summarizes the experiment conditions.

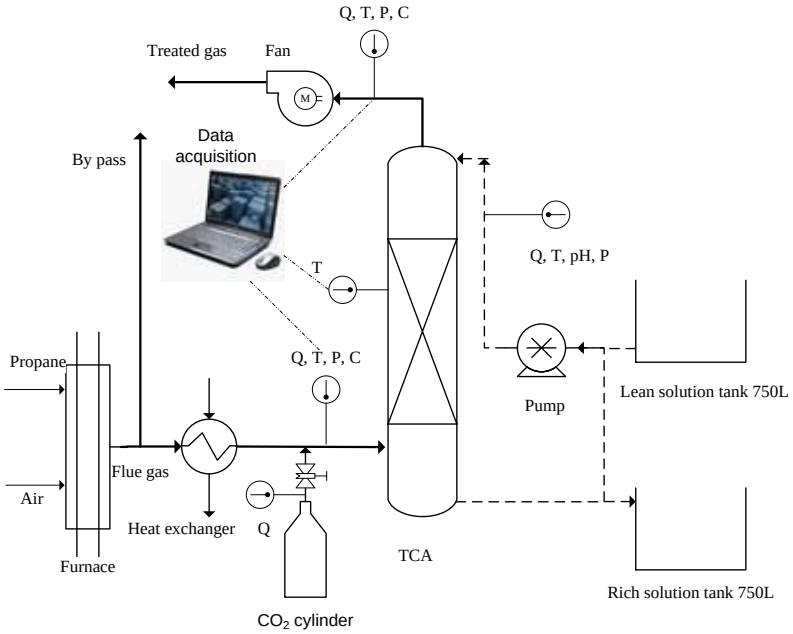

Figure 3.2 Experimental set-up for TCA test.

Table 3.1 Experimental conditions

Terms	Specific values
TCA column Diameter and Height (m)	D=0.13, H=1.5
Solvent (M = mol/L)	Pure water, NaOH (0.1 M, 1 M, 2 M,4 M)
Q gas flow rate (m^3/min)	0.2~1.3
L liquid flow rate (L/min)	1.9~20.8
CO_2 gas concentration (volume %)	7~14
Gas distributor packing height (m)	0.05~0.18
Static bed height (m)	0.4

3.3 Calculation of mass-transfer coefficient

The mass-transfer performance of TCA can be quantified by calculating the value of $K_g a$. K_g is the overall mass-transfer coefficient, and has a unit of kmol/(m^2·s·atm). a is the interfacial area per unit volume, and has a unit of m^{-1}. $K_g a$ can be expressed as:

$$K_g a = \frac{G'}{AP(y-y^*)}\left(\frac{dY}{dZ}\right) \tag{3.7}$$

where G' is the inert gas flow rate (kmol/s); Y is the CO_2 molar ratio; y is the mole fraction; A is the cross section area of the column; and Z is the height of the column. The equation can further be expressed as:

$$K_g a = \frac{G'\left(Y_{in}-Y_{out}\right)}{AZ\overline{\left(\Delta p\right)}_{\ln}} \tag{3.8}$$

where $\overline{\left(\Delta p\right)}_{\ln} = \dfrac{\Delta p_{top}-\Delta p_{bottom}}{\ln \Delta p_{top} - \ln \Delta p_{bottom}} =$ log mean pressure difference.

3.4 Results and discussions

3.4.1 System leak test

A leak test for the absorber column was performed under two operating conditions: 1) The blower was set at the inlet of the absorber which gave a positive pressure to the system; and 2)

The blower was set at the outlet of the absorber which gave a negative pressure to the system. It was confirmed that >97%(wt) of CO_2 mass balance closure could be obtained across the absorption column under varied gas flow rates.

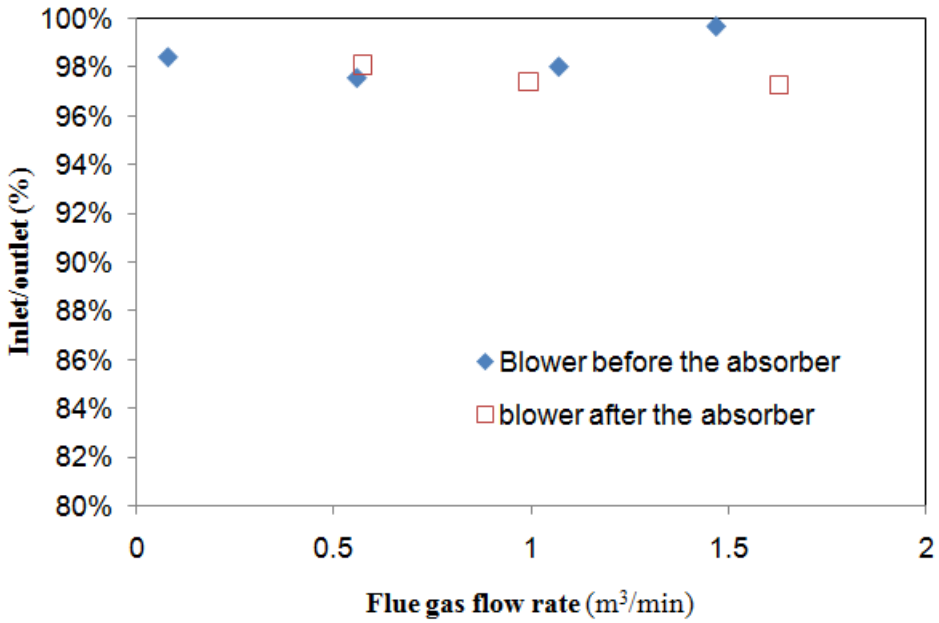

Figure 3.3 System leak test.

3.4.2 Spray nozzle test

A fresh solvent was introduced to the top of the absorber, and a spray nozzle was installed at the inlet of the feed stream for better liquid distribution. Different types of full cone mist spray nozzles with 0, 15, and 60 degree were tested under different L/G ratios. The CO_2 removal performance data showed that a 15-degree nozzle has better performance than a 0-degree nozzle as it can provide finer liquid drops and better liquid distribution. However, a 60-degree nozzle shows a CO_2 gas removal efficiency lower than a 15-degree nozzle even if it provides the finest liquid mist. This is because most of the mists from a 60-degree nozzle were sprayed to the wall of the column, resulting in a decrease in the interfacial area between gas and liquid. It was a typical "wall effect" phenomenon occurring inside the absorber.

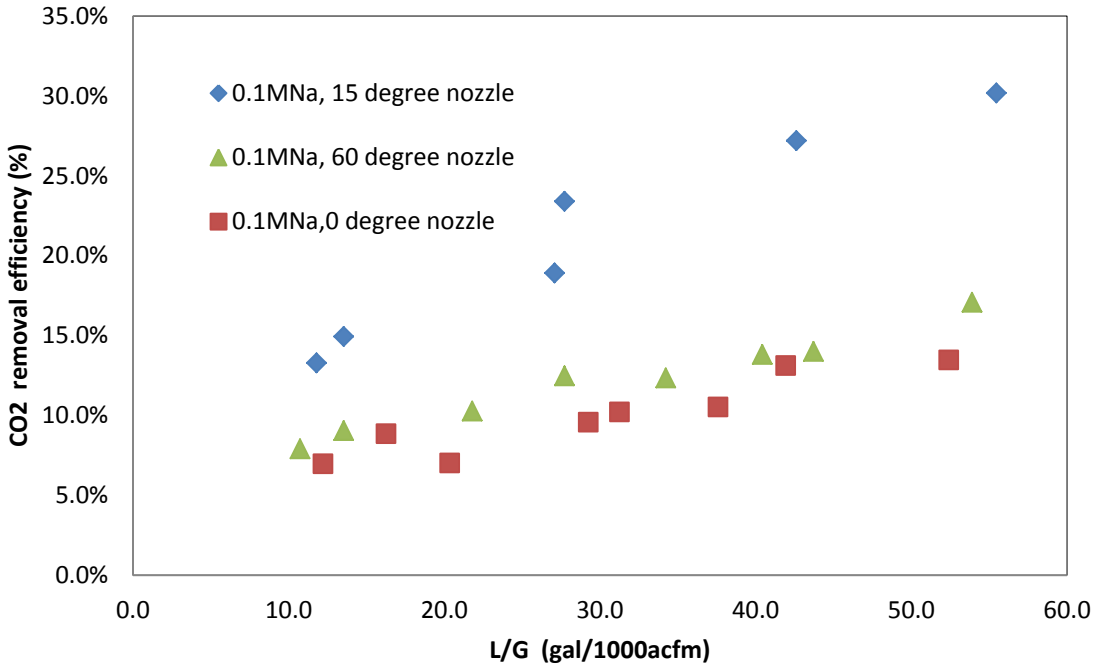

Figure 3.4 Spray nozzle test.

3.4.3 Expanded bed and loading points

The expanded bed height and loading points are crucial parameters in determining a fluidized bed reactor performance. The expanded bed ratio is defined as:

$$\text{Expanded bed ratio} = \frac{\text{Total height of the fluidized bed}}{\text{Static bed height}}$$

Typically, a fluidized bed reactor is recommended operating at an expanded bed ratio between 2 and 5. The ratio is controlled by gas and liquid flow rates. We studied a relationship among the expanded bed ratio, gas flow rate, and liquid flow rate. The results show that an expanded bed height increases as a liquid or gas flow rate increases. For an expanded bed ratio less than 2, an expanded bed ratio and a liquid flow rate are linearly correlated. The expanded bed was found to be more dependent on the gas flow rate than on the liquid flow rate.

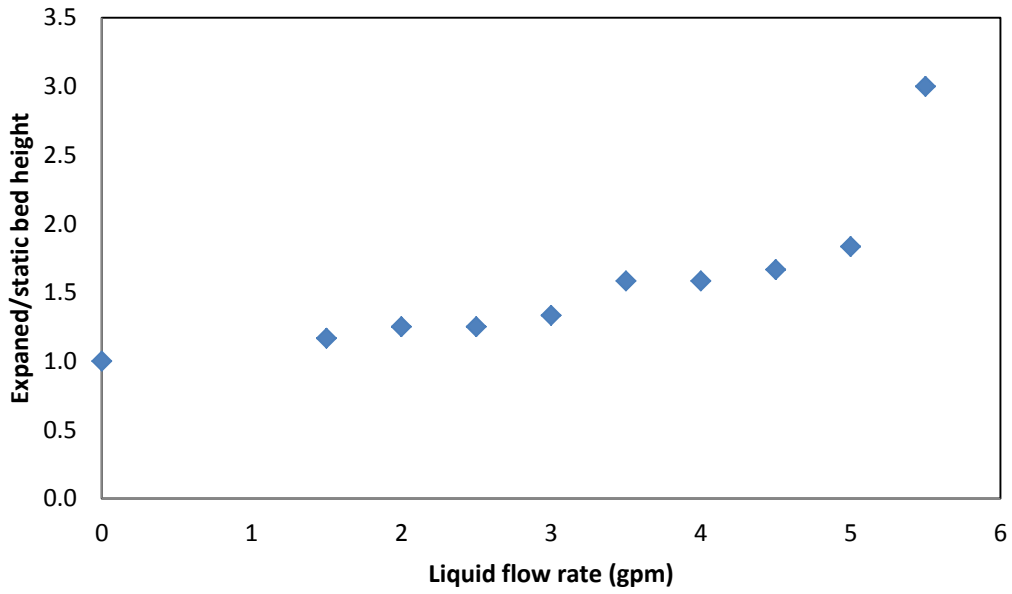

Figure 3.5 Expanded bed height at various liquid flow rates.

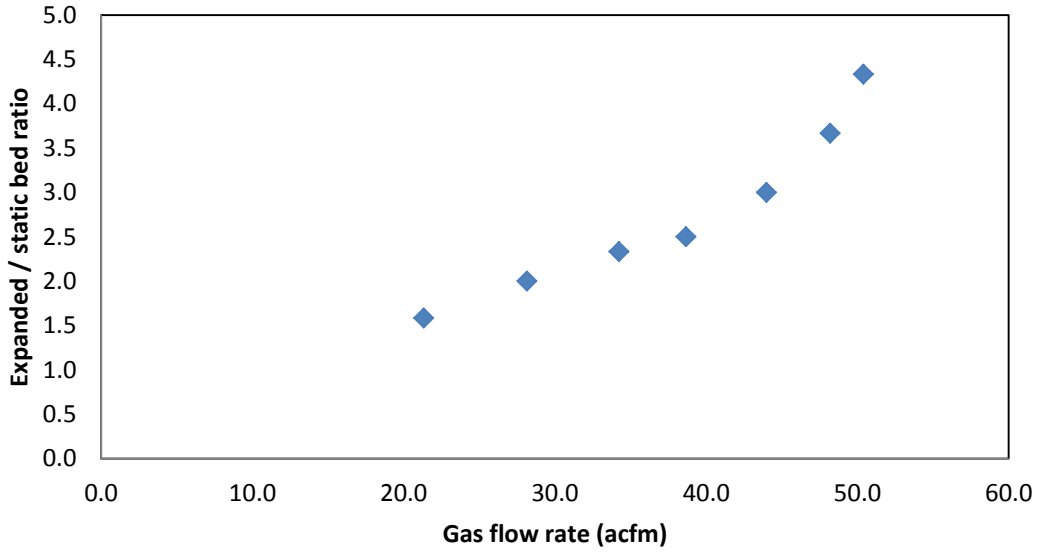

Figure 3.6 Expanded bed height at various gas flow rates.

In addition, a relationship between expanded bed height and L/G ratio was correlated. The results show that an increase in an L/G ratio results in an increase in expanded bed height, therefore improving the scrubbing performance. However, a pressure drop also increased as a result.

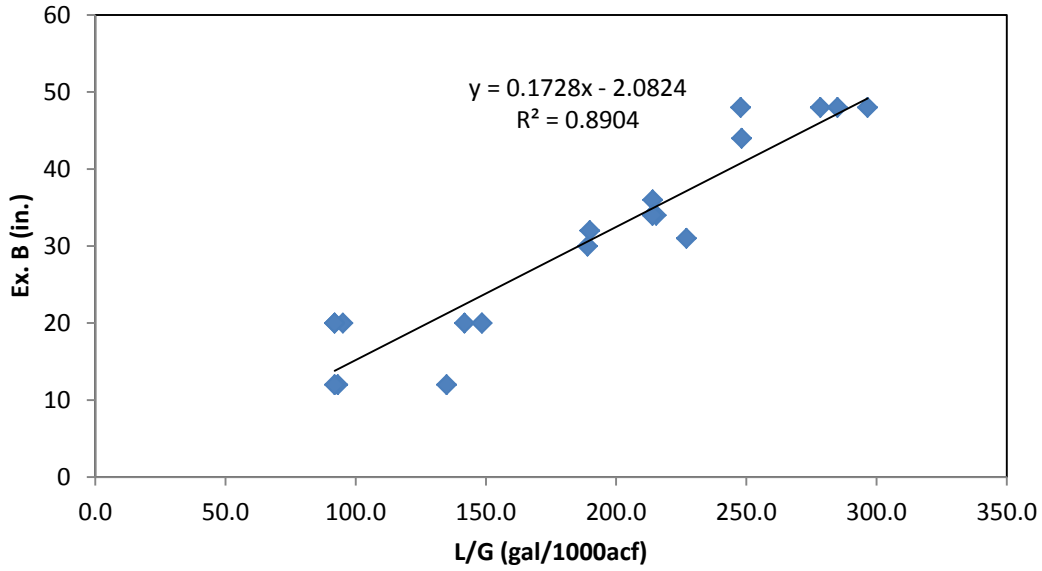

Figure 3.7 Expanded bed height at various L/G ratios.

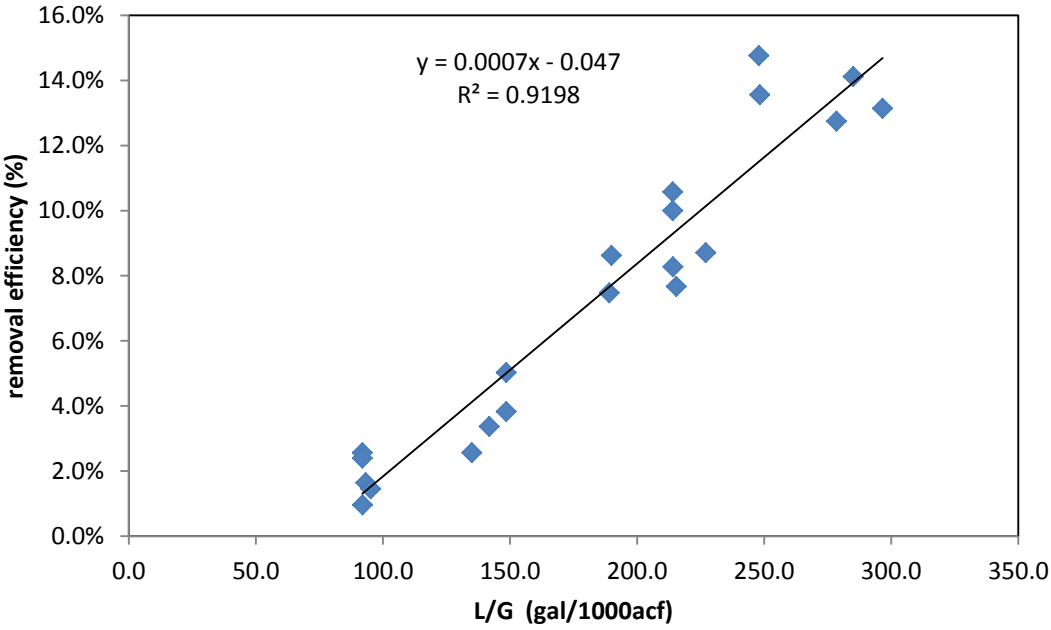

Figure 3.8 CO_2 removal efficiency at various L/G ratios using pure water.

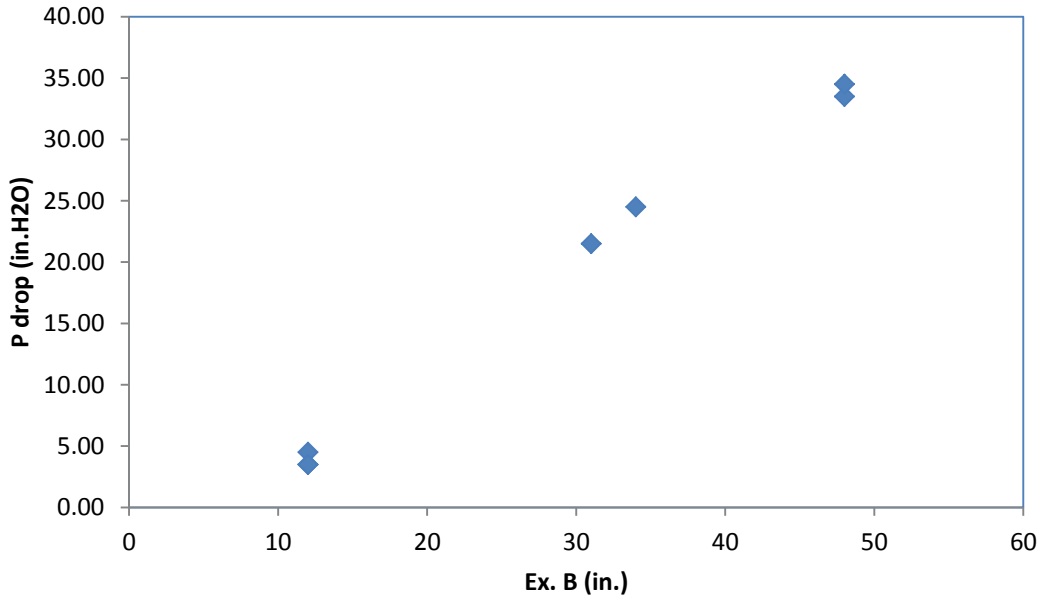

Figure 3.9 Relationship between pressure drop and expanded bed height.

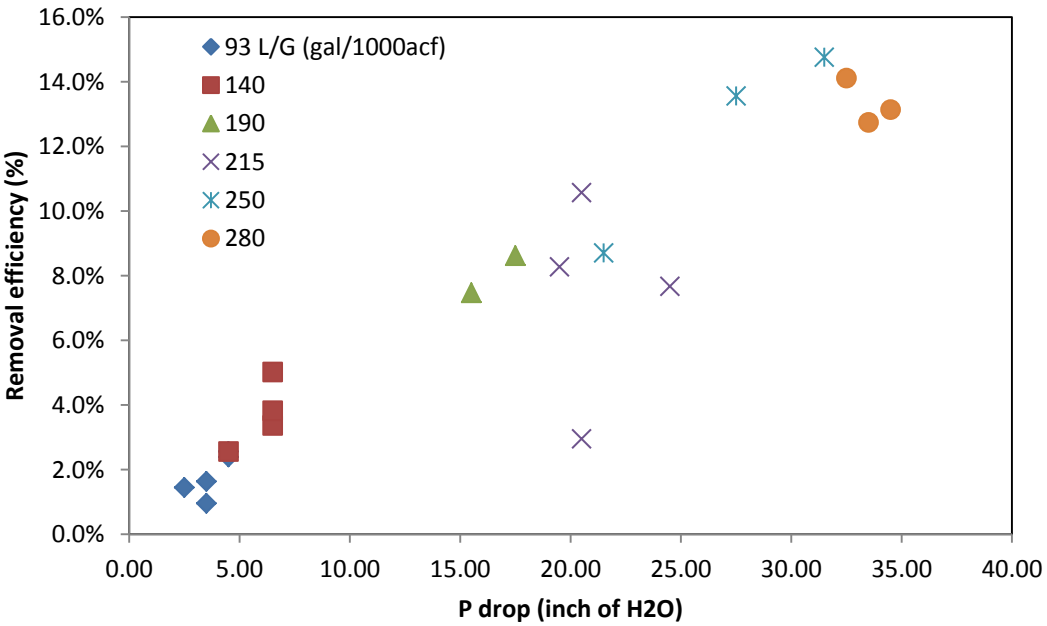

Figure 3.10 CO_2 removal efficiency and pressure drop at various L/G ratios.

Furthermore, the relationship between pressure drop and gas flow rate was investigated to give the loading and flooding points for the absorber operation. Operation near the loading point gives the highest mass-transfer performance.

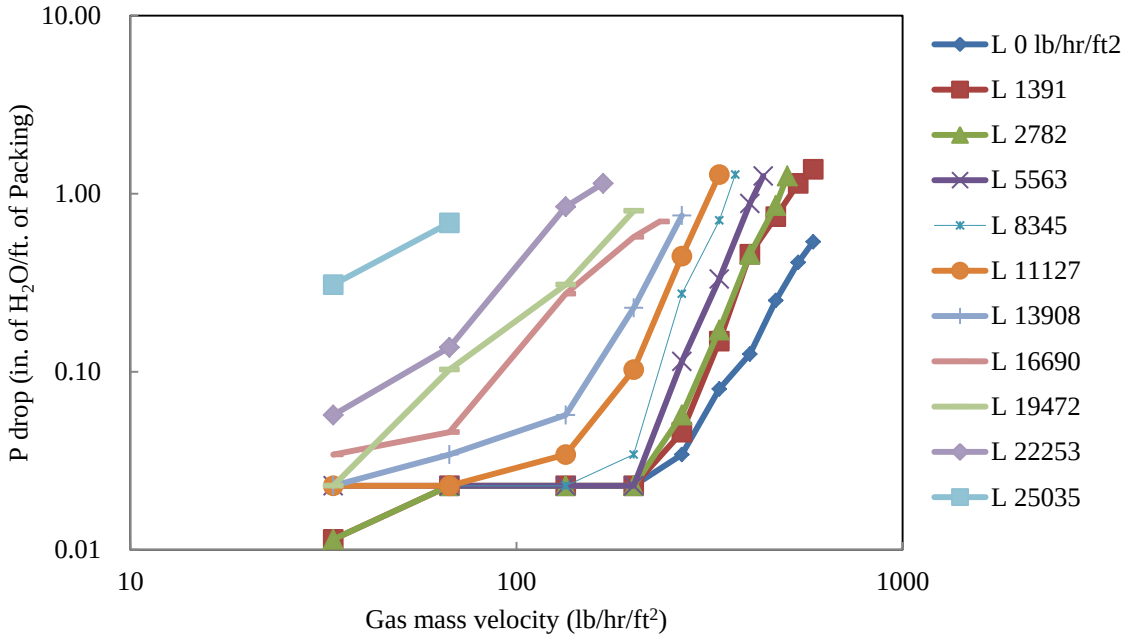

Figure 3.11 Loading and flooding points.

3.4.4 Effects of gas distribution on CO_2 gas removal

5 mm Raschig rings were used as a gas distributor at the bottom of the column. Raschig ring packings with 2, 4, 7, and 14 inch heights were tested under various L/G ratios. Our results show that various heights of gas distributors almost gave the same or similar CO_2 gas removal performances. Higher height of gas distribution increases the system pressure drop. Therefore, for TCA operation, a low height of gas distributor is recommended.

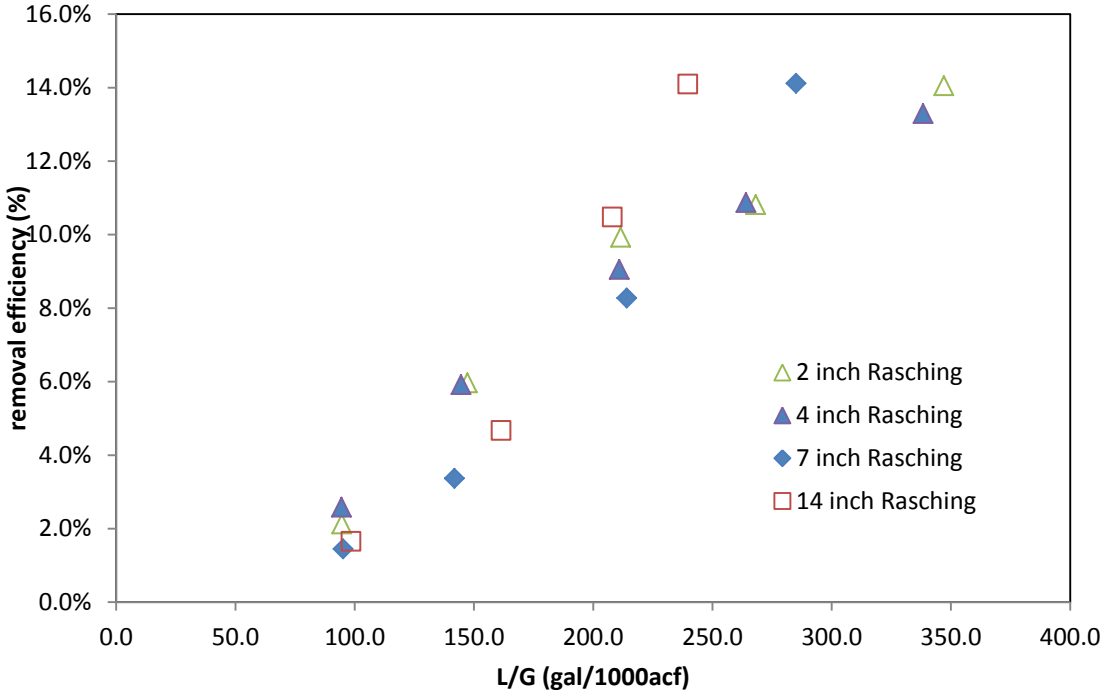

Figure 3.12 CO_2 gas removal performances with different heights of gas distributors.

3.4.5 Effects of a number of gas distributors on removal efficiency

A number of gas distributors was also studied for its effect on CO_2 gas removal. It was expected that the CO_2 removal efficiency would increase as the packing's uniformity increases. As shown in Figure 3.13, multiple gas distributors showed a slightly better CO_2 removal performance than a single distributor system.

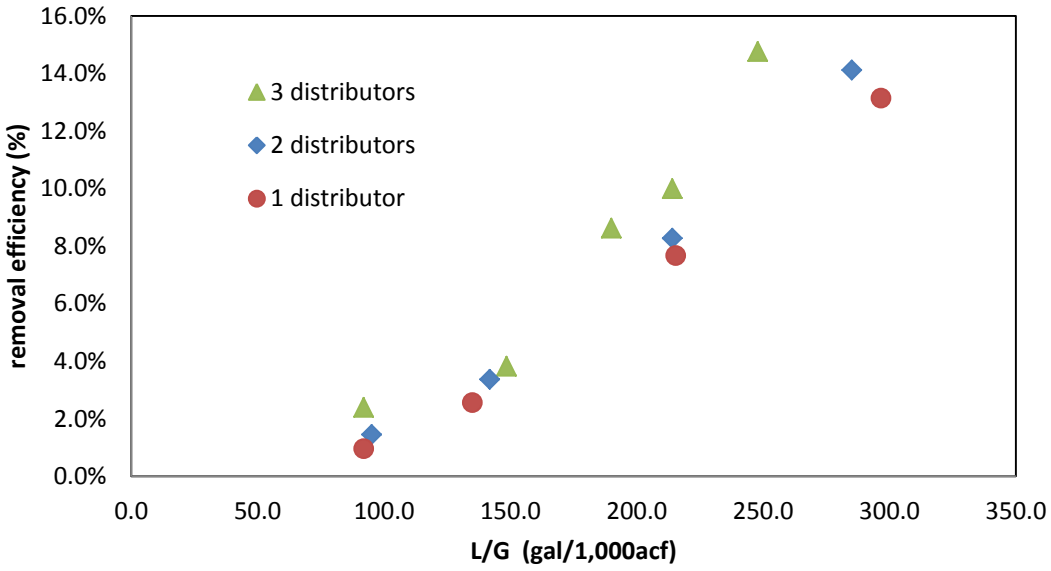

Figure 3.13 CO_2 removal performances with various gas distributors.

3.4.6 Effects of inlet CO_2 gas concentrations on CO_2 removal efficiency

Inlet CO_2 gas concentrations between 5 to 16% were tested for its removal efficiency. Theoretically, flue gas with higher CO_2 partial pressure will have higher concentration driving force for gas side mass transfer. The results showed that different inlet CO_2 concentrations in the range showed almost the same CO_2 removal performances. This indicates that overall mass transfer may mainly depend on the liquid-side mass transfer under the range.

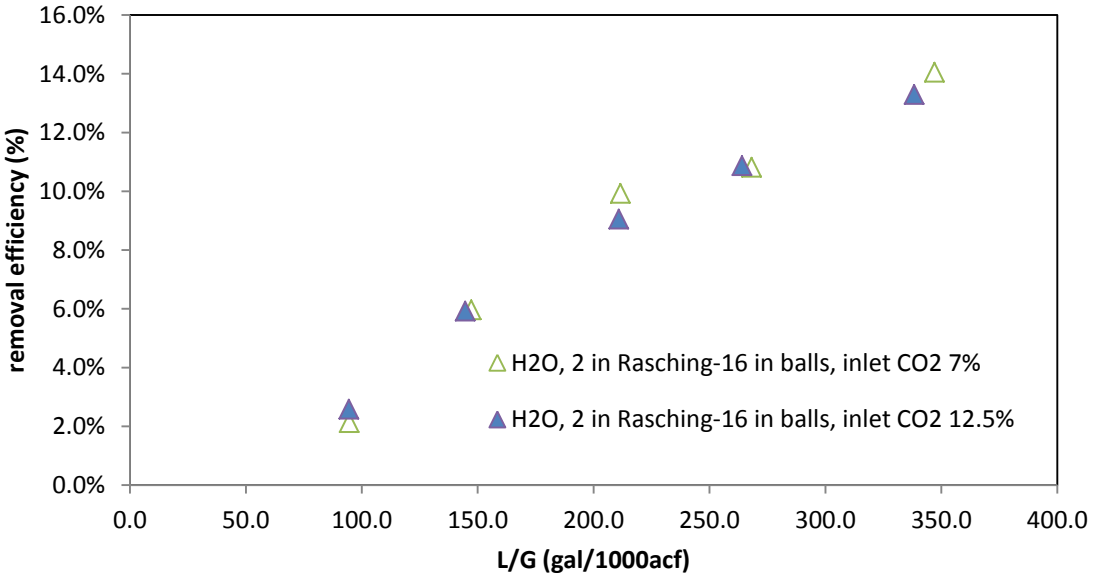

Figure 3.14 CO_2 gas removal efficiency with respect to different inlet CO_2 concentrations in terms of different L/G ratios.

3.4.7 Relationship between gas holdup and L/G ratio

Gas hold-up is a very important parameter for TCA design and operation. Typically, in most TCA operations, an increase in gas hold-up results in a decrease in system pressure drop, therefore improving the energy demand. On the other hand, an increase in an L/G ratio results in better scrubbing performance but higher pressure drop. The results show that an increase in L/G ratios decreased gas hold-up but benefited the scrubbing performance by an increase in bed height.

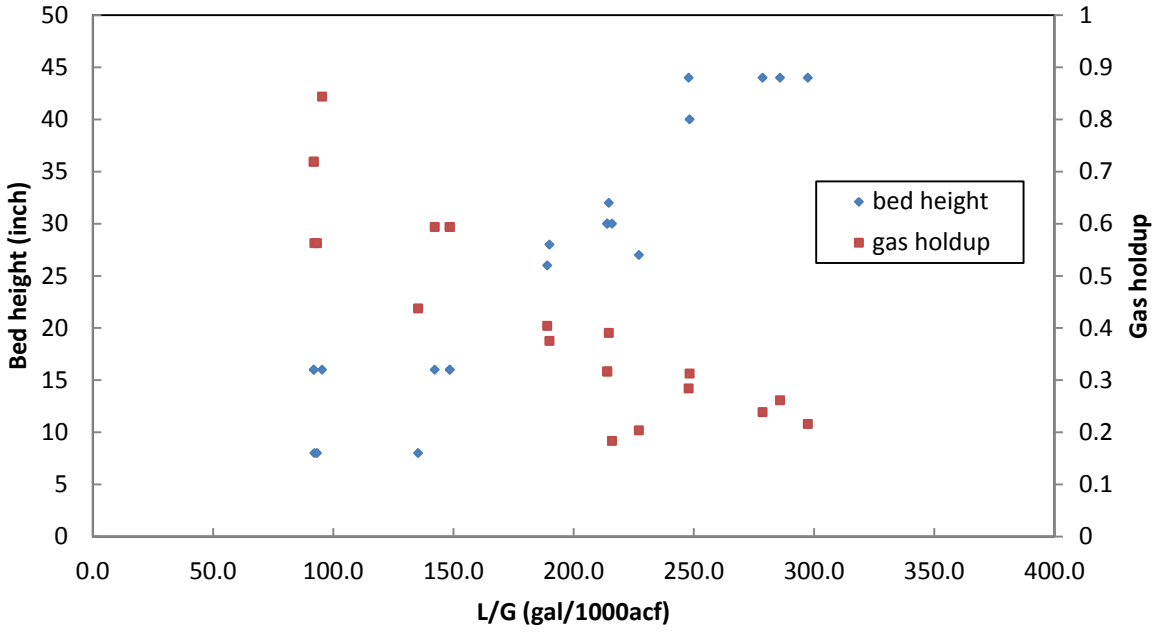

Figure 3.15 TCA bed height and gas hold-up in terms of L/G ratios.

3.4.8 Solvent tests

NaOH and $Mg(OH)_2$ solutions were tested under various L/G ratios. A 1 M NaOH solution could achieve 70% of CO_2 removal efficiency at an L/G ratio of 170 gal/1,000 acf while a 0.1 M NaOH solution could achieve 35% of CO_2 removal at the same L/G ratio. A 0.1 M $Mg(OH)_2$ solution can only reach 10% of CO_2 removal even at L/G of 350 gal/1000 acf. These performance differences are attributed to different alkalinity of cations and availability of OH^- ions in the solution, to which the dissolution rate of $Mg(OH)_2$ particles is critical. This result suggests that the liquid-side mass transfer accounts for a large proportion of the overall mass transfer of the TCA operation.

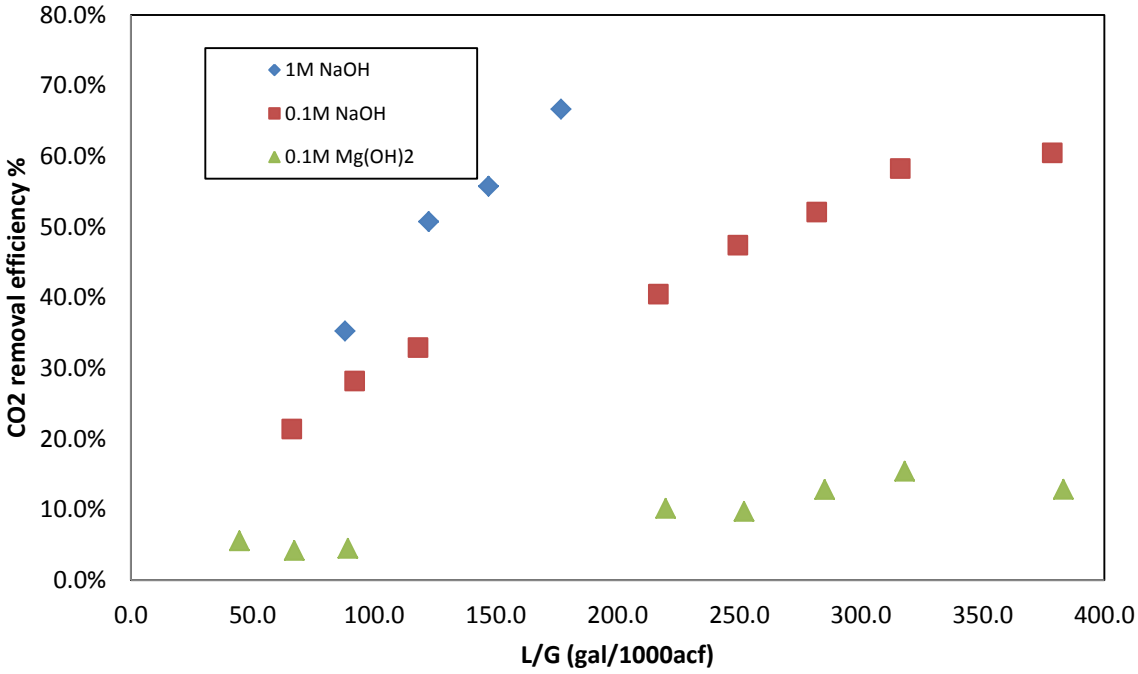

Figure 3.16 CO_2 removal efficiencies of 0.1 M $Mg(OH)_2$, 0.1 M NaOH, and 1 M NaOH solutions at various L/G ratios.

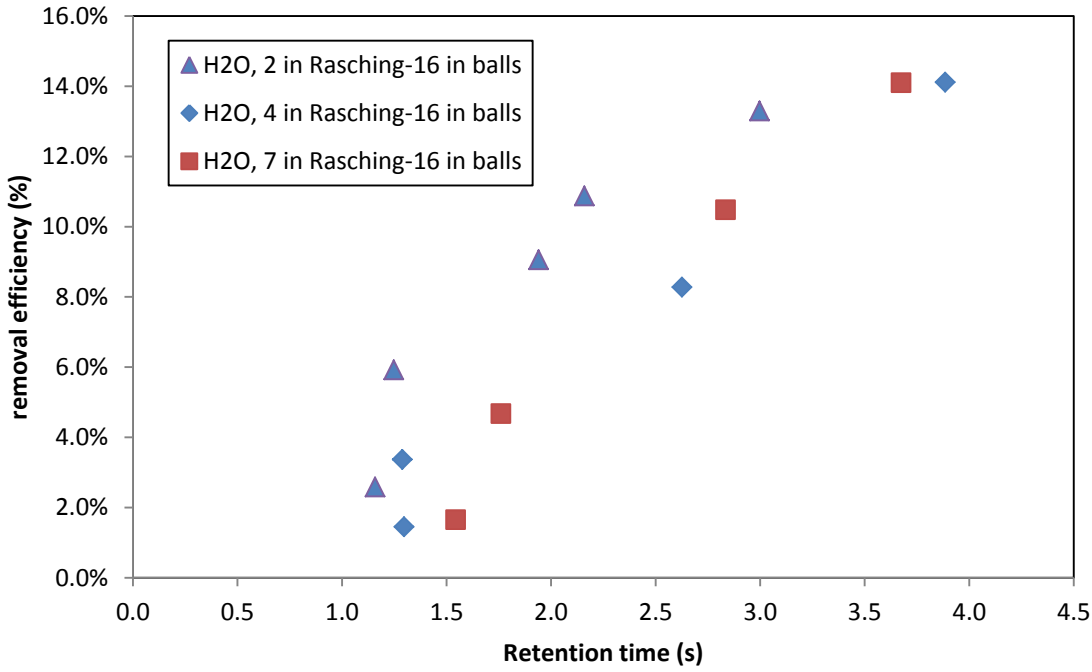

Figure 3.17 CO_2 removal efficiencies in pure water at various gas retention time.

3.4.9 Tanks-in-series model

The absorption of CO_2 gas into water involves physical absorption and chemical hydrolysis reactions. A tanks-in-series model considers a system whose behavior is between two ideal reactors of continuous stirred tank reactors (CSTR) in series and a plug flow reactor. For CO_2 gas absorption into water, the following component mass balance equation for CO_2 gas can be derived for the completely mixed gas and liquid phases:

$$Y_{in}\frac{\rho_{air}V_G}{MW_{air}} - Y_{out}\frac{\rho_{air}V_G}{MW_{air}} = \left(\frac{Y_{out}}{H}\right)\frac{\rho_{H_2O}V_L}{MW_{H_2O}} \tag{3.9}$$

where:

ρ_{air} = density of air = 0.001185 (g/cm^3) @ air temperature 25 °C, 1 atm;

ρ_{H2O} = density of water = 0.9992 (g/cm^3) @ water temperature 25 °C, 1 atm;

Y_{in} = inlet CO_2 gas molar fraction (dimensionless) = inlet CO_2 gas partial pressure (atm);

Y_{out} = outlet CO_2 gas molar fraction (dimensionless) = outlet CO_2 gas partial pressure (atm);

V_G = gas volumetric flow rate (cm^3/sec);

V_L = water volumetric flow rate (cm^3/sec);

MW = molecular weight of air and H_2O (g/mole);

H = Henry's law constant for CO_2 into water ($\frac{mole\ fraction_{air}}{mole\ fraction_{water}}$);

= 1054500 × exp(-3050.73/T) = 26.5 @ water temperature 25 °C.

The CO_2 removal efficiency at the equilibrium state, η_{EQ}, for one CSTR is:

$$\eta_{EQ} = \frac{\left(Y_{in} - Y_{out}\right)}{Y_{in}} = \frac{\rho_{H_2O}MW_{air}V_L}{H\,\rho_{air}MW_{H_2O}V_G + \rho_{H_2O}MW_{air}V_L} \tag{3.10}$$

An actual TCA system performs between an ideal CSTR and a plug flow reactor. The overall CO_2 removal efficiency can be expressed at equilibrium as a series of several CSTRs as the follows:

$$\eta_{overall} = 1-(1-\eta_{EQ})^n \tag{3.11}$$

where n = number of CSTR tanks in series (dimensionless).

From the above model, a maximum overall CO_2 removal efficiency at the equilibrium state can be predicted and compared to an experimental removal efficiency. The number of tanks, n, is between 1 and infinity, which should be determined by fitting the experimental data.

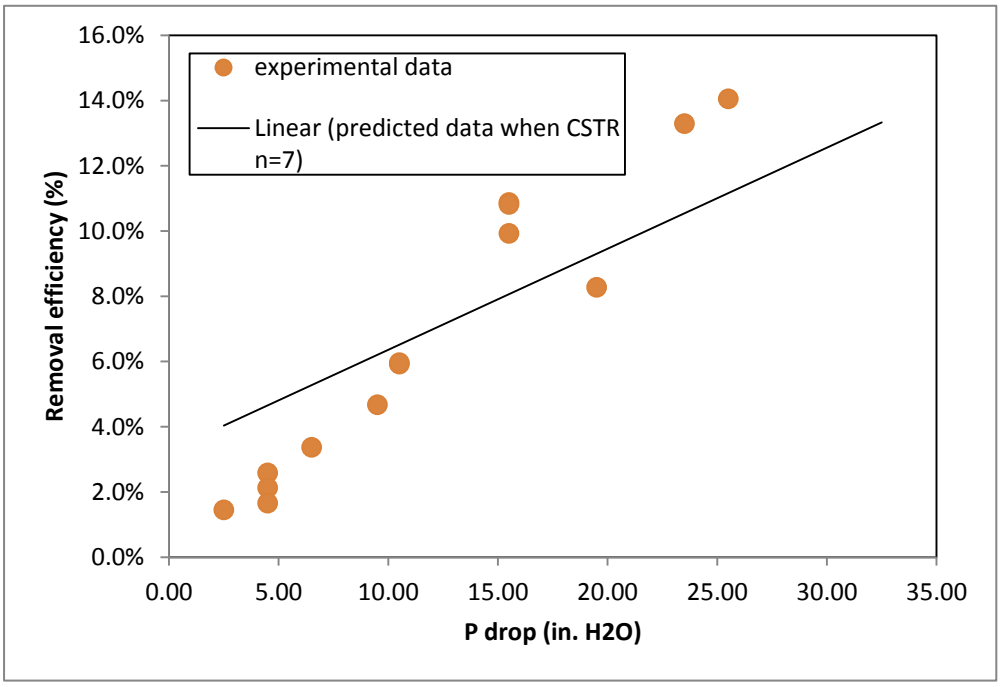

Figure 3.18 Comparison of experimental and predicted CO_2 removal efficiencies at various pressure drops.

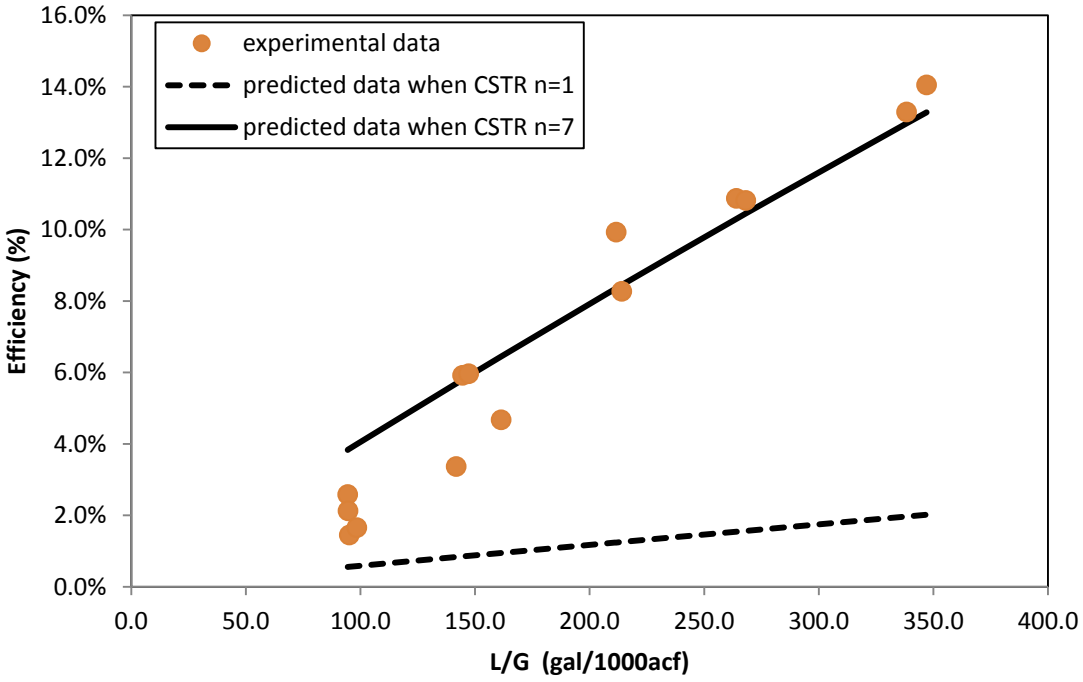

Figure 3.19 Comparison of experimental and predicted CO_2 removal efficiencies at various L/G ratios.

3.4.10 Mass-transfer resistance in NaOH-CO_2 system

0.1-4 M NaOH solutions were tested for CO_2 absorption in the TCA column in order to study the mass-transfer resistance in the NaOH-CO_2 system. The results show that the NaOH-CO_2 system may be divided into two regimes in terms of NaOH concentrations. At the concentration range of 0.1 to 1 M, it is found that the CO_2 removal efficiency significantly increased from 35 to 67% as NaOH concentration increased from 0.1 to 1 M in the TCA column. The result shows that the liquid-phase mass transfer accounts for a larger proportion of overall mass transfer than the gas-phase mass transfer. At a concentration range of 1 to 4 M, it is found that CO_2 removal efficiency only slightly increased from 65 to 70% when NaOH concentration increases from 1 to 4 M. This result suggests that the gas-phase mass transfer may be a rate-limiting step when the concentration is greater than 1 M.

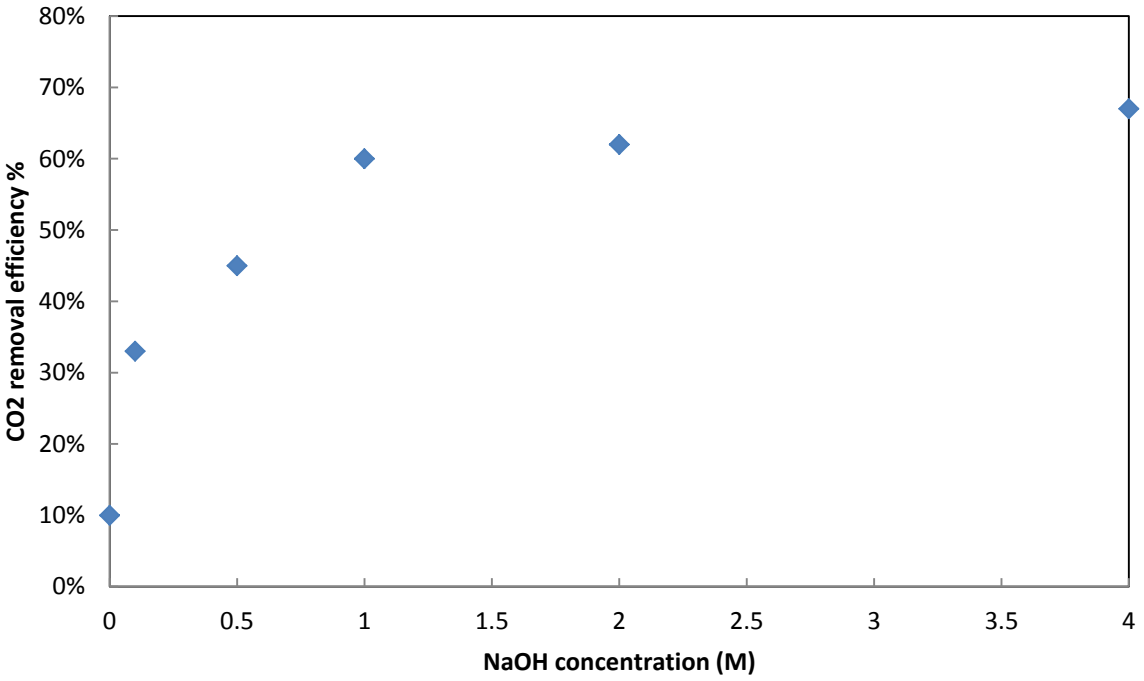

Figure 3.20 CO_2 removal efficiency at various NaOH concentrations.

Overall mass-transfer coefficient, K_ga, was calculated at various L/G ratios for 0.1 and 1 M NaOH solutions. The values were found to be 0.006-0.008 and 0.014-0.018 kmol/(m^3·sec·atm) at a range of L/G ratios of 10-30 L/m^3 for 0.1 and 1 M NaOH solutions, respectively. In addition, the specification and performance data have been compared with other widely studied systems as shown in Table 3.2. The results show that the L/G ratios used in the TCA was greater than that of packed tower and spray tower, but the TCA residence time was significantly less than those typically used for sprayer tower and packed tower.

Table 3.2 Comparison of specification and performance in varied mass transfer devices.

Solvent	Absorber	Column diameter × Height (m·m)	Packing	L/G ratio ($L \cdot m^{-3}$)	Residence time (s)	Removal efficiency (%)
1.2~2.5 M NaOH (Tontiwachwuthikul, Meisen et al. 1992)	Packed tower	0.1 × 6.55	Berl saddles, 12.7 mm	0.1~0.2	10~20	62~100
0.4~1.2 M NaOH (Herskowits, Herskowits et al. 1990)	Impinging-Jet absorber	0.06 × 0.23~0.3	None	26~105	0.4~4	N/A
2.5 M NaOH + 0.7 M $Ca(OH)_2$ (Chen, Fang et al. 2005)	Spray tower	0.1 × 0.7	None	3	30	48
1.25 M NaOH (Javed, Mahmud et al. 2010)	Spray scrubber	0.1 × 1.25	None	8	15	~40
1 M NaOH	TCA	0.13 × 1.5	Hollow ball, 10 mm	24	3.3	~60

4. CO_2 Absorption and Desorption in Bubble Column

Our previous CO_2 gas absorption results in a turbulent contact absorber (TCA) were not good because the gas residence time in the absorber was not long enough to obtain a high CO_2 removal efficiency. Therefore, a bubble column approach was introduced to obtain a CO_2 gas removal efficiency greater than 90%.

4.1 Experimental design of bubble column (batch and continuous operation)

A bubble absorption column experimental set-up consists of seven major sections: (1) simulated flue gas generation; (2) flow control; (3) bubble column absorber; (4) stripper (desorber); (5) gas sampling and analysis; (6) pH, temperature measurement; (7) data acquisition. A schematic of the experimental set-up is shown in Figure 4.1.

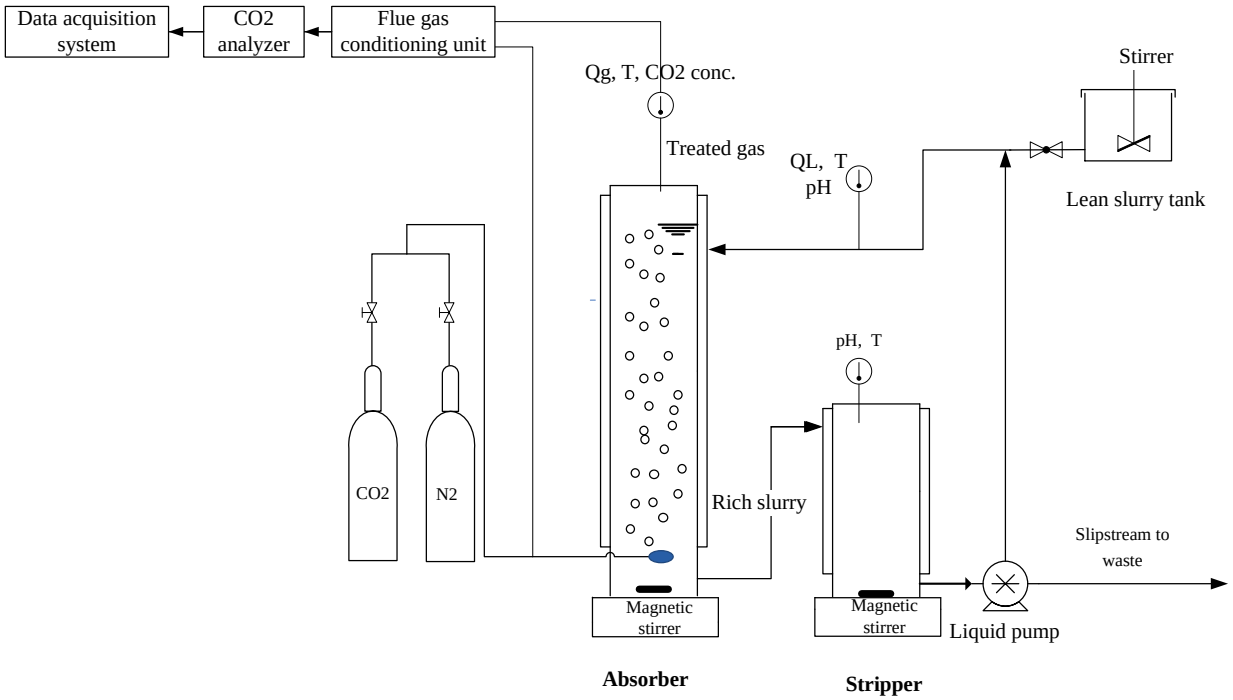

Figure 4.1. Experimental set-up of bubble column test.

A column with a 130-cm height and a 10-cm diameter made of Plexiglas with a heating jacket and thermal insulation was used as a main body of the bubble column reactor. Three sampling ports are located near the top, middle and bottom of the reactor to obtain temperature and pH data from the reactor. Fritted glass size C (porosity 25-50 micron, ACE glass Inc.) was installed at the bottom of the reactor as the gas bubbler. A 5-L glass column with a heating

jacket and thermal insulation was used as a stripper. Both absorber and stripper were sat on the magnetic stirrer plate allowing for mixing during absorption and desorption.

A simulated flue gas was produced by mixing pure CO_2 gas with pure N_2 gas (high purity >99%, Wright Brothers Inc.). Both gas streams were controlled by mass flow controllers (Thermal gas mass flow controller, Cole Parmer Inc.) in order to have desirable CO_2 concentrations. The mixed gas stream was heated and maintained at 52 °C, which was close to a typical temperature of a wet FGD outlet.

The gas sampling system consists of an in-line flue gas conditioning unit (IMR 400 flue-gas conditioning system, Environmental Equipment Inc.) where the particles in the sample were removed by the filter, and water vapor was removed by passing through the Nafion dryer. The pretreated gas sample was then analyzed for CO_2 gas concentration by an infrared CO_2 gas analyzer (Model ZRH infrared analyzer, California Analytical Instruments Inc.). The CO_2 gas analyzer was periodically calibrated by using pure N_2 (high purity >99%, Wright Brothers Inc), 5% CO_2 and 16% CO_2 (certified grade, CO_2 in N_2, Purity Plus Gas Inc) standard gases.

The pH of the fluid was measured by a pH meter (Model 25, Fisher Scientific Inc.). Temperatures were measured at the gas inlet stream and three locations along the bubble column for monitoring and maintaining the test conditions. A computer with data acquisition system (Model USB-1208FS, NI Instruments Inc.) was used to record the CO_2 gas concentrations, temperatures, and pH values throughout the experiments. Magnesium hydroxide solutions were prepared by dissolving a magnesium hydroxide powder (industry grade, 81% purity, Garrison Minerals LLC.) in deionized water. The experimental conditions used are summarized in Table 4.1.

Table 4.1. Experimental conditions used for bubble column tests.

Parameter	Value
Inlet gas temperature	~52 °C
Absorber temperature	~52 °C
Stripper temperature	60-85 °C
Gas flow rate	0.5 L/min
Inlet CO_2 concentration	5-16 % vol.
$Mg(OH)_2$ concentration	0.01-0.1 M
Mixing rate	1,200 RPM
Porosity of gas bubbler	25-50 micron

4.2 Experimental design for desorption

An absorption-desorption cyclic test was used to determine the CO_2 removal and separation capacity of magnesium slurry solutions. In the absorption and desorption process, 16%(v) CO_2 and pure N_2 were introduced to the bottom of the bubble column for absorption and desorption. The concentration of CO_2 gas was monitored at the outlet with an NDIR CO_2 analyzer. The absorption was considered to be complete when a CO_2 gas reading from the analyzer was equal to the inlet CO_2 concentration, while the desorption was considered to be complete when the CO_2 gas concentration measured in the desorber was equal or close to zero. Liquid and solid samples were taken at the end of each process. The carbon content in the liquid was quantified by a wet chemistry method (Snoeyink and Jenkins 1980), and the carbon in the solid was quantified by an elemental analyzer (Elementar, Vario Macro Cube).

4.3 Results and discussion

4.3.1 Bubble column absorption results

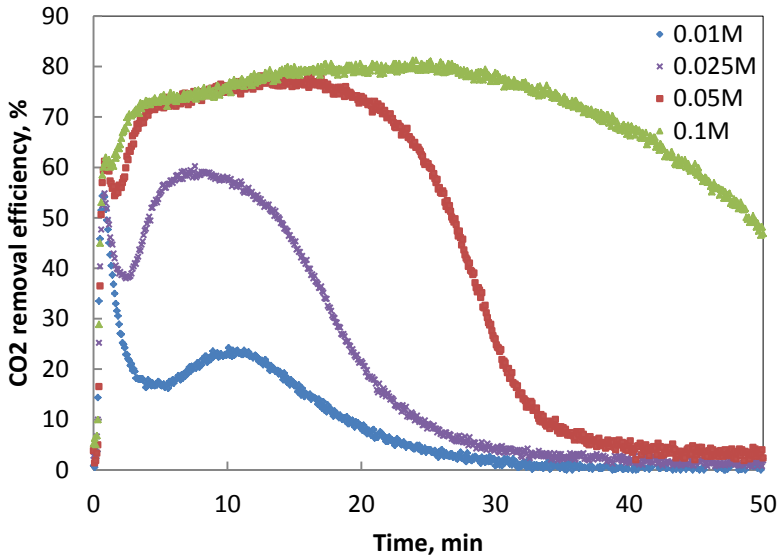

Figure 4.2. CO_2 removal efficiencies under semi-batch runs in a bubble column. Operating conditions: temperature = 52 °C; distributor filter C (ACE glass, 25~50 μm); gas flow rate = 1.8 acfm; gas residence time = 9 s, L/G ratio = 110 gal/1,000 acf; inlet CO_2 gas concentration = 8.6%(v).

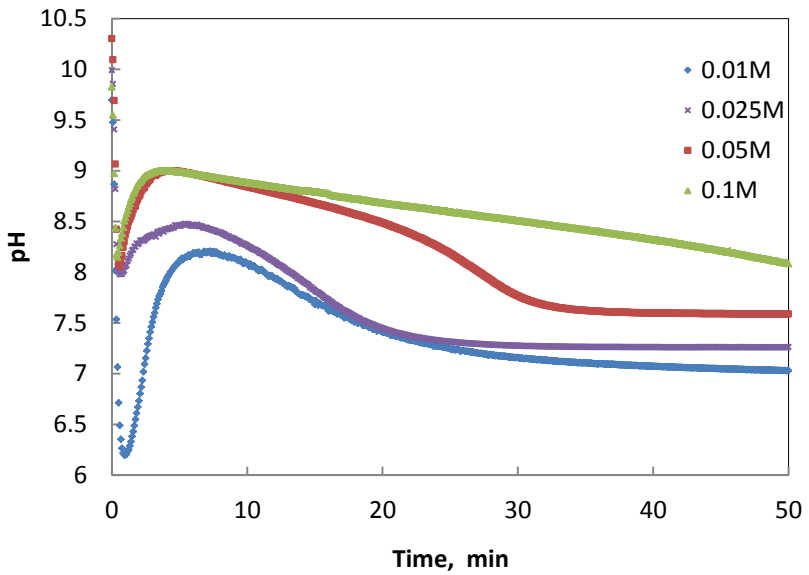

Figure 4.3. pH profiles during CO_2 removal under semi-batch runs in a bubble column. Operating conditions: distributor filter C (ACE glass, 25~50 μm); gas flow rate = 1.8 acfm; gas residence time = 9 s, L/G ratio = 110 gal/1,000acf; inlet CO_2 gas concentration = 8.6%(v).

Figure 4.2 and 4.3 demonstrate the CO_2 removal and pH profiles during batch absorption tests. In the beginning of the absorption process, a fast decrease in the pH value and high CO_2 removal were observed, which was independent of $Mg(OH)_2$ concentrations. This is due to the fast consumption of the readily available dissolved alkalinity. A rate of pH decrease depends on the dissolution rate of $Mg(OH)_2$ particles. After $Mg(OH)_2$ particles start to dissolve, the CO_2 removal efficiency reaches relatively a constant rate period where the absorption of CO_2 gas is balanced with the dissolution of $Mg(OH)_2$ particles into the liquid. Then the pH starts to gradually decrease. The dissolution rate during this period seems to be dependent on available surface areas, the pH of the solution, and thus the concentration of $Mg(OH)_2$ solutions. The result clearly shows that 0.1 and 0.05 M solutions have much faster dissolution rates than 0.025 and 0.01 M solutions. However, a 0.1 M solution showed slightly higher CO_2 removal efficiencies than a 0.05 M solution when $Mg(OH)_2$ particles seem to become available. In the meantime, the pH values continued to decrease as a result of a decrease in available $Mg(OH)_2$ particles, and eventually reached equilibrium pH values. The equilibrium pH values were 7.2, 7.4, 7.7, and 8.0 for 0.01, 0.025, 0.05 and 0.1 M solutions, respectively.

4.3.2 Effects of L/G ratios on CO_2 removal

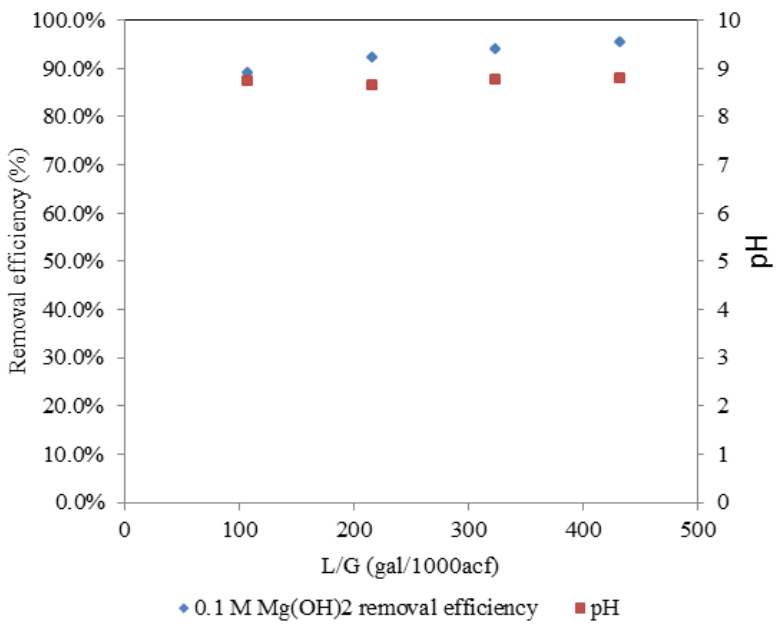

Figure 4.4. Effects of L/G ratios on CO_2 removal. Operating conditions: distributor filter C (ACE glass, 25~50 μm); gas flow rate = 1.9 acfm; residence time = 9 s; inlet CO_2 concentration = 7.9%(v).

Figure 4.4 shows the CO_2 removal performance at different L/G ratios. It shows that 110 gal/1,000 acf L/G warrants >90% CO_2 removal. The CO_2 removal efficiency increased from 90 to 98% when the L/G ratio increased from 100 to 450 gal/1,000 acf. In comparison, a wet FGD scrubber typically uses 60 to 180 gal/1,000acf for >90% SO_2 removal (Smith, Swenson et al. 1983).

4.3.3 Effects of inlet CO_2 gas concentrations on CO_2 removal

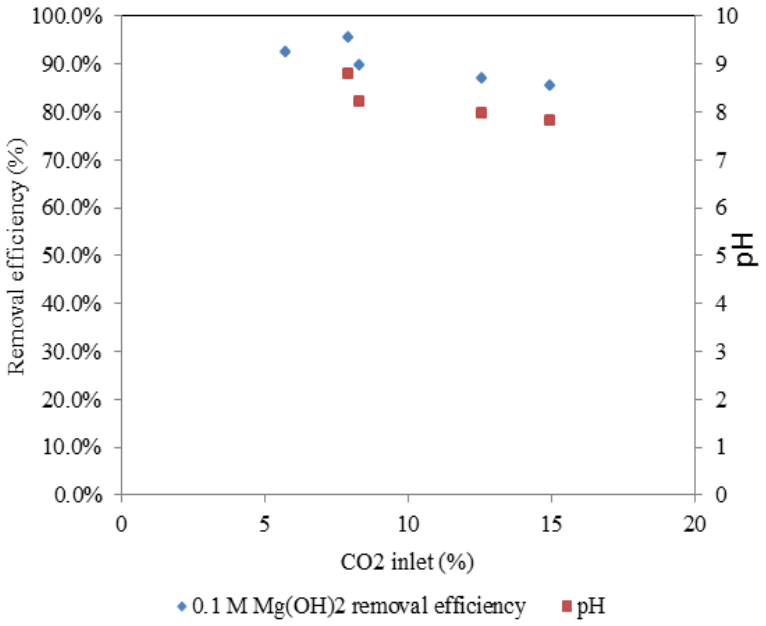

Figure 4.5. Effects of inlet CO_2 gas concentrations on CO_2 removal. Operating conditions: distributor filter C; gas flow rate = 1.9 acfm; gas residence time = 8.5 s; L/G ratio = 110 gal/1,000acf.

Figure 4.5 shows the effects of inlet CO_2 gas concentrations on the CO_2 removal performance. It shows that a 0.1 M $Mg(OH)_2$ solution has almost the same CO_2 removal performance when an inlet CO_2 gas concentration was less than 20%.

4.3.4 Effects of gas residence time on CO_2 removal

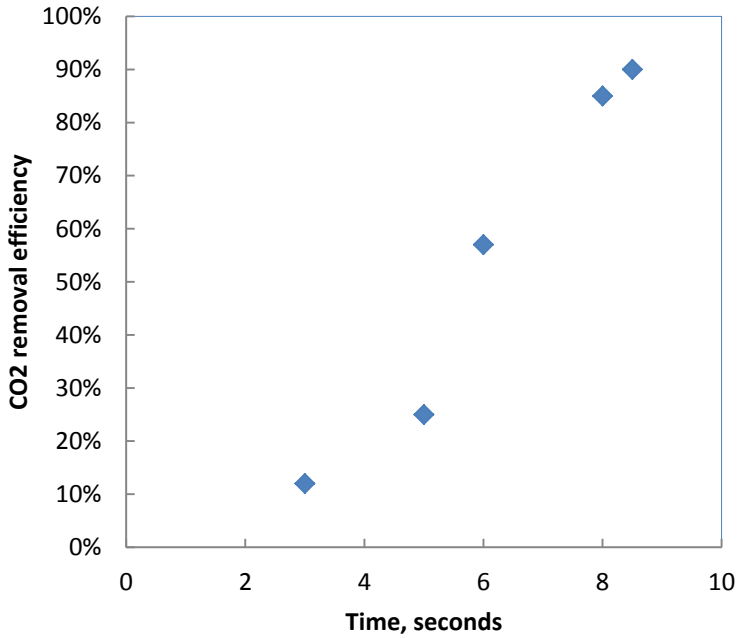

Figure 4.6. Effects of gas residence time on CO_2 removal. Operating conditions: 0.1 M $Mg(OH)_2$; distributor filter C; gas flow rate = 1.9 acfm; L/G ratio = 106 gal/1,000acf; inlet CO_2 concentration = 7.9%(v).

The removal efficiency heavily depends on the gas residence time, and >8.5-sec residence time warrants >90% CO_2 removal.

4.3.5 Cyclic test results

One cyclic test consists of an absorption run followed by a desorption run. Table 4.2 shows the effects of desorption temperatures on carbon recovery of CO_2 rich solution. It clearly shows that CO_2 recovery increases with an increase in a desorption temperature.

Table 4.2. Results of cyclic test under different desorption temperatures.

Desorption temperature, ℃	Rich solution, mol CO_2 /mol Mg	Regenerated solution, mol CO_2 /mol Mg	% of recovery (Recovery/removal)
60	0.456	0.199	56%
65	0.481	0.196	59%
75	0.509	0.189	63%
85	0.610	0.189	70%

Table 4.3 shows a carbon mass balance obtained from the cyclic test. For each absorption process, the carbon removed from the gas phase should theoretically go into the liquid or solid phase. For each desorption cycle, the amount of carbon originally in a rich solution should be theoretically equal to the sum of the carbon recovered and the carbon still remaining in the liquid and solid phases.

Table 4.3 Carbon mass balance of absorption-desorption cyclic tests.

	C removed/recovered , mole	C in the system, mole	C in liquid, mole	C in solids, mole	Unaccounted, mole	Unaccounted, %
1st absorption	0.0288	0.0288	0.0260	0.0000	0.0028	9.7
1st desorption	0.0122	0.0260	0.0070	0.0081	-0.0013	5.0
2nd absorption	0.0124	0.0275	0.0200	0.0045	0.0030	10.9
2nd desorption	0.0110	0.0245	0.0045	0.0097	-0.0006	2.4
3rd absorption	0.0100	0.0241	0.0170	0.0055	0.0016	6.7
3rd desorption	0.0101	0.0225	0.0035	0.0097	-0.0007	3.2
4th absorption	0.0098	0.0230	0.0150	0.0058	0.0022	9.4
4th desorption	0.0089	0.0208	0.0035	0.0098	-0.0014	6.8
						Avg=6.8

Figure 4.7 shows the effect of absorption-desorption cycles on CO_2 gas removal. The result shows that the CO_2 capture capacity decreased ~30-40% of the original fresh capacity after first desorption, but afterwards, the capacity approached ~50%. Figure 4.8 shows the accumulated carbon captured per initial magnesium at different desorption temperatures. It shows that the carbon/magnesium molar ratio can increase from ~9 to ~10 when a desorption temperature increased from 75 to 85 °C. High temperature helps remove more carbon.

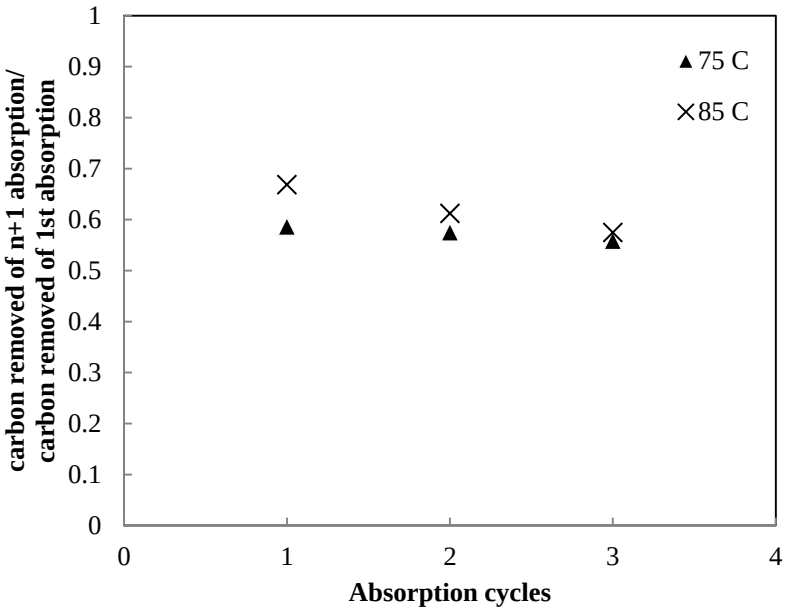

Figure 4.7. Absorption capacity with respect to absorption cycles under different temperatures.

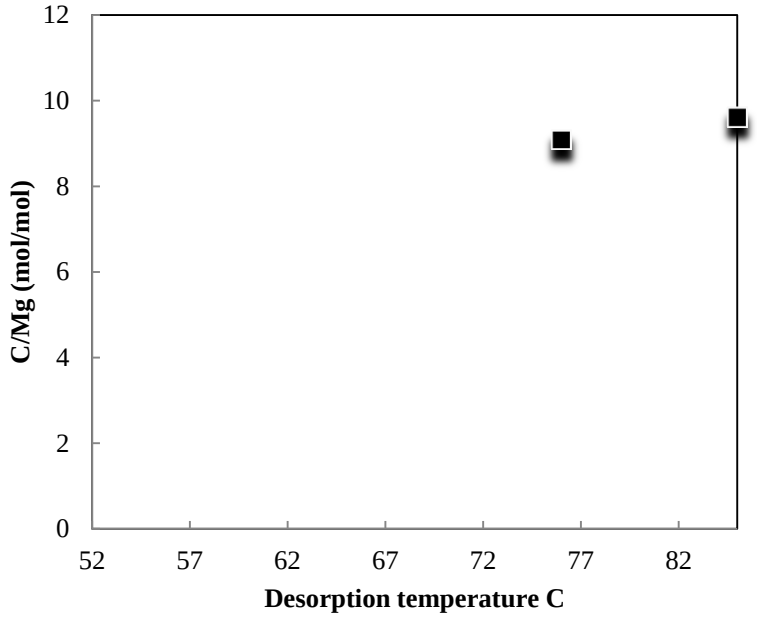

Figure 4.8. Accumulated carbon removed per initial magnesium content during a cyclic test.

4.3.6 Continuous test results

Figure 4.9 shows the CO_2 removal performance and pH values under a steady-state condition. It shows that >90% CO_2 removal could be achieved by adding a small make-up flow of fresh

$Mg(OH)_2$ slurry. The pH in the absorber could be kept at ~8.6 where regenerable bicarbonate ions are dominated. A fresh make-up $Mg(OH)_2$ slurry flow rate has been determined to be 8 mL/second to make the system keep >90% CO_2 removal at 52 °C in the absorber and 75 °C in the desorber.

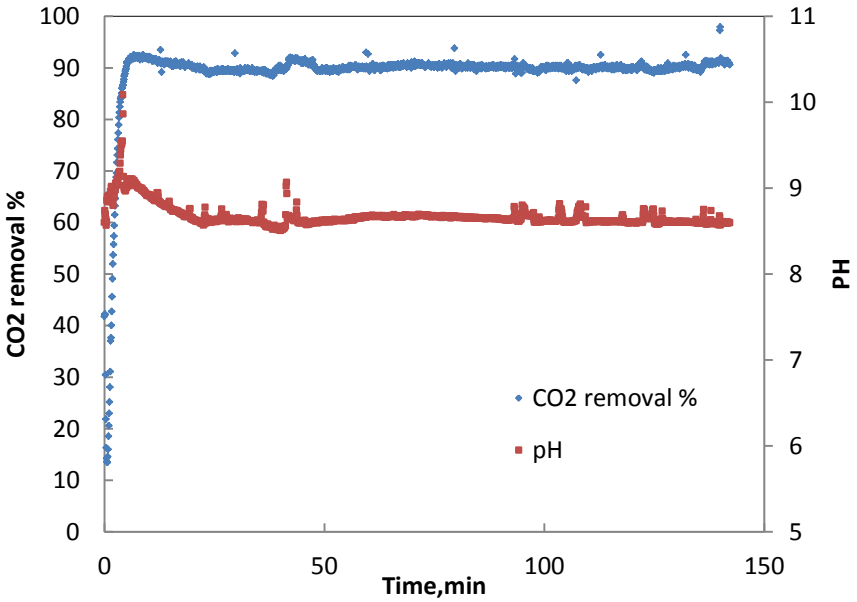

Figure 4.9. CO_2 removal and pH under continuous operation mode. (0.1 M $Mg(OH)_2$; distributor filter C (ACE glass, 25~50 μm); gas flow rate = 1.9 acfm; gas residence time = 9 s; inlet CO_2 gas concentration = 7.9%(v), temperature = 52 °C; L/G ratio = 106 gal/1,000acf)

5. CO_2 Absorption Model in Bubble Column Absorber

This chapter addresses the development of a mathematical model for CO_2 absorption in a bubble column absorber. A primary objective of this work was to investigate the chemical reaction mechanisms and the mass-transfer phenomena in the absorption process using a model for a better understanding of CO_2 gas removal in a gas-liquid-solid system (Cheng, Li et al. 2013). In addition, the overall mass-transfer coefficient K_G, a key design parameter for absorption process, has been calculated and compared with the coefficient values for other widely studied CO_2 scrubbing systems. Table 5.1 summaries the literature findings for mass-transfer studies in bubble columns.

Table 5.1 Summary of mass-transfer studies for bubble columns reported in the literature.

Solution	Significant findings	Operation conditions	Experiment setup
Li-CO_3-K_2CO_3(Kanai, Fukunaga et al.)	k_La decreased with increasing temperature, k_La increased linearly with increased gas velocity	673K-1173K, 1 atm pressure, slurry concentration 38-62 % wt.	Bubble column, 0.4 m in height, 0.031 m in inner diameter
Diethanolamine DEA(Maceiras, Nóvoa et al. 2007)	Correlate the local mass transfer coefficient with Re, Sh, Sc numbers	DEA concentration 0.05-1 mole/L, gas flow rate 10-25 L/h	Bubble column 0.06 m x0.06 m rectangular section and 1.03 m in height
DEA, MDEA(Maceiras, Alves et al. 2008)	Develop the stagnant cap model, mass transfer coefficient decreases as bubbles rise along the column	Solvent concentration 0.05-1 mol/L, temperature 293-303 K	Bubble column 0.06 m x0.06 m rectangular section and 1 m in height
Triethanolamine TEA(Rubia, García-Abuín et al. 2010)	Interfacial area and mass transfer coefficient were calculated by using a photographic method based on the bubble size determination	Solvent concentration 0-1 mol/L, room temperature, batch mode, gas flow rate 15-30 L/h	Bubble column 0.06 m x0.06 m rectangular section and 1 m in height
NaOH(Fleischer, Becker et al. 1996)	Developed a one-dimensional non-isothermal two-phase reactor model. It consists of	Gas flow rate 0-20 L/min	Volume is 11.5 L, and 1.78 m in height

	mass, momentum, energy, and bubble population balance equations.		
$NaHCO_3$ and $NaCO_3$(Wylock, Larcy et al. 2010)	2D axisymmetrical model for a spherical bubble rising in a liquid. Chemical reactions are coupled with mass transport. Correlate the mass transfer coefficient with Re, Sh for clean and fully contaminated interface	273-300 K, spherical bubble	COMSOL multiphysics software
MEA(Chen, Shi et al. 2008; Chen 2012)	Film theory. Overall mass transfer coefficient 6.6E-7 to 9.1E-6 mol/cm^3-atm-second	P_{CO2}=0.1-0.3 atm; C_{MEA}= 4 M	Bubble column

A $Mg(OH)_2$-CO_2 system is a gas-liquid-solid reaction system. The CO_2 gas in the gas phase needs to be dissolved in the water in order to react with magnesium ions which are dissolved from magnesium hydroxide particles. The entire scrubbing process may be characterized as physical absorption of CO_2 in water coupled with ionic reactions between dissolved CO_2 species and magnesium ions along with the dissolution of the magnesium particles. Therefore, this chapter will first present the physical absorption of CO_2 gas in H_2O and subsequent chemical reactions.

5.1 Physical absorption of CO_2-H_2O

Bubble column is preferred to operate under homogeneous conditions where a flow condition falls into the laminar flow regime (Treybal 1967; Shah, Kelkar et al. 1982). This bubbly flow may give more uniform and smaller bubbles for large surface areas and long retention times. The system can be easily described by the two film theory. The model developed here is based on uniform mixing in the liquid phase and plug flow in the gas phase. Absorption rate, r_A, can be expressed in terms of gas- or liquid-side mass transfer coefficients based on the film theory:

$$r_A = k_G a(P_A - P_{Ai}) \quad (5.1)$$
$$r_A = k_L a(C_{Ai} - C_{AT}) \quad (5.2)$$

P_{Ai} and C_{Ai} are CO_2 concentrations at the gas-liquid interface following the Henry's Law.

$$H_{CO2} = \frac{P_{Ai}}{C_{Ai}} \quad (5.3)$$

The interfacial compositions cannot be determined. Instead, the bulk driving force which may be characterized as overall mass transfer coefficient can be applied. Therefore, the absorption rate can be written as:

$$r_A = \frac{dC_{AT}}{dt} = K_G a(P_A - H_{CO2} C_{AT}) \quad (5.4)$$

The CO_2 partial pressure in the bubble will change with the position in the column. Here, it is assumed that a pseudo-steady state condition exists between the CO_2 partial pressure of the bubble and the CO_2 concentration in the liquid. Therefore, the Equation (5.4) can be rewritten as:

$$\frac{dC_{AT}}{dt} = K_G a(P_{avg} - H_{CO2} C_{AT}) \quad (5.5)$$

Perform a mass balance on CO_2 in the bubble as it rises up in the column in the x direction assuming a pseudo-steady state condition.

$$\frac{dP_A}{dx} = -\frac{RT}{u} K_G a(P_A - H_{CO2} C_{AT}) \quad (5.6)$$

Letting $z = \frac{x}{L}, V_L = SL, \ Q_g = uS$, then:

$$\frac{dP_A}{dz} = -\frac{RTV_L}{Q_g} K_G a(P_A - H_{CO2} C_{AT}) \quad (5.7)$$

This is the governing equation for bubble column absorption. It expresses a change of CO_2 concentrations in the liquid in terms of the bubble CO_2 partial pressure, which is changing with respect to the position in the liquid column, z. Therefore, the average CO_2 concentration in the bubble can be found by integrating Equation (5.7) between the limits of z=0, $p_A=p_0$ and z=1:

$$P_{avg} = \frac{Q_g P_0 - \mathrm{H_{CO2}} C_{AT} Q_g + e^{\frac{-RTV_L \mathrm{K_G a}}{Q_g}} (\mathrm{H_{CO2}} C_{AT} Q_g - Q_g P_0 + e^{\frac{RTV_L \mathrm{K_G a}}{Q_g}}) \mathrm{H_{CO2}} C_{AT} RT \mathrm{K_G a}}{RTV_L \mathrm{K_G a}} \quad (5.8)$$

Substitute the average bubble CO_2 concentration into the Equation (5.5), integrate with respect to the time:

$$C_{AT} = \frac{P_0}{H_{CO2}} e^{-m}(e^m - 1) \quad (5.9)$$

Where $m = \frac{Q_g \mathrm{H_{CO2}} \mathrm{t}}{RTV_L} e^{\frac{-RTV_L \mathrm{K_G a}}{Q_g}} (e^{\frac{RTV_L \mathrm{K_G a}}{Q_g}} - 1)$

Then, solve for $\mathrm{K_G a}$ overall mass transfer coefficient as:

$$\mathrm{K_G a} = -\frac{Q_g \ln \frac{Q_g \mathrm{H_{CO2}} \mathrm{t} + RTV_L \ln \frac{P_0 - \mathrm{H_{CO2}} C_{AT}}{P_0}}{Q_g \mathrm{H_{CO2}} \mathrm{t}}}{RTV_L} \quad (5.10)$$

This equation shows that the overall mass-transfer rate is dependent on the hydrodynamic parameters, equilibrium constant, CO_2 gas partial pressure in the gas phase and the temperature. In addition, it is necessary to calculate the total dissolved carbon and pH when system reaches the equilibrium. These numbers provide the quality assurance when we perform the experiment data analysis.

Equilibrium concentration calculation of total dissolved carbon C_{eq}

The chemistry of CO_2 gas dissolved in the water is well known and can be expressed as following:

$$H_2O + CO_{2\,gas} \overset{\mathrm{H_{CO2}}}{\longleftrightarrow} H_2CO_3^* \quad (5.11)$$

$$H_2CO_3^* \overset{K_1}{\leftrightarrow} H^+ + HCO_3^- \quad (5.12)$$

$$HCO_3^- \overset{K_2}{\leftrightarrow} H^+ + CO_3^{2-} \quad (5.13)$$

In addition, these carbonate species concentrations can be written as:

$$[H_2CO_3^*] = \mathrm{H_{CO2}} P_{eq} \quad (5.14)$$

$$[HCO_3^-] = \frac{K_1}{[H^+]} \mathrm{H_{CO2}} P_{eq} \quad (5.15)$$

$$[CO_3^{2-}] = \frac{K_1 K_2}{[H^+]^2} \mathrm{H_{CO2}} P_{eq} \quad (5.16)$$

Therefore, C_{eq} can be written as the sum of these species:

$$C_{eq} = (1 + \frac{K_1}{[H^+]} + \frac{K_1 K_2}{[H^+]^2})\mathrm{H_{CO2}} P_{eq} \quad (5.17)$$

Equilibrium pH calculation

For CO_2-water system, the electro neutrality equation can be written as:

$$[H^+] = [OH^-] + [HCO_3^-] + 2[CO_3^{2-}] \quad (5.18)$$

This electro-neutrality equation is only valid for pure CO_2-water system. If any other ions presented in the solution, then these ions need to be considered. Substitute the equilibrium equations and this becomes:

$$[H^+] = \frac{K_w}{[H^+]} + \frac{K_1}{[H^+]}\mathrm{H_{CO2}} P_{eq} + 2\frac{K_1 K_2}{[H^+]^2}\mathrm{H_{CO2}} P_{eq} \quad (5.19)$$

Rearrange as:

$$[H^+]^3 - \left(K_w + \mathrm{H_{CO2}} P_{eq} K_1\right)[H^+] - 2\mathrm{H_{CO2}} P_{eq} K_1 K_2 = 0 \quad (5.20)$$

K_1, K_2, K_w, and H_{CO2} are temperature dependent equilibrium constants. Therefore, the equilibrium pH can be determined once these constants are given. Figure 5.1 shows the relationship between equilibrium constants and temperatures.

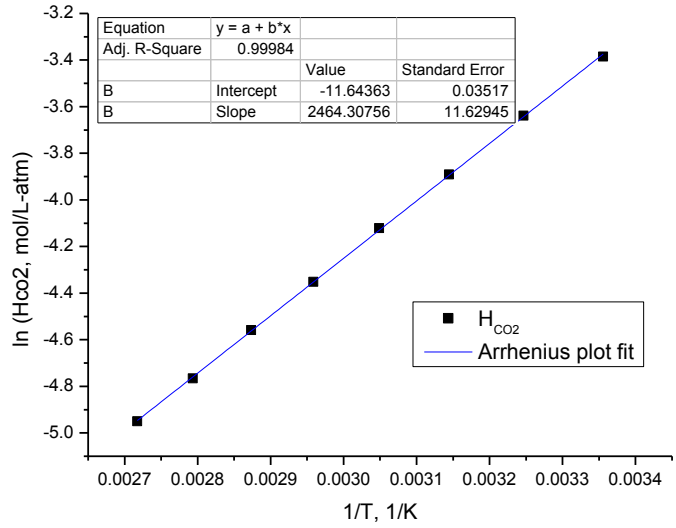
Equation | y = a + b*x
Adj. R-Square | 0.99984
Value | Standard Error
B | Intercept | -11.64363 | 0.03517
B | Slope | 2464.30756 | 11.62945
ln (Hco2, mol/L-atm)
1/T, 1/K
H_CO2
Arrhenius plot fit

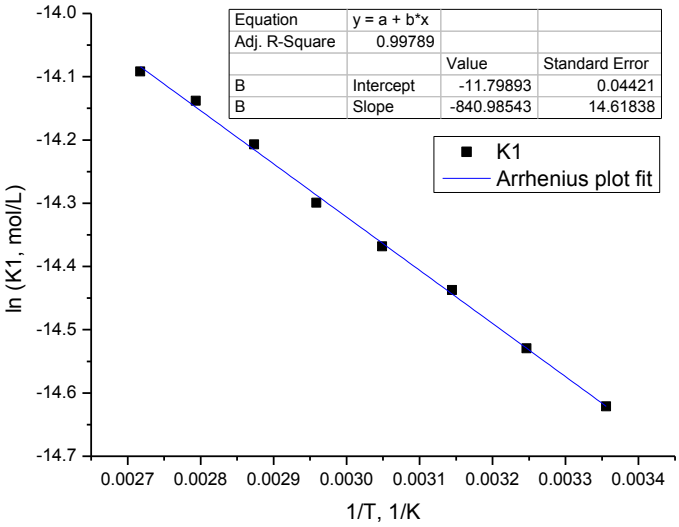
Equation | y = a + b*x
Adj. R-Square | 0.99789
Value | Standard Error
B | Intercept | -11.79893 | 0.04421
B | Slope | -840.98543 | 14.61838
ln (K1, mol/L)
1/T, 1/K
K1
Arrhenius plot fit

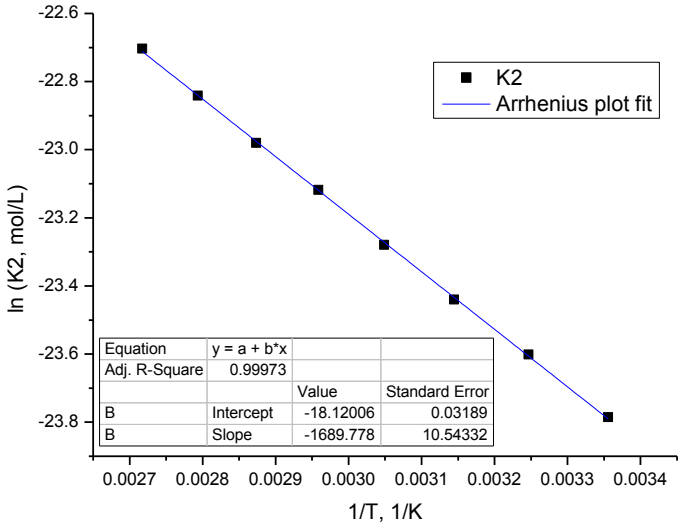

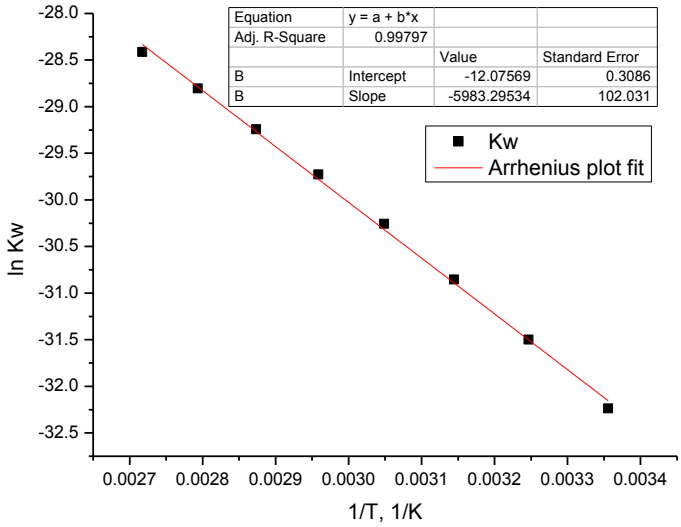

Figure 5.1. Plots of K_1, K_2, K_w, and H_{CO2} at different temperatures.

5.2 Absorption with reaction of CO_2-$Mg(OH)_2$ system

The major absorption steps involved in the system are: gas absorption and diffusion, ionic reactions at the liquid phase, solid dissolution and diffusion. It was assumed that the reaction between dissolved CO_2(aq) and the magnesium ions is instantaneous with respect to the mass transfer. Therefore, the chemical reaction is viewed as an enhancement factor for the process; while the gas-side mass transfer and the dissolution of solid magnesium hydroxide particles are

viewed as rate-limiting steps. Figure 5.2 demonstrates the reactions schematic of the system. According to the film theory, in order to make CO_2 gas react with the magnesium hydroxide slurry, CO_2 gas needs to be dissolved and disassociated to form carbonate ions and transferred into the liquid phase. On the other hand, the magnesium hydroxide solid particles need to be dissolved and disassociated as magnesium and hydroxyl ions and transferred into the liquid phase. The reaction will occur at a plane in the liquid at a position close to the gas/liquid interface as these ions reach the reaction zone. The rate will be determined by the diffusion of CO_2(aq) and magnesium ions. In addition to the reactions between CO_2 and water, the following reactions will take place throughout the process:

$$Mg(OH)_2 \leftrightarrow Mg^{2+} + 2OH^- \quad (5.21)$$

$$2HCO_3^- + Mg^{2+} \leftrightarrow Mg(HCO_3)_2 \quad (5.22)$$

$$CO_3^{2-} + Mg^{2+} \leftrightarrow MgCO_3 \quad (5.23)$$

As Figure 5.2 shows, x is the position of the reaction plane, and it moves as the partial pressure of CO_2 changes or as magnesium ions concentration changes. The rate of CO_2 absorption in the liquid may be expressed as:

$$-r = k_{Ag}A_b(P_A - P_{Ai}) \quad CO_2\ in\ the\ gas\ film \quad (5.24)$$

$$-r = k_{Al}A_b(C_{Ai} - 0)\frac{x_0}{x} \quad CO_2\ in\ the\ liquid\ film \quad (5.25)$$

$$-r = k_{Bl}A_b(C_B - 0)\frac{x_0}{x_0 - x} \quad Mg^{2+}\ ion\ in\ the\ liquid\ film \quad (5.26)$$

$$-r = k_sA'(C_s - C_B)n_p \quad Mg\ solid\ to\ liquid \quad (5.27)$$

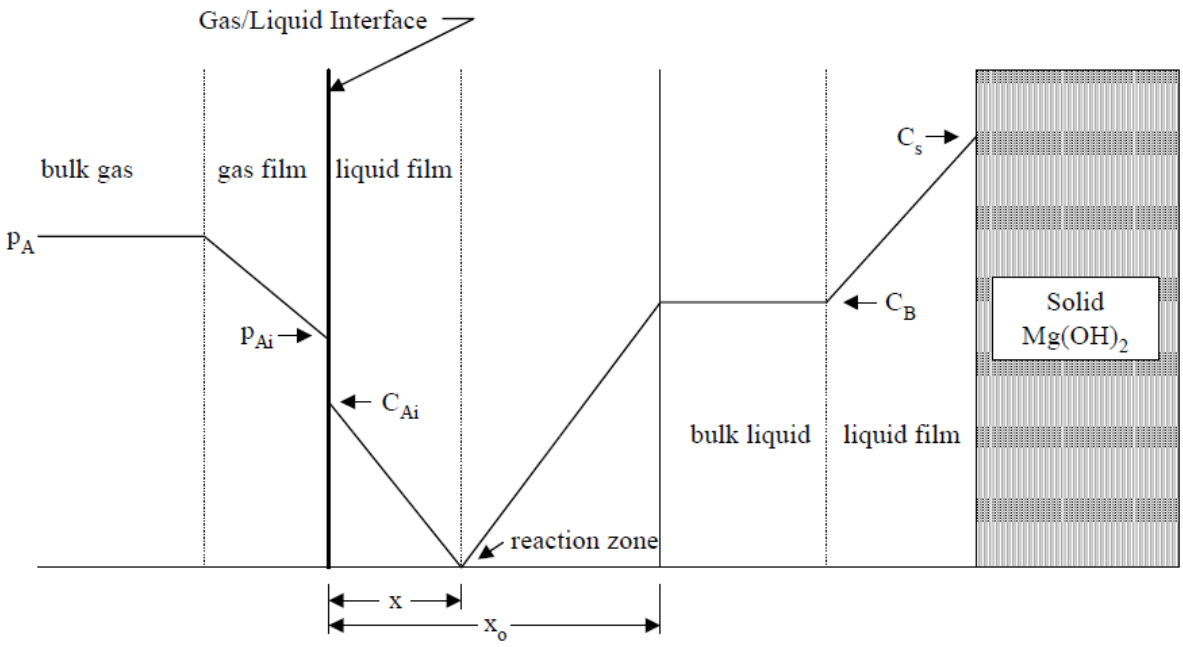

Figure 5.2. Reactions schematic of CO_2-$Mg(OH)_2$ slurry system.

The interfacial concentrations are assumed to be at equilibrium and may be related through Henry's Law:

$$P_{Ai} = \mathrm{H_{CO2}} C_{Ai} \tag{5.28}$$

The mass transfer of CO_2 and magnesium ions within the film may be explained by the diffusion, therefore, the transfer coefficient for CO_2 (A) and magnesium ions (B) in the liquid are related by:

$$\frac{k_{Al}}{k_{Bl}} = \frac{D_{Al}/x_0}{D_{Bl}/x_0} = \frac{D_{Al}}{D_{Bl}} \tag{5.29}$$

where D_{Al} and D_{Bl} are the liquid diffusivities of dissolved CO_2 and magnesium ions, respectively.

Also, the dissolution rate k_s may be explained by the diffusivity of magnesium ions in the solution and the film thickness around the solid particle:

$$k_s = \frac{D_{Bl}}{\delta} \tag{5.30}$$

Equations listed above can be solved to obtain a rate expression for $Mg(OH)_2$ slurry scrubbing CO_2:

$$-r = \frac{P_A A_b + \frac{D_{Al}}{D_{Bl}} A_b \mathrm{H_{CO2}} C_s}{\frac{1}{k_{Ag}} + \frac{\mathrm{H_{CO2}}}{k_{Al}} + \frac{\mathrm{H_{CO2}} \delta A_b}{n_p A' D_{Al}}} \tag{5.31}$$

Or, it can be rearranged as:

$$-r = \frac{P_A A_b + \frac{D_{Al}}{D_{Bl}} A_b \mathrm{H_{CO2}} C_s}{\frac{1}{k_{Ag}} + \frac{\mathrm{H_{CO2}}}{k_{Al}\left(\frac{n_p A' D_{Al}}{n_p A' D_{Al} + k_{Al} \delta A_b}\right)}} \tag{5.32}$$

Letting $\varphi = \frac{n_p A' D_{Al}}{n_p A' D_{Al} + k_{Al} \delta A_b}$, the equation becomes:

$$-r = \frac{P_A A_b + \frac{D_{Al}}{D_{Bl}} A_b \mathrm{H_{CO2}} C_s}{\frac{1}{k_{Ag}} + \frac{\mathrm{H_{CO2}}}{\varphi k_{Al}}} = \mathrm{K_G} A_b \left(P_A + \mathrm{H_{CO2}} C_s \frac{D_{Bl}}{D_{Al}}\right) \tag{5.33}$$

Where φ is the chemical enhancement factor; and $\mathrm{K_G}$ is the overall mass-transfer coefficient, and the unit is mol/cm^2-atm-sec:

$$\mathrm{K_G} = \frac{1}{\frac{1}{k_{Ag}} + \frac{\mathrm{H_{CO2}}}{\varphi k_{Al}}} \tag{5.34}$$

This is the definition term of the overall mass transfer coefficient. It clearly revealed that physical absorption and diffusion are rate limiting steps; but chemical reactions serve as rate enhancement factor. In order to quantify this coefficient, the rate expression may need to be rewritten as:

$$\frac{dC_{AT}}{dt} = \frac{-r}{V_L} = \frac{\mathrm{K_G} A_b \left(P_A + \mathrm{H_{CO2}} C_s \frac{D_{Bl}}{D_{Al}}\right)}{V_L} \tag{5.35}$$

Again, letting $z = \frac{x}{L}, V_L = SL, Q_g = u_g S,$ then:

$$\frac{dP_A}{dz} = -\frac{RT}{Q_g} \mathrm{K_G} A_b \left(\mathrm{P_A} + \mathrm{H_{CO2}} C_s \frac{D_{Bl}}{D_{Al}}\right) \tag{5.36}$$

It may be integrated between the limits of z=0 (where $P_A=P_0$) and z=1, to give an expression relating the CO_2 concentration in the bubble with respect to dimensionless position z. The average CO_2 concentration in the bubble can be found as:

$$P_{avg} = \frac{Q_g P_0 + Q_g H_{CO2} C_s \frac{D_{Bl}}{D_{Al}} - H_{CO2} C_s RT K_G A_b V_L \frac{D_{Bl}}{D_{Al}} - Q_g (P_0 + H_{CO2} C_s \frac{D_{Bl}}{D_{Al}}) e^{\frac{-RTV_L K_G A_b}{Q_g}}}{RTV_L K_G A_b} \quad (5.37)$$

The average bubble CO_2 concentration, P_{avg}, may be substituted into Equation (5.35), and integrated with respect to time and solved for the overall mass transfer coefficient, K_G, to give:

$$K_G = \frac{Q_g}{A_b RT} \ln\left[\frac{\left(P_0 + H_{CO2} C_s \frac{D_{Bl}}{D_{Al}}\right) Q_g t}{Q_g P_0 t + H_{CO2} C_s Q_g t \frac{D_{Bl}}{D_{Al}} - C_{AT} RTV_L}\right] \quad (5.38)$$

This equation allows us to calculate the overall mass-transfer coefficient once the amount of carbon removal with respect to time is known. The schematic of the model computation is presented as Figure 5.3.

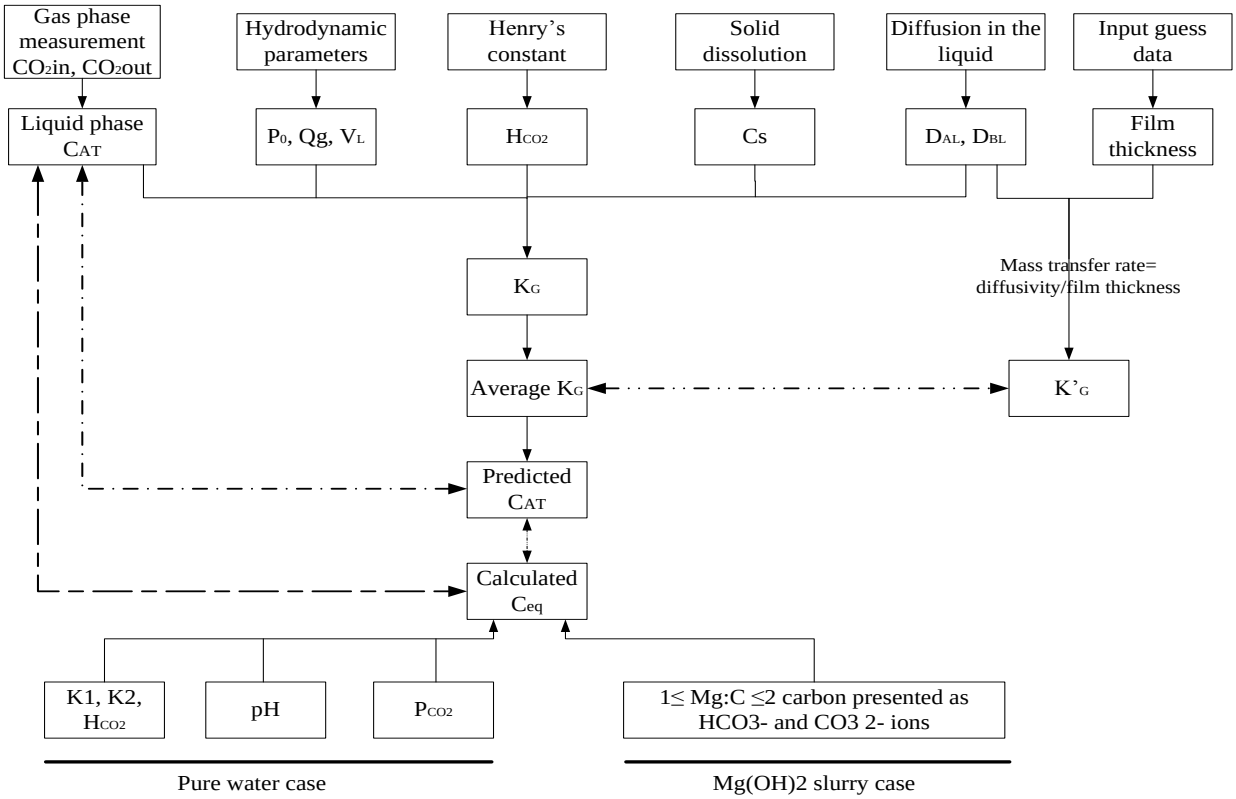

Figure 5.3. A schematic for the model computations.

5.3 Results and discussion

5.3.1 CO_2-H_2O system

CO_2 gas absorption into pure water was tested at several temperatures of 25, 39, 47 and 54 °C. The average overall mass-transfer coefficient was found from 2.75×10^{-7} to 4.1×10^{-7} mol/(cm^3·atm·sec). As shown in Figure 5.4, it was found that the overall mass-transfer coefficient decreases as temperature increases. This is because that as temperature increases, both the diffusivities of CO_2 in air and water increase, leading to an increase in the individual mass-transfer coefficients on gas (k_g) and liquid (k_L) sides. However, the physical absorption governing factor-Henry's constant decreases as temperature increases. The dependence of Henry's constant on temperature is greater than those of individual mass-transfer coefficients.

$$K_G = \frac{1}{\frac{1}{k_g}+\frac{H_{CO2}}{k_L}} \quad (5.39)$$

Where $k_g = D_{CO2\ in\ air}/\delta_{gas\ film}$; $k_L = D_{CO2\ in\ water}/\delta_{liquid\ film}$

By assuming that the gas and liquid film thicknesses are equal, the film thickness was estimated to be 0.024 cm, giving the closest overall mass-transfer rates calculated by Equation (5.38) to the measured ones. The increase of temperature also affects the water absorption capacity on CO_2. It was found that the dissolved carbon concentration at equilibrium decreased from 0.004 to 0.002 mol/L when temperature increased from 25 to 54 °C. Figure 5.5 shows that our model can adequately predict the total inorganic carbon concentration in the liquid for CO_2-water absorption process in the bubble column.

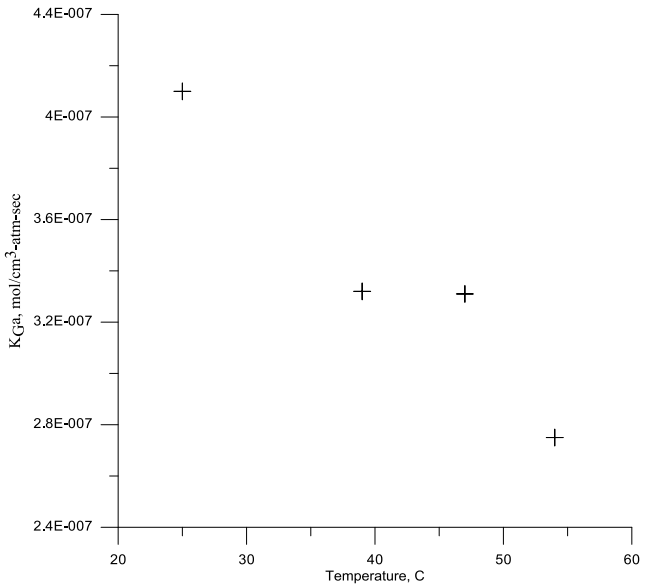

Figure 5.4. Overall mass transfer rate at different temperatures for water absorption. Operating conditions: distributor filter C (ACE glass, 25~50μm); gas flow rate = 0.5 L/min; residence time = 4.2 s; liquid holdup= 2.1 L; inlet CO_2 concentration = ~12%(v).

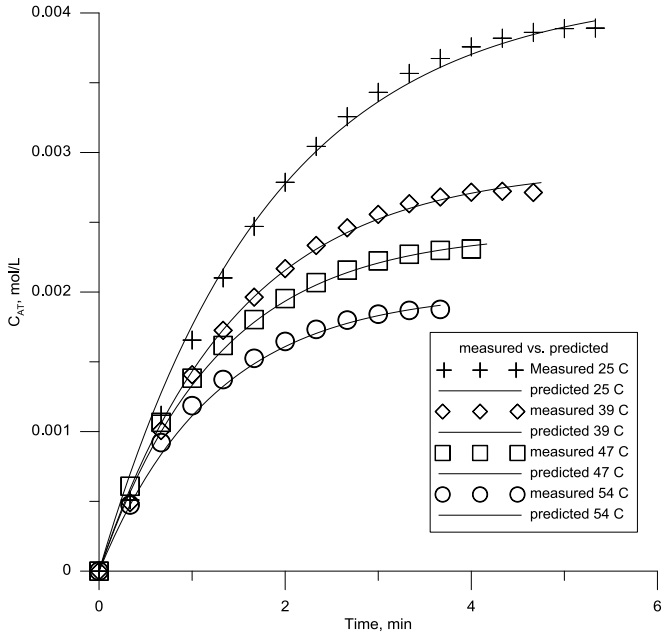

Figure 5.5. Comparison of measured and predicted values of total inorganic carbon concentration in the liquid. Operating conditions: same as Figure 5.4

5.3.2 CO_2-$Mg(OH)_2$-H_2O system

0.01, 0.025, 0.05 and 0.1 mol/L $Mg(OH)_2$ slurry solutions were tested under the temperatures of 25 and 52 ℃. Figure 5.6 is the pH profiles obtained from the different $Mg(OH)_2$ concentrations under batch tests. All the solutions started with similar initial pH values, ~10. The pH in the column dropped very fast once the CO_2 gas was introduced. This is due to the consumption of initial total alkalinity and the slow dissolution rate of $Mg(OH)_2$ particles. The pH of the slurry solution goes up due to the dissolution of the $Mg(OH)_2$ solid particles. It stopped when the consumption rate of dissolved magnesium ions equaled the dissolution rate of magnesium solid. Afterwards, the pH values continued to decrease due to a decrease in available $Mg(OH)_2$ particles, and eventually reach the equilibrium pH values. The equilibrium pH values were 7.2, 7.4, 7.7, and 8.0 for 0.01, 0.025, 0.05 and 0.1 mol/L solutions, respectively. Under these pH conditions, the carbon in the liquid is present as bicarbonate ions, resulting in a maximum stoichiometric ratio of Mg:C=1:2. These are also shown in Figure 5.7.

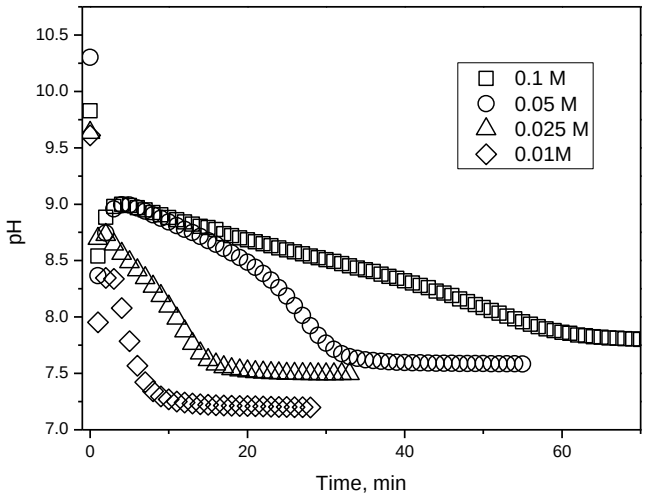

Figure 5.6. pH profiles for $Mg(OH)_2$ solutions with four different concentrations under 52 °C. Operating conditions: distributor filter C (ACE glass, 25~50 μm); gas flow rate = 0.5 L/min; residence time = 4 s; liquid holdup= 2.1 L; inlet CO_2 concentration = 12%(v); pH was measured at the top section of the bubble column.

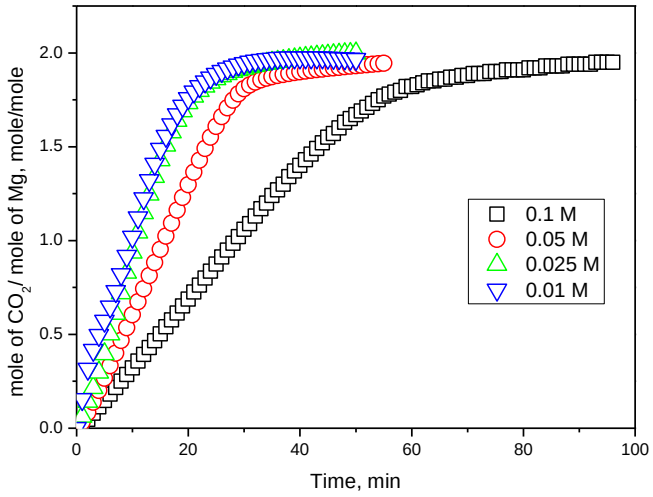

Figure 5.7. Plot of magnesium utilization of batch experiments. Operating conditions: the same as Figure 5.6.

Figure 5.8 is the CO_2 removal efficiency for $Mg(OH)_2$ solutions with four different concentrations under 52 ℃. The removal for the four solutions showed similar efficiencies during the very beginning period, ~60%. It is because the $Mg(OH)_2$ solutions between 0.01-0.1 M were initially all saturated at 52 °C, providing the same amount of OH- ions available in the solution. Then, the efficiency dropped to a certain value after consuming the initial OH- ions available in the solution. The results shown in Figure 5.8 show that 0.1 and 0.05 M solutions have much faster dissolution rates than 0.025 and 0.01 M solutions. However, a 0.1 M solution has a slightly faster dissolution rate than that of a 0.05 M solution.

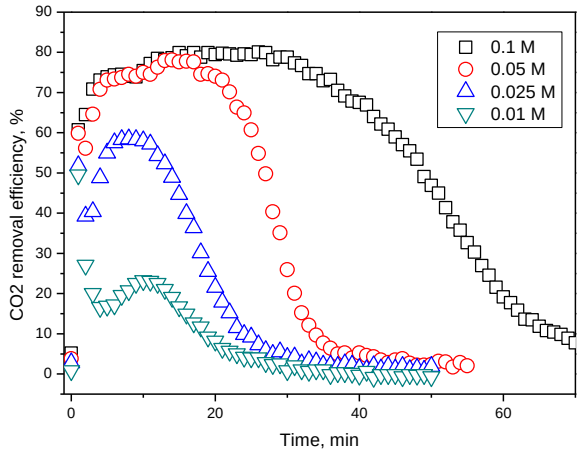

Figure 5.8. CO_2 removal efficiency for different concentration $Mg(OH)_2$ solutions for batch mode operation. Operating conditions: the same as Figure 5.6.

Figure 5.9 shows the relationship between overall mass-transfer rates and the concentrations of $Mg(OH)_2$ solutions under the temperature of 25 and 52 °C. It is found that high overall mass-transfer coefficients can be obtained at high temperatures and $Mg(OH)_2$ concentrations. However, the overall mass-transfer coefficient for a 0.1 M solution was slightly higher than that for mass transfer rate than that for a 0.05 mol/L solution at both temperatures.

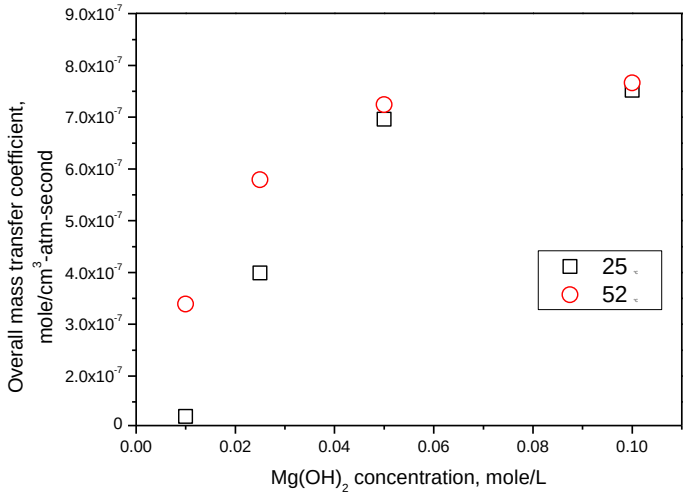

Figure 5.9. Overall mass transfer coefficients at 25 and 52 °C.

Figure 5.10 shows the predicted and measured values of total dissolved carbon in the liquid for CO_2-$Mg(OH)_2$-H_2O batch mode operations. In addition, a series of continuous tests for each

concentration are conducted. It was confirmed that the model could predict the temporal concentrations of dissolved carbon with good accuracy. Therefore, the overall mass-transfer coefficients found from these batch tests can be used to design a continuous system in the future.

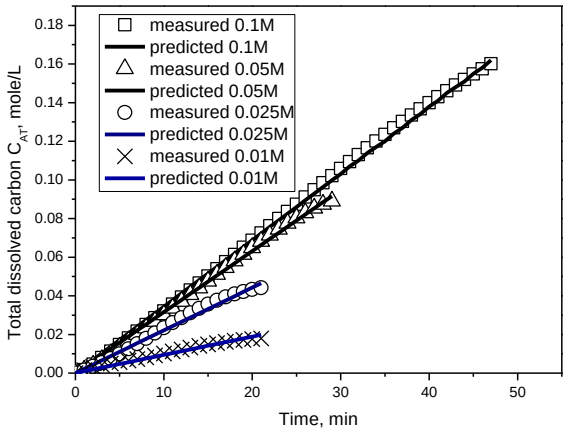

Figure 5.10. Comparison of measured and predicted values of total dissolved carbon

Table 5.2 summaries mass-transfer coefficients reported in the literature. It shows that the mass-transfer coefficients found for our system are comparable to those reported for MEA and NaOH-based absorption.

Table 5.2 Comparison of mass-transfer coefficients.

Scrubbing agent	Contacting device	Experiment conditions	Mass transfer coefficient (mol/cm^3-atm-second)
MEA-MDEA (Sema, Naami et al. 2012)	Structured DX packed column	T=25-60 ℃; $C_{MDEA/MEA}$ = 1.95/1.16, 2.1/0.8, 2.3/0.5 M	2.8E-6 to 2.5E-5
MEA (Kuntz and Aroonwilas 2009)	Spray tower and packed tower	T=25℃; C_{MEA} =3-7 M; P_{CO2} =0.05-0.15 atm	2.2E-6 to1.25E-4; 2E-6 to 4.2E-6
MEA (Luo, Hartono et al. 2011)	String of discs contactor	T=50 ℃; C_{MEA} = 5 M	8.3E-7
MEA (Chen, Shi et al. 2008; Chen 2012)	Bubble column	T=25-45 ℃; P_{CO2}=0.1-0.3 atm; C_{MEA}= 4 M	6.6E-7 to 9.1E-6
NaOH (Chen, Shi et al. 2008)	Packed column	P_{CO2}=0.1-0.3 atm; C_{NaOH}= 2 M	5.4E-7 to 7.7E-6
NH_3 (Chen 2012)	Bubble column	T=25-60℃; P_{CO2}=0.15-0.6 atm; C_{NH3}= 7.7 M	4.9E-7 to 2.1E-5
NaOH (Treybal 1967)	Packed column	C_{NaOH}= 2 M	1.02E-5
KOH (Treybal 1967)	Packed column	C_{KOH}= 2 M	1.7E-5
$Mg(OH)_2$ This work	Bubble column	T=25 and 52℃; P_{CO2}=0.12 atm; $C_{Mg(OH)2}$=0.01-0.1 M	3.4E-7 to 7.7E-7

5.3.3 Discussion of chemical absorption in $Mg(OH)_2$ solution

The CO_2 absorption in $Mg(OH)_2$ solution is a chemical absorption. The CO_2 gas dissolved in water starts to form bicarbonate and carbonate ions, and then reacts with magnesium and hydroxyl ions. Here, the CO_2 physical absorption may be characterized by Henry's Law, and viewed as rate limiting step while the ionic chemical reactions can be explained by enhancement factor. The total dissolved carbon in the liquid is a sum of the concentrations of H_2CO_3*, HCO_3^-, and CO_3^{2-}, and may be written as Equation (5.17). In a CO_2-H_2O-$Mg(OH)_2$ system, the solution pH is much higher than pure water, the effect of pH value need to be considered, and an effective Henry's law constant may be defined from Equation (5.17) as:

$$H_{e,CO2} = H_{CO2}(1 + \frac{K_1}{[H^+]} + \frac{K_1 K_2}{[H^+]^2}) \qquad (5.40)$$

Then, the total dissolved carbon in the system may now be written as:

$$C_{AT} = H_{e,CO2} P_{eq} \tag{5.41}$$

The effective Henry's law constant is always greater than the Henry's law coefficient, and depends on temperature and solution pH. For instance, at a pH value of 10.4, the effective Henry's law constant will be ~10,000 times that of the original Henry's law coefficient At a pH value of 8.7, the effective Henry's constant will be ~230 times that of the original Henry's law coefficient.

5.3.4 Carbon speciation during absorption

To validate all the results given by the NDIR CO_2 gas analyzer, carbon speciation during an absorption process was studied. CO_2 absorption was conducted in the bubble column containing a 0.1 M $Mg(OH)_2$ solution in 2.1 L under 25 or 52 °C and 1 atm. Nine samples were taken during this process to obtain the carbon distribution in the absorption process. The carbon content in gas phase, liquid phase and solid phase were determined from the CO_2 gas analyzer, HCl titration method, and CHNS analyzer. Figure 5.11 shows the carbon mass balance closure. Figure 5.12 gives the carbon distribution in the liquid and solid phases.

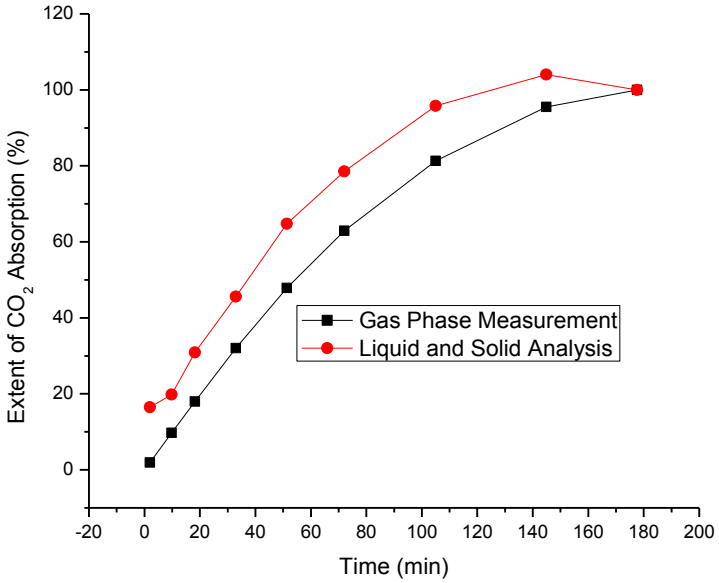

Figure 5.11. Carbon mass balance during CO_2 absorption conducted under 52 °C and 1 atm.

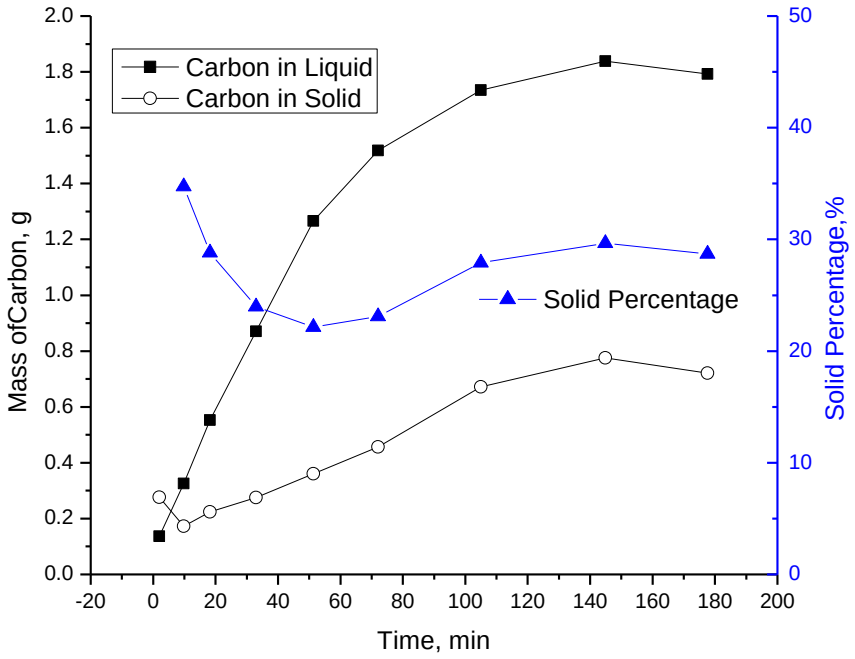

Figure 5.12. Carbon distribution in the liquid and solid phases obtained under 52 °C and 1 atm.

5.3.4.1 Carbon distribution in absorption at 25 °C

Table 5.3. Carbon mass balance at 25 °C

Time, min	pH	CO_2 removal from the gas phase, mole	HCO_3^-, mole	CO_3^{2-}, mole	$MgCO_3$ solid, mole	Unaccounted mass, %
0	9.83	0	0	00	0	0
0.5	8.15	4.4E-04	4.3E-04	2.0E-05	0	3%
1	8.54	2.0E-03	1.8E-03	5.0E-05	0	6%
1.5	8.74	3.5E-03	3.0E-03	1.2E-04	2.0E-04	4%
2	8.88	5.1E-03	4.2E-03	1.6E-04	6.0E-04	4%
2.5	8.95	6.9E-03	5.6E-03	2.2E-04	1.2E-03	2%
3	8.98	8.8E-03	7.0E-03	3.4E-04	1.7E-03	3%
3.5	8.99	1.1E-02	8.3E-03	4.5E-04	2.4E-03	5%
4	8.99	1.3E-02	9.7E-03	5.6E-04	3.8E-03	12%
4.5	8.99	1.4E-02	1.1E-02	7.8E-04	4.5E-03	13%
5	8.98	1.6E-02	1.2E-02	9.0E-04	5.0E-03	10%

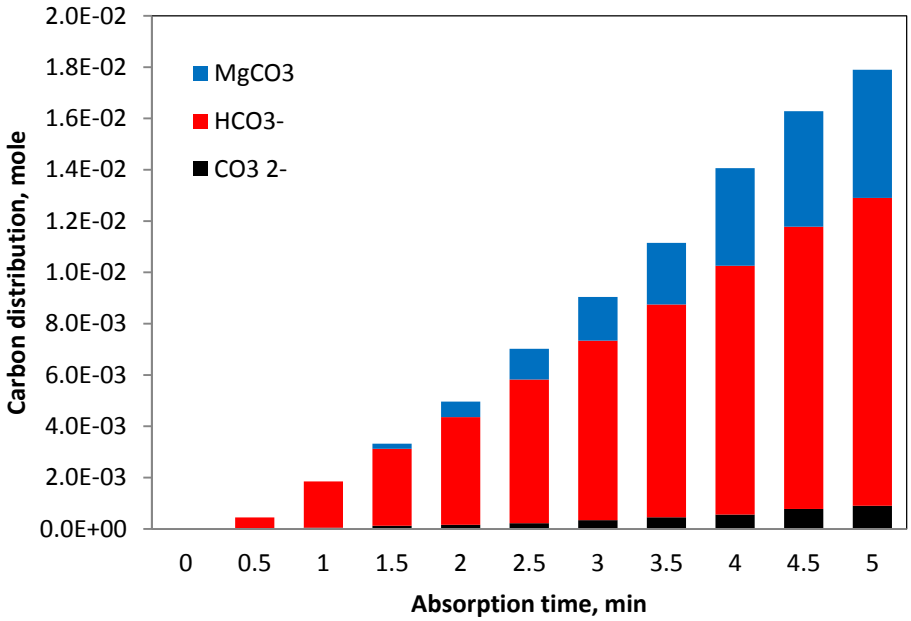

Figure 5.13. Carbon content with respect to time during absorption at 25 °C.

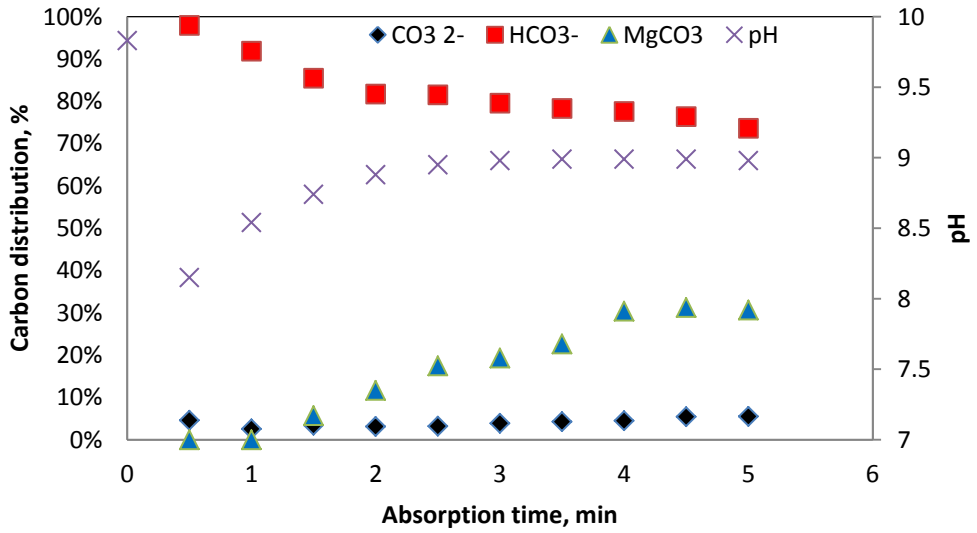

Figure 5.14. Carbon distribution and pH during absorption at 25 °C.

Table 5.3 summaries a carbon mass balance during the absorption process. The amount of CO_2 gas absorbed in the 0.1 M $Mg(OH)_2$ solution was calculated based on the CO_2 gas measurement data in the gas phase. For each sample, the carbon content in the liquid and solid phases was determined using the HCl titration method and CHNS analyzer, respectively. The bar graph in

Figure 5.13 shows an increase of individual carbon species in the solid and liquid phases with respect to absorption time. In Figure 5.14, the absorption process can be divided into three sections based on the pH profile. During the first 30 sec, the pH of the solution quickly dropped as a result of the consumption of initial alkalinity. Almost all the absorbed carbon was present as bicarbonate ions in the solution. From 30 sec to 2 min, the pH of the solution increased. In this section, a relative fraction of the bicarbonate ion in the liquid decreased with time. During this period, the carbon solid formation also increased with time by ~15%. The rest of carbon remains in the liquid phase as bicarbonate and carbonate ions. From 2 to 5 min, the dissolution rate of $Mg(OH)_2$ slows down and approached an equilibrium pH value.

5.3.4.2 Carbon speciation during absorption at 52 °C

Table 5.4. Carbon mass balance during absorption at 52 °C.

Time, min	pH	CO_2 removal from the gas phase, mole	HCO_3^-, mole	CO_3^{2-}, mole	$MgCO_3$ solid, mole	Unaccounted mass, %
0	9.46	0	0	0	0	0
0.5	8.88	1.02E-03	8.00E-04	6.00E-05	1.00E-04	6%
1	8.92	2.78E-03	2.20E-03	1.00E-04	5.00E-04	1%
1.5	8.87	4.56E-03	3.80E-03	1.20E-04	9.00E-04	6%
2	8.82	6.38E-03	5.00E-03	1.60E-04	1.00E-03	3%
2.5	8.77	8.19E-03	7.10E-03	2.00E-04	2.00E-03	7%
3	8.73	1.00E-02	8.10E-03	3.40E-04	2.20E-03	6%
3.5	8.69	1.18E-02	8.30E-03	4.50E-04	2.40E-03	6%
4	8.66	1.37E-02	9.70E-03	5.60E-04	3.80E-03	3%
4.5	8.63	1.55E-02	1.10E-02	7.80E-04	4.10E-03	2%
5	8.59	1.74E-02	1.30E-02	5.00E-04	5.00E-03	4%

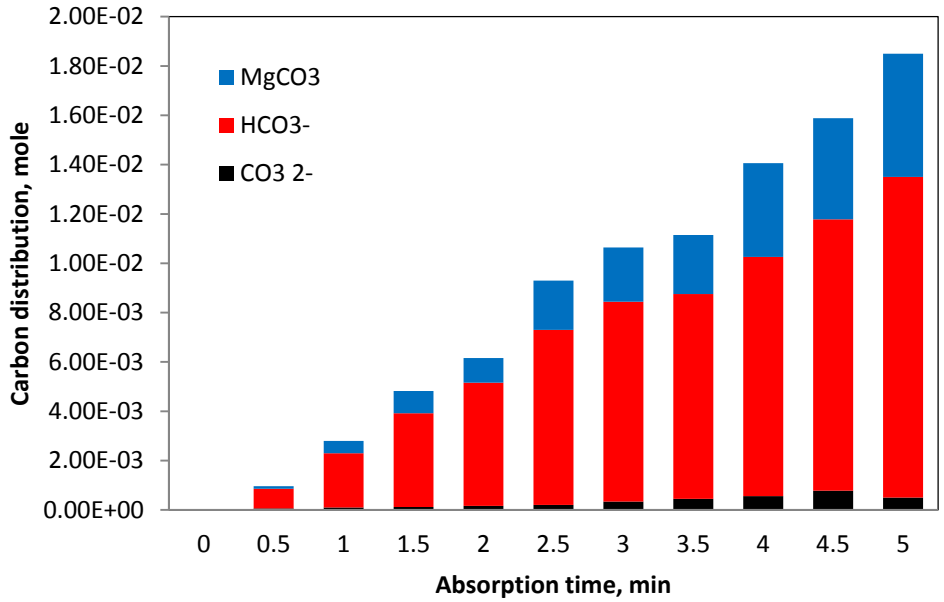

Figure 5.15. Carbon content with respect to time during absorption at 52 °C.

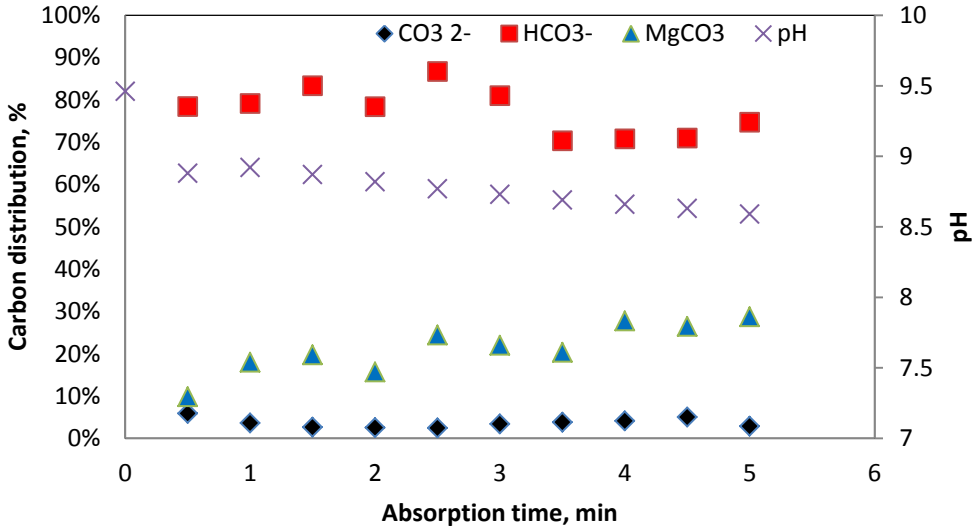

Figure 5.16. Carbon distribution and pH during absorption at 52 °C.

Table 5.4 summarizes the carbon mass balance of the absorption process at 52 °C. Overall, the bar graph in Figure 5.15 shows that the carbon content in the solid and liquid phases increases with absorption time. Compared to the result obtained at 25 °C, a higher temperature resulted in a lower equilibrium pH value of 8.7, but high dissolution rate of $Mg(OH)_2$. Since the dissolution rate of $Mg(OH)_2$ at 52 °C was faster than that at 25 °C, the pH rapidly reached an

equilibrium value. The distribution of bicarbonate ion, carbonate ion, and $MgCO_3$ solid was 70-80%, 2-5%, and 20-28% levels, respectively, at the equilibrium condition.

6. Vapor-Liquid Equilibrium (VLE) Studies

The equilibrium data for the CO_2-water-$Mg(OH)_2$ system at various temperatures, pressures and concentrations have a vital role in understanding the system and designing the absorber and stripper. For designing the absorber, the equilibrium data is also important for the determination of a liquid-to-gas ratio because the solubility of CO_2 gas at given temperature and pressure determines the amount of $Mg(OH)_2$ solution needed for the absorber to meet the specifications of treated gas. In addition, the VLE data will predict the dissolved carbon concentrations at the inlet and outlet streams from the absorber and stripper. These data are also important for the estimation of $Mg(OH)_2$ solvent degradation at various operating conditions.

This chapter presents a laboratory technique based on titration using an HCl acid to determine the equilibrium concentrations of the different inorganic carbon species in the CO_2-$Mg(OH)_2$-water system. A chemical engineering simulation software, PRO/II, has been used to predict the equilibrium concentrations for the absorber and stripper at various operating conditions.

6.1 Experimental set-up

The VLE experimental set-up consists of several sections: (1) mixed CO_2 gas; (2) bubble column absorber; (3) temperature control unit; (4) gas sampling and analysis; (5) liquid analysis unit; and (6) pH, temperature measurement and data acquisition. A schematic of the experimental set-up is shown in Figure 6.1.

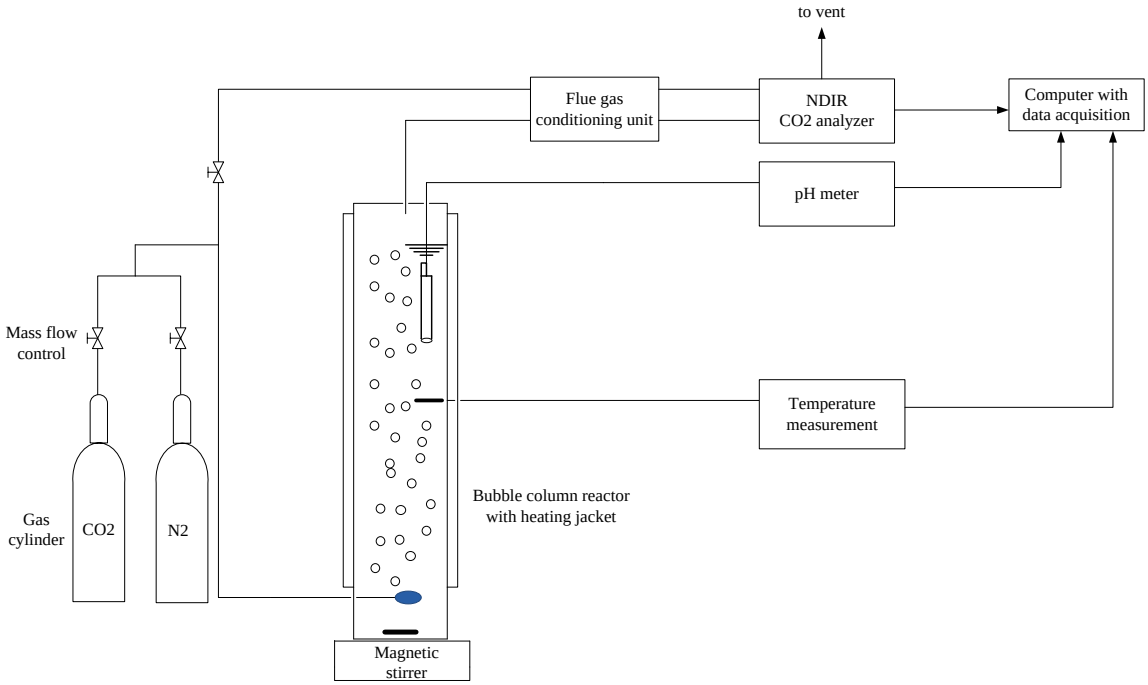

Figure 6.1. Experimental set-up for equilibrium tests.

A 35-cm-tall, 5-cm-diameter column made of Plexiglas with a heating jacket and thermal insulation was used as the main body of the bubble column reactor. Three sampling ports were located at the top, middle, and bottom of the reactor to obtain complete temperature and pH profiles of the reactor. Fritted glass size C (porosity 25-50 μm, ACE glass Inc.) was installed at the bottom of the reactor as a gas bubbler. The absorber sat on the magnetic stirrer plate which allows for mixing inside the column.

A simulated flue gas was produced by mixing a CO_2 gas with a N_2 gas (high purity >99%, Wright Brothers Inc.). Both gas streams were controlled by mass flow controllers (Thermal gas mass flow controller, Cole Parmer Inc.) in order to have a desired CO_2 gas concentration. A gas sampling system consists of an in-line flue gas conditioning unit (IMR 400 flue-gas conditioning system, Environmental Equipment Inc.) where the particles in the sample were removed by the filter, and water vapor was removed by passing through the Nafion dryer. A pretreated gas sample was then analyzed for CO_2 gas concentration by an infrared CO_2 gas analyzer (Model ZRH infrared analyzer, California Analytical Instruments Inc.) The CO_2 gas analyzer was periodically calibrated by using pure N_2 (high purity >99%, Wright Brothers Inc.), 5% CO_2 and 16% CO_2 (certified grade, CO_2 in N_2, Purity Plus Gas Inc.) standard gases.

The pH of a solution was measured by a pH meter (Model 25, Fisher Scientific Inc.). Temperatures were measured at an inlet gas stream and three locations along the bubble column for monitoring and maintaining test conditions. A computer with a data acquisition system (Model USB-1208FS, NI Instruments Inc.) was used to record the CO_2 concentrations,

temperatures, and pH values during experiments. A reagent-grade $Mg(OH)_2$ slurry was used to obtain the equilibrium data under different CO_2 partial pressures. The experiment conditions are summarized in Table 6.1.

Table 6.1 Experimental conditions for VLE test.

Parameter	Value
Inlet gas temperature	52 °C
Absorber temperature	25-95 °C
Gas flow rate	0.5 L/min
Inlet CO_2 concentration	5-16 % vol.
$Mg(OH)_2$ concentration	0.1 M
Mixing rate	1,200 RPM
Porosity of gas bubbler	25-50 μm

6.2 Experimental procedure

A CO_2 gas balanced in N_2 gas was bubbled through 45 mL of a 0.1 M $Mg(OH)_2$ solution. After an outlet CO_2 gas concentration equaled an inlet CO_2 gas concentration, the system was considered to reach an equilibrium condition under the CO_2 gas partial pressure at 1-atm total system pressure. Then dissolved inorganic carbon in the aqueous phase was quantified by a wet chemistry method (titrated by 0.1 N standard HCl acid).

6.3 PRO/II simulation

A simulation software PRO/II (version 9.0, Invensys SimSci-Esscor) was used to obtain the VLE data. Since the reaction between $Mg(OH)_2$ and CO_2 are ionic reactions, a third party chemistry thermodynamic data base OLI (Chemistry wizard 3.1, OLI engine in PROII 9.0, OLI system) was used to generate all the reactions between $Mg(OH)_2$ and CO_2. Flash reactor was selected as CO_2 absorber and stripper. The configuration of the simulation is given in Figure 6.2.

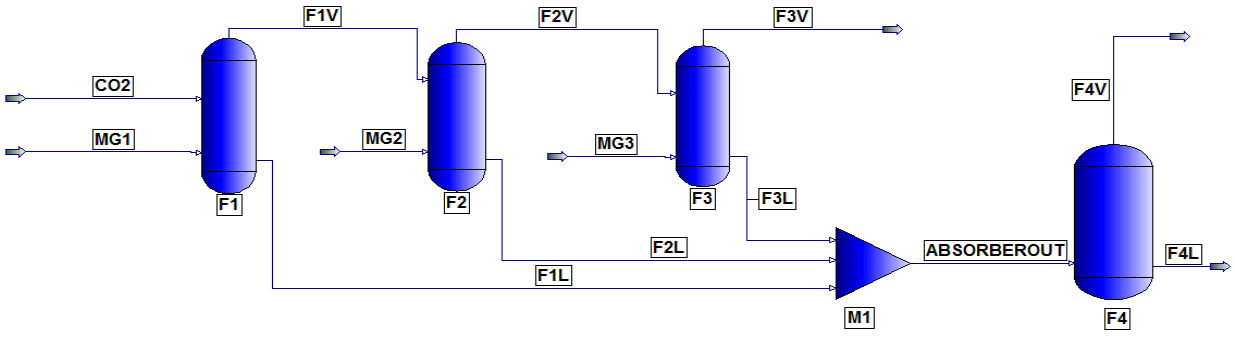

Figure 6.2. Configuration of PRO/II simulation.

6.4 Results and discussion

6.4.1 Equilibrium pH for $Mg(OH)_2$ dissolution

The solution pH will affect the dissolution of $Mg(OH)_2$, precipitation of $MgCO_3$, and distribution of carbonate and bicarbonate ions. Magnesium hydroxide in the aqueous solution will have two major reactions as shown below.

$$Mg(OH)_{2\ Solid} = Mg^{2+} + 2OH^- \quad (6.1)$$

$$K_{sp} = [Mg^{2+}][OH^-] \quad (6.2)$$

$$Mg^{2+} + OH^- = MgOH^+ \quad (6.3)$$

$$K_h = [MgOH^+]/([Mg^{2+}][OH^-]) \quad (6.4)$$

Rearrange above equations:

$$[MgOH^+] = K_h * K_{sp} * [H^+]/[K_w] \quad (6.5)$$

$$[Mg^{2+}] = K_{sp}[H^+]^2/[K_w]^2 \quad (6.6)$$

The concentration of all of the ions in the solution must satisfy the electro-neutrality equation,

$$[H^+] + 2[Mg^{2+}] + [MgOH^+] = [OH^-] \quad (6.7)$$

This can be rewritten in terms of the preceding equations:

$$(2K_{sp}/K_w^2) * [H^+]^3 + ((K_w + K_h * K_{sp})/K_w) * [H^+]^2 - K_w = 0 \quad (6.8)$$

Therefore, the system pH can be determined once these temperature dependence constants are given.

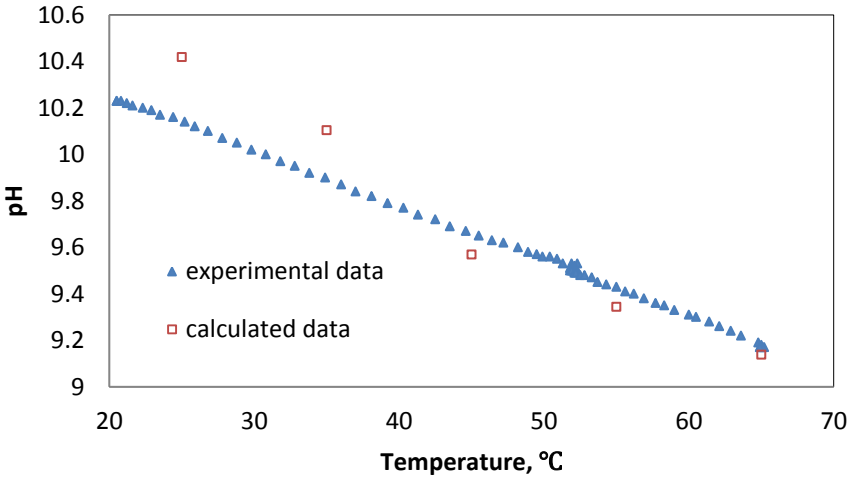

Figure 6.3 pH vs. temperature data for $Mg(OH)_2$-H_2O system.

As shown in Figure 6.3, the equilibrium pH values of a magnesium hydroxide solution at different temperatures decreased with an increase in temperature. At 52 °C of the outlet of a typical FGD outlet temperature, the equilibrium pH value of a $Mg(OH)_2$ solution is found to be ~9.5, which is still high enough to have the potential to offer an effective and sufficient CO_2 absorption rate.

6.4.2 VLE data under 1 atm of total system pressure

The 0.1 M $Mg(OH)_2$-CO_2 VLE data have been obtained under the conditions of temperatures between 25 and 95 °C and CO_2 partial pressures between 5 and 20 kPa. The results show that as temperature increases, the total dissolved carbon concentration in the liquid decreases. Under 16%(v) CO_2 gas concentration, the molar fractions of the dissolved carbon were found to be 0.0035 and 0.00025 at temperature 25 and 85 °C, respectively. This concentration difference serves as a mass-transfer driving force for the regeneration step. At a temperature of 52 °C and a 16%(v) CO_2 gas concentration, the molar fractions of the dissolved carbon were found to be 0.00005 and 0.0013 for water and 0.1 M $Mg(OH)_2$ solution, respectively. The chemical reactions between CO_2 and $Mg(OH)_2$ account for this difference, and the chemical enhancement factor has been calculated to be ~26.

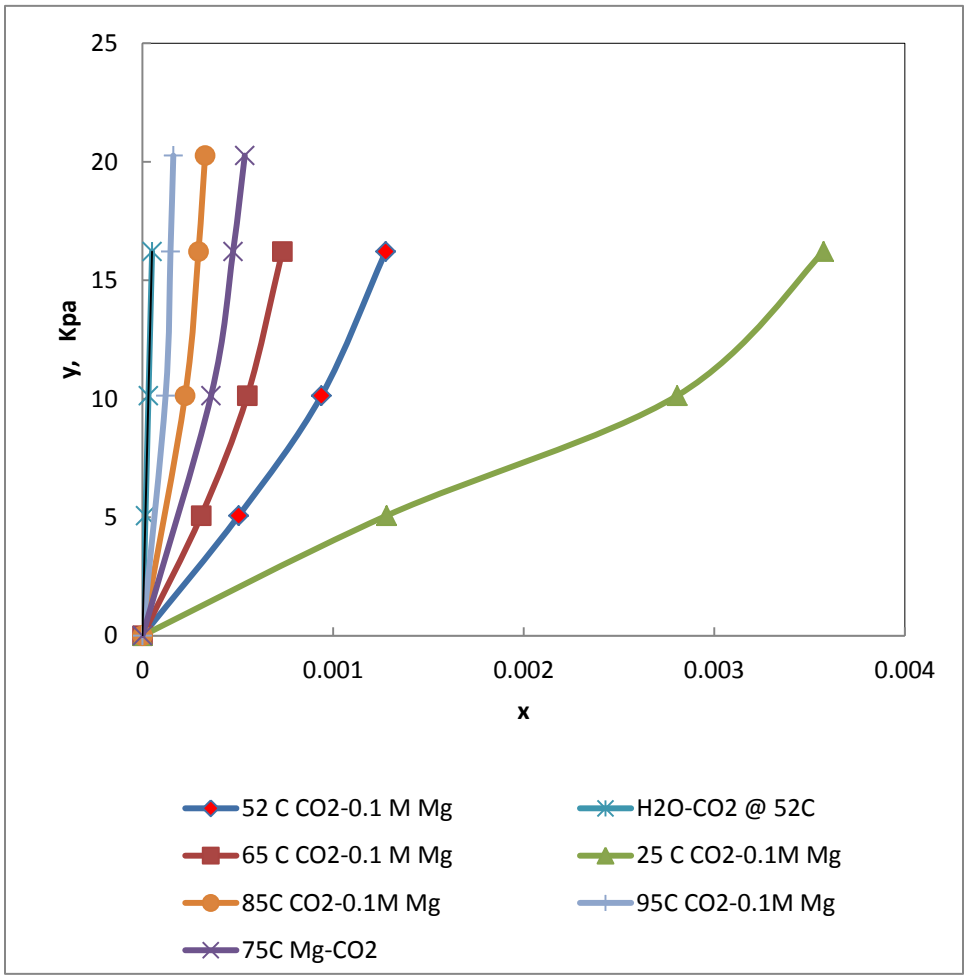

Figure 6.4 VLE data for CO_2-0.1M $Mg(OH)_2$ system at various conditions.

6.4.3 Equilibrium pH profiles for CO_2-$Mg(OH)_2$ system

The equilibrium pH values under the CO_2-$Mg(OH)_2$ system range from 7.5 to 8.5 under CO_2 partial pressures of 5–20 kPa. As temperature increased, the equilibrium pH decreased.

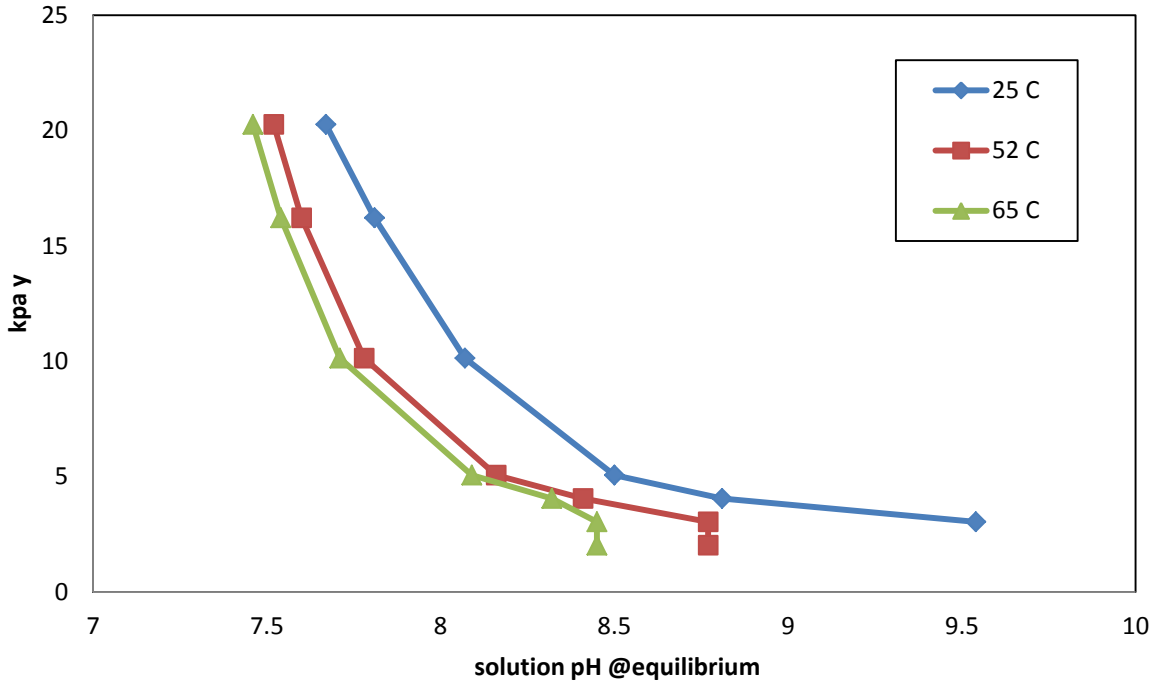

Figure 6.5 Equilibrium pH profiles at various temperatures.

6.4.4 Equilibrium distribution of dissolved inorganic carbon and magnesium compounds

The equilibrium distribution of dissolved inorganic carbon and magnesium compounds was calculated using PRO/II. In the $Mg(OH)_2$-CO_2 system, dissolved magnesium species will exist as Mg^{2+}, $MgHCO_3^-$, $MgOH^-$, and $MgCO_3$ (aq); the dissolved inorganic carbon species will exist as CO_3^{2-}, HCO_3^-, $MgHCO_3^+$, $MgCO_3$ (aq), and H_2CO_3. The CO_3^{2-} and HCO_3^- concentrations can be determined by a wet chemistry method. However, it is practically very difficult to experimentally determine carbon-bound magnesium compounds (e.g. $MgHCO_3^+$, $MgCO_3$ (aq)), and thus this equilibrium calculation method can be used to determine the distribution of such compounds.

It was found that at a pH range of 7.4 to 9, bicarbonate ions accounted for 80% of the total dissolved carbon compounds, and the highest value occurred at pH of 8.2. The carbonate species including $MgCO_3$ (aq) and CO_3^{2-} were found less than 10% of the total dissolved carbon compounds. As discussed before, bicarbonate ions were considered as the regenerable carbon species while carbonate ion thermodynamically prefer to precipitate out as $MgCO_3$ solid making it difficult to regenerate. Therefore, the operation pH range at the outlet of the absorber is preferred to be controlled at a range of 7.4 to 9 in order to make bicarbonate ions dominant species.

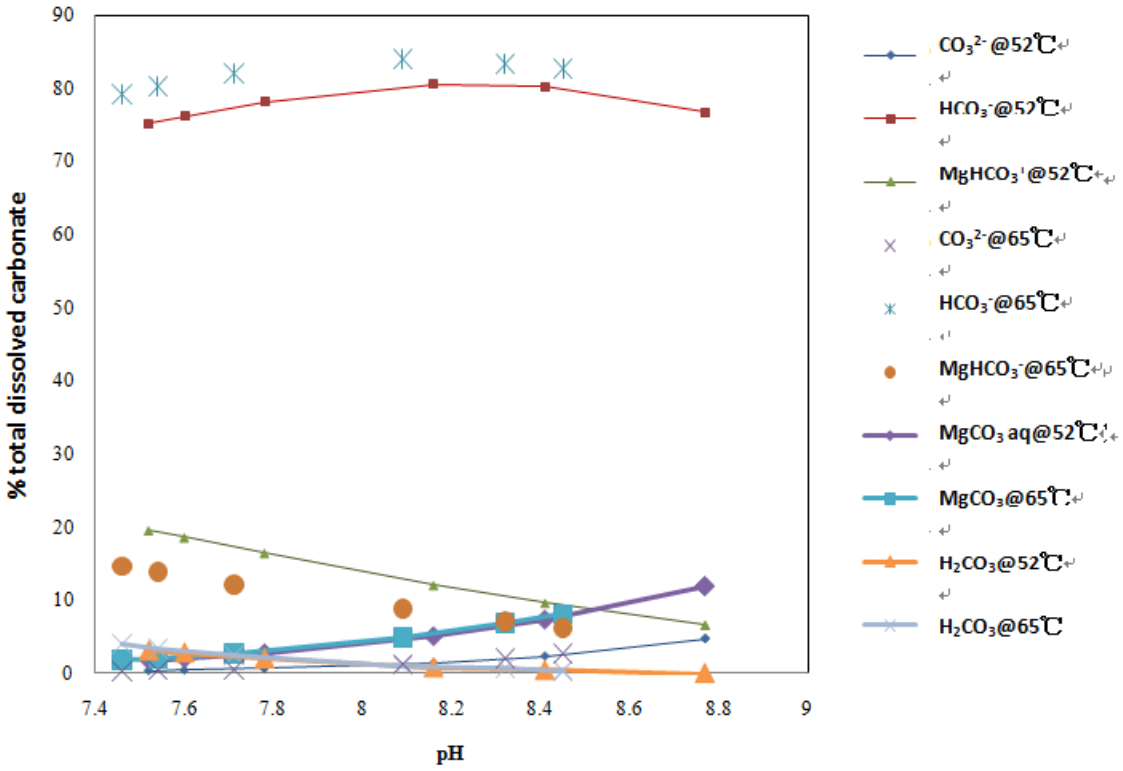

Figure 6.6 Equilibrium compositions of carbon and magnesium species as a function of pH at 52 and 65 °C.

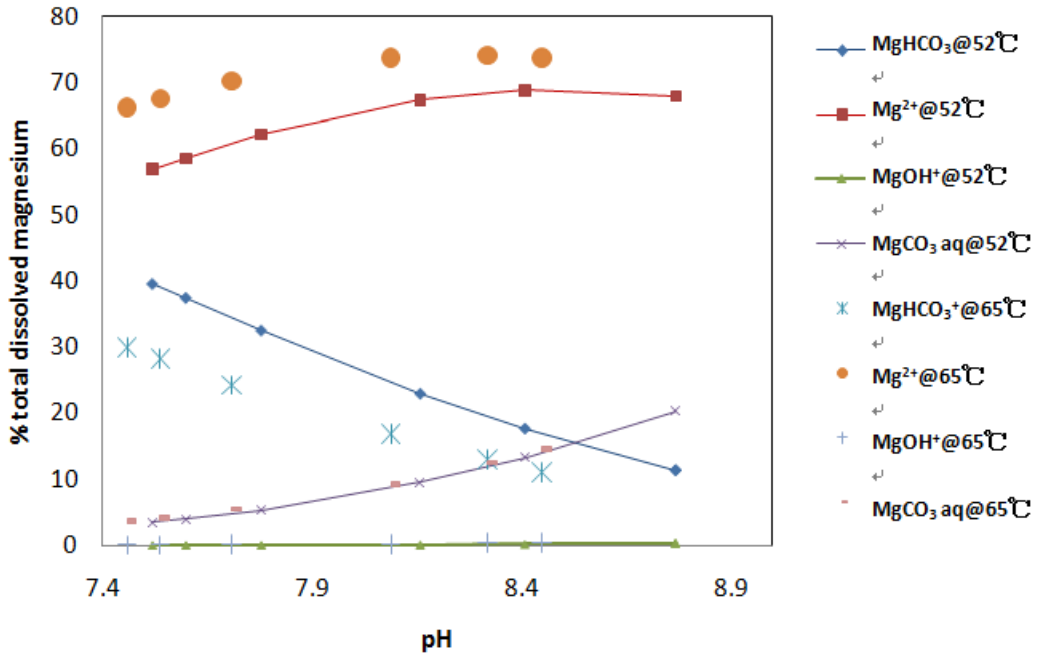

Figure 6.7 Equilibrium compositions of dissolved magnesium species as a function of pH at 52 and 65 °C.

6.4.5 Carbon speciation during desorption

To investigate the effect of temperature and pressure on the release of CO_2 gas from a rich magnesium slurry solution, the speciation of carbon during desorption was simulated at various temperatures and pressures with PRO/II.

6.4.5.1 Effects of desorption temperature

Temperature was varied from 20 to 95 °C at 1 atm of total system pressure as shown in Figure 6.8. CO_2 gas started to desorb at >~75 °C and <~20% CO_2 gas is desorbed at 95 °C. Meanwhile, up to 70% $MgCO_3$ formation was predicted at 95 °C. These results are similar to aforementioned experimental results.

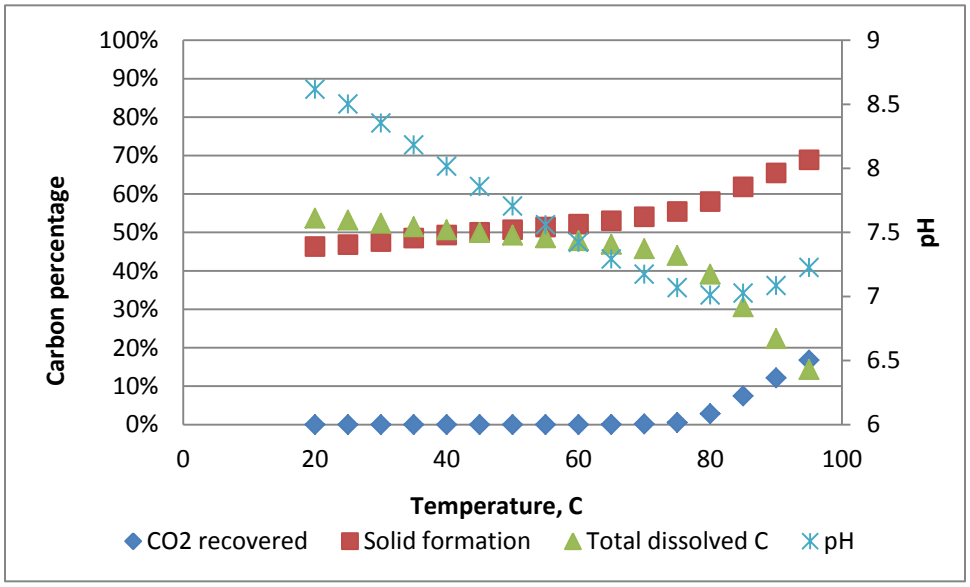

Figure 6.8 Carbon distribution between 20 and 95 °C under 1 atm.

6.4.5.2 Effects of desorption pressure

Pressure was varied from 0.3 to 2 atm at 75 °C as shown in Figure 6.9. The pressure effect was noticeable at pressures below 0.5 atm, but still <~20% CO_2 gas is recoverable at 75 °C. Overall, solid formation is identified as a major barrier for CO_2 recovery from a magnesium slurry solution.

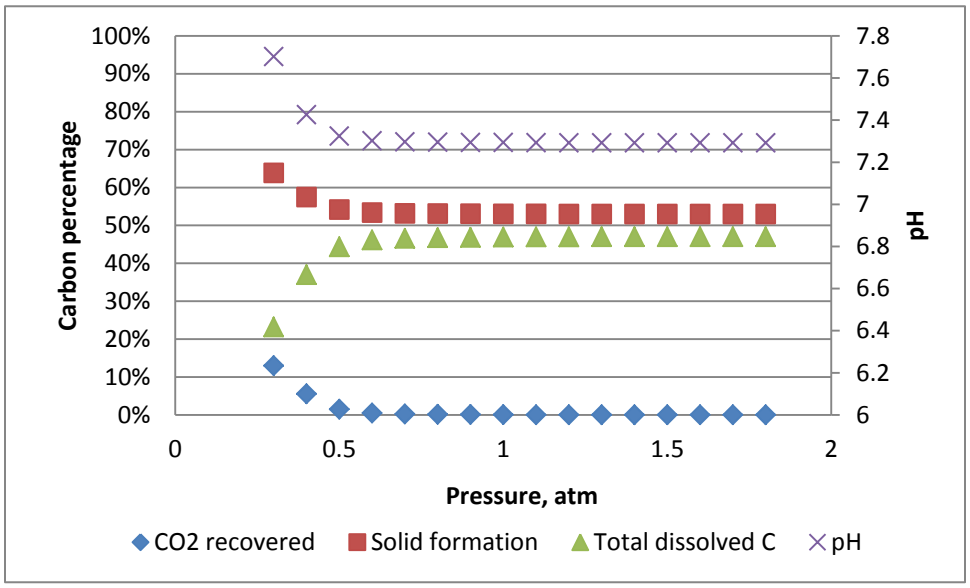

Figure 6.9 Carbon distribution between 0.3 and 2 atm at 75 °C.

7. Desorption of Rich Magnesium Solution

As mentioned in Section 2.3, it is important to maximize the magnesium utilization and improve the regeneration performance to make the CO_2 removal process self-sustainable. In this Chapter, the regeneration of rich magnesium solution was studied.

7.1 Desorption of $Mg(HCO_3)_2$

During the desorption of rich magnesium slurry solution, the formation of magnesium carbonate and the escape of CO_2 gas from the solution are important phenomena. A rich magnesium slurry solution was obtained by absorbing CO_2 gas into 0.025 M $Mg(OH)_2$ under 52 °C and 1 atm in the bubble column. Then, the rich solution mainly containing $Mg(HCO_3)_2$ was transferred to the desorber. In order to study the effect of temperature on the decomposition, different temperatures were applied, ranging from 60 to 100 °C. Nitrogen gas was used as a carrier gas flowing through the bubbler in the desorber to carry CO_2 gas to a CO_2 gas analyzer.

During the desorption process, inorganic carbon is distributed in three different phases. A titration method, NDIR analyzer and CHNS analyzer were used to analyze carbon in liquid, gas and solid phase, respectively. In the desorption process, the rich magnesium solution was first heated from 52 °C to a desired temperature, and then the desorber was kept under the temperature. Total alkalinity was obtained through titration with a 0.1 N HCl solution and a bicarbonate ion concentration was calculated based on total alkalinity and initial pH. The time "0" on the x axis in Figure 7.1 is a moment when temperature ramp stopped and reached a desired desorption temperature. Before the temperature reached a desired desorption temperature, no N_2 carrier gas was introduced.

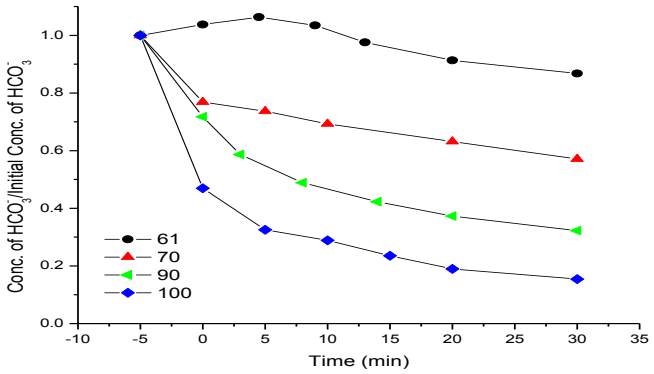

Figure 7.1 Temporal profile of bicarbonate ion concentration determined by titration.
Note: Time "-5" on the x-axis denotes a moment when rich slurry starts to be heated from 52 °C to a desired temperature. Time "0" denotes a moment when the desired temperature was reached.

Figures 7.2–7.4 shows the distribution of inorganic carbon speciation during the desorption process under three different temperatures.

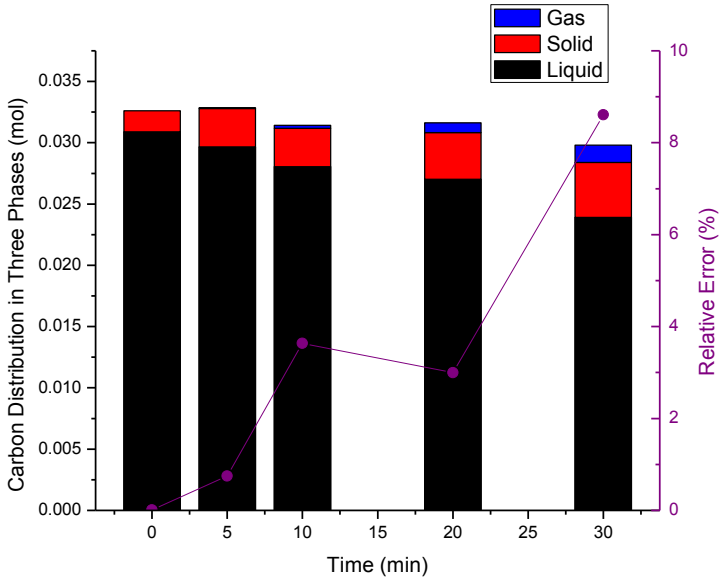

Figure 7.2 Carbon distribution in the desorption process at 70 °C.
Note: The relative errors of data are shown with absolute values.

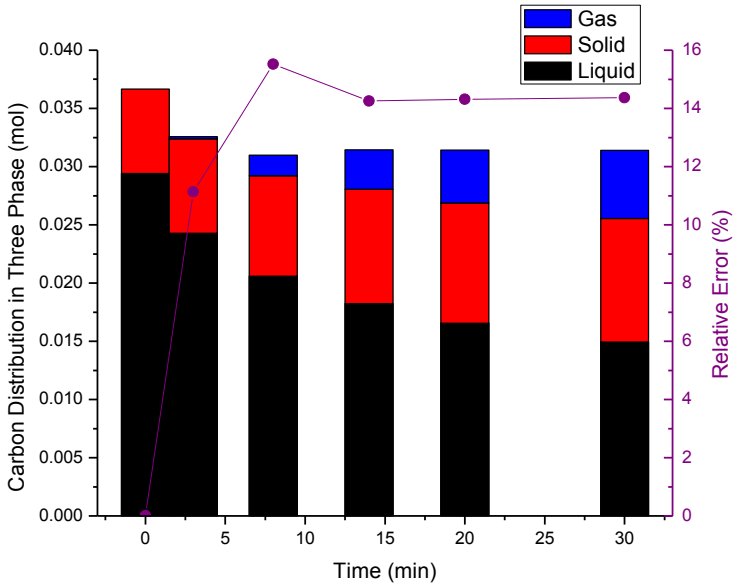

Figure 7.3 Carbon distribution in the desorption process at 90 °C.

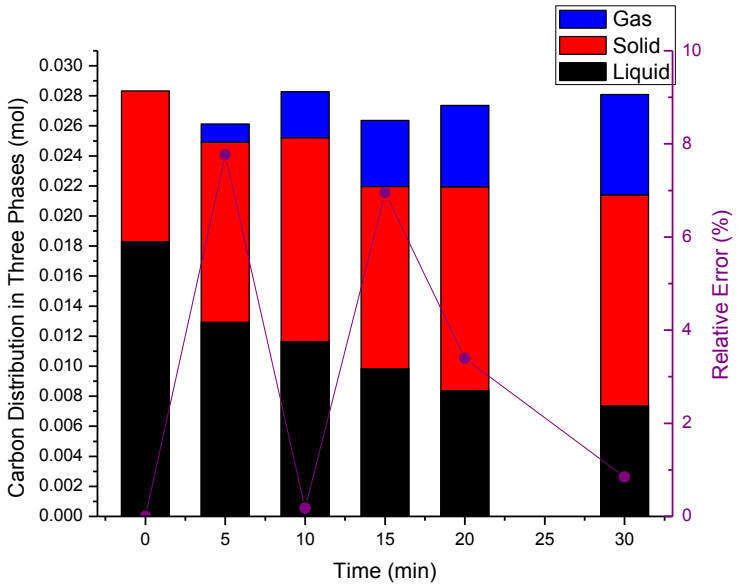

Figure 7.4 Carbon distribution in the desorption process at 100 °C.

As shown in Figure 7.1, CO_2 gas desorption from the rich slurry solution increased with an increase in temperature. Figures 7.2–7.4 also show that more CO_2 gas was released with an increase in temperature, however, at the same time, more $MgCO_3$ solid was formed and pronounced. The kinetics of $MgCO_3$ formation is discussed in Chapter 9.

7.2 Adsorption of Bicarbonate Ion Using Resin

Since $MgCO_3$ solid started to significantly form at high temperatures where CO_2 gas desorption was preferable, the adsorption of inorganic carbon species (mostly bicarbonate ion) from a rich magnesium slurry solution was attempted. Huang et al. proposed a dual alkali method to regenerate ammonia. In this method, a weakly basic ion-exchange resin containing amine functional groups is used to regenerate ammonia through absorbing carbonic acid from ammonium bicarbonate at an ambient temperature. In our experiment, a resin Amberlite IRA-67 (Polyamine, moisture: ~60%, Sigma Co.) was added to a rich slurry solution after CO_2 absorption. Samples were taken at different sampling times and inorganic carbon in the solution was analyzed using titration. Figure 7.5 shows that with higher the rich slurry concentration, the more the adsorbed inorganic carbon. After 40 min, a maximum 18% inorganic carbon was adsorbed to the resin when 18.75 g was used. The adsorption of bicarbonate ions using the resin was not significant.

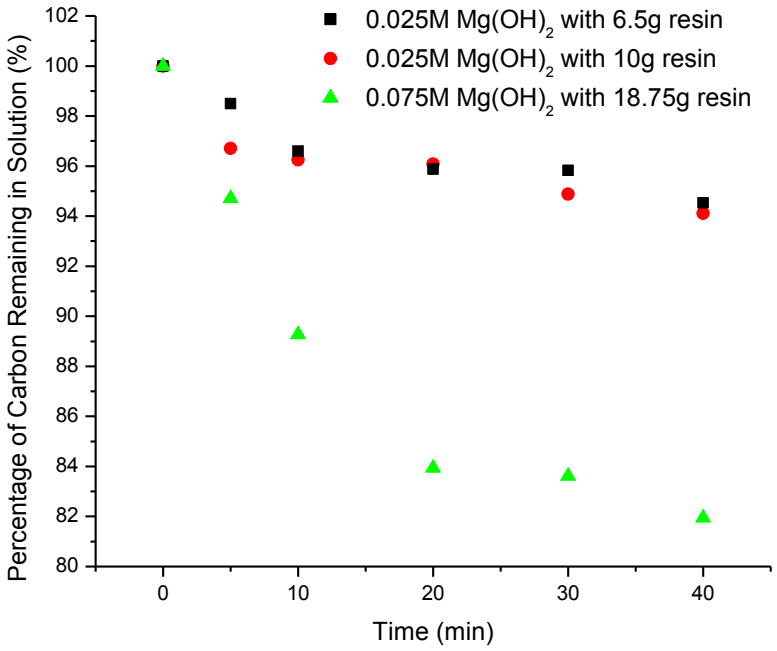

Figure 7.5 Adsorption of bicarbonate ion in terms of different rich magnesium concentrations and amounts of resin.

8. Dissolution Kinetics of Magnesium Hydroxide

8.1 Dissolution of Magnesium Hydroxide

The dissolution of mineral oxides in an aqueous environment has been studied for its potential applications in acid gas control, environmental impact study, corrosion, and drug design. Over the many years, several studies have been conducted on the dissolution of limestone for SO_2 gas control in wet Flue Gas Desulphurization (FGD) systems. Previous studies have focused on estimating the dissolution of limestone, lime and other calcium-based materials using a hydrochloric acid solution under conditions used in wet FGD systems (Wang, Keener et al. 1998; Shih, Lin et al. 2000; Gao, Guo et al. 2009; Siagi and Mbarawa 2009; Sun, Zhou et al. 2010).

A CO_2 separation process using magnesium hydroxide ($Mg(OH)_2$) slurry solutions was previously studied for absorption and desorption at 52 and 65 °C, respectively (Jung, Keener et al. 2004). The major advantages of this process include the readily available non-corrosive solvent which can also be reclaimed from the magnesium-enhanced FGD systems, no requirement for additional heating/cooling of flue gas, and potential low energy requirement for desorption (Lani 1998). However, less soluble magnesium carbonate ($MgCO_3$) could be formed and adversely impact the regeneration capacity of the solvent (Zhao, Sang et al. 2009; Hövelmann, Putnis et al. 2012). CO_2 gas absorption into $Mg(OH)_2$ solution takes place based on the following steps:

1. Diffusion of CO_2 gas through the gas film near the gas-liquid interface;
2. Dissolution of CO_2 gas in the aqueous phase;
3. Dissociation of CO_2(aq) into bicarbonate ion (HCO_3^-);
4. Dissociation of CO_2(aq) into carbonate ion (CO_3^{2-});
5. Dissolution of $Mg(OH)_2$ solid into Mg^{2+} and OH^-; and
6. Diffusion and subsequent reactions of inorganic carbon species with Mg^{2+} within the reaction zones of the liquid film.

Step 1 depends on the type of mass-transfer equipment used to bring the gas into contact with the slurry solution. Step 2 is governed by the Henry's law. Steps 3 and 4 involve proton ion generation and thus are known to almost instantaneously take place (V. Bravo, F. Camacho et al. 2002). From the above, one of the most important steps in the CO_2 absorption using $Mg(OH)_2$ slurry solution is to determine the $Mg(OH)_2$ dissolution rate for the continuous reaction of absorbed CO_2 with $Mg(OH)_2$. When $Mg(OH)_2$ solid dissolves in water (Step 5), it forms a slurry solution due to its low solubility (0.00069 g per 100 g of H_2O at 20 °C). Therefore, the dissolution rate of $Mg(OH)_2$ is very likely to be a rate-determining step in the CO_2 absorption process, and the determination of the dissolution kinetics is essential for the design and operation of $Mg(OH)_2$-based CO_2 absorption process.

Previous studies have shown that magnesium oxide (MgO) dissolution exhibits fractional orders in a range of 0−0.6 (Segall, Smart et al. 1978; Wogelius, Refson et al. 1995). The dissolution of periclase (sintered polycrystalline MgO) in dilute HCl solutions under temperatures ranging from 25 to 60 °C and very acidic pH conditions ranging from 2 to 4 reported fractional orders of 0.4−0.7 and high activation energy values of 93−101 kJ/gmol (Raschman and Fedoročková 2008). The measured dissolution rates were up to two orders of magnitude smaller than the estimated rate of external mass transfer, which indicated that the dissolution mechanism was controlled by surface chemical reaction. However, not all the dissolution kinetics reported in these previous studies was determined under the chemical reaction control regime. In addition, the kinetic expressions were determined under the pH and temperature conditions, which are different from those that can be used for CO_2 absorption.

The objective of this study is to determine the intrinsic dissolution kinetics of $Mg(OH)_2$ for CO_2 absorption. After determining a mixing condition where mass-transfer resistance becomes negligible, a series of pH stat experiments was conducted under different pH and temperature conditions. A shrinking-core model was used to determine the reaction rate constant and order under a pH range of 7.6–9.6 at room temperature and a pH range of 7.6–9 at a temperature range of 32–52 °C, from which the true activation energy was also determined. The difference in the pH ranges is due to a decrease in the equilibrium pH of the system with an increase in temperature.

8.2. Experiment

The dissolution rate of $Mg(OH)_2$ was determined by using a pH stat device [Cole Parmer Chemcadet] where the dissolution rate was correlated with the rate of HCl acid consumption required to maintain a preset value of pH. The dissolution of $Mg(OH)_2$ by HCl titration is widely represented by the following reaction stoichiometry (Raschman and Fedoročková 2004; Raschman and Fedorockova 2006):

$$Mg(OH)_2 + 2HCl \rightarrow MgCl_2 + 2H_2O \qquad (8.1)$$

$MgCl_2$ is highly soluble in water (54 g/100 mL water at 20 °C) and does not interfere with the dissolution process of $Mg(OH)_2$ (Fedoročková and Raschman 2008; Raschman and Fedoročková 2008). It may be worthwhile to mention that HCl acid is not used for CO_2 absorption with a $Mg(OH)_2$ solution, and is used to determine the dissolution kinetics of $Mg(OH)_2$ in this study. The direct use of CO_2 gas may interfere with $Mg(OH)_2$ dissolution by potential formation of much less soluble $MgCO_3$, which can be deposited onto $Mg(OH)_2$ surfaces. For the same reason, HCl acid has also been used for the dissolution kinetic studies of $CaCO_3$ and $Ca(OH)_2$ since the reaction product $CaCl_2$ does not interfere with the dissolution because of its high solubility. An experimental apparatus was set up as shown in Figure 8.1, consisting of pH

control, temperature control, and acid consumption measurement. The pH stat activated an acid pump (Walchem Diaphragm Pump, Cole Parmer) when a pH value was above a preset value. The pH values were controlled within ±0.2 during the entire experiment. When the acid pump delivered an HCl solution into the beaker, the reduced HCl solution weight (i.e. consumption) was recorded with a balance as shown in Figure 8.2. A 0.01 N HCl solution was used to provide pH control during the dissolution experiment. The pH and weight readings were recorded by means of a data acquisition system (Labview, version 2011, National Instruments Corp.). The temperature of the $Mg(OH)_2$ solution was kept constant in a water bath within ±0.5 °C for all experiments. Different temperatures of 22, 32, 42 and 52 °C were used to obtain the dissolution results, but an adiabatic saturation temperature of 52 °C after a wet flue gas desulfurization system was considered a temperature to be used for CO_2 absorber operation (Cooper and Alley 2011).

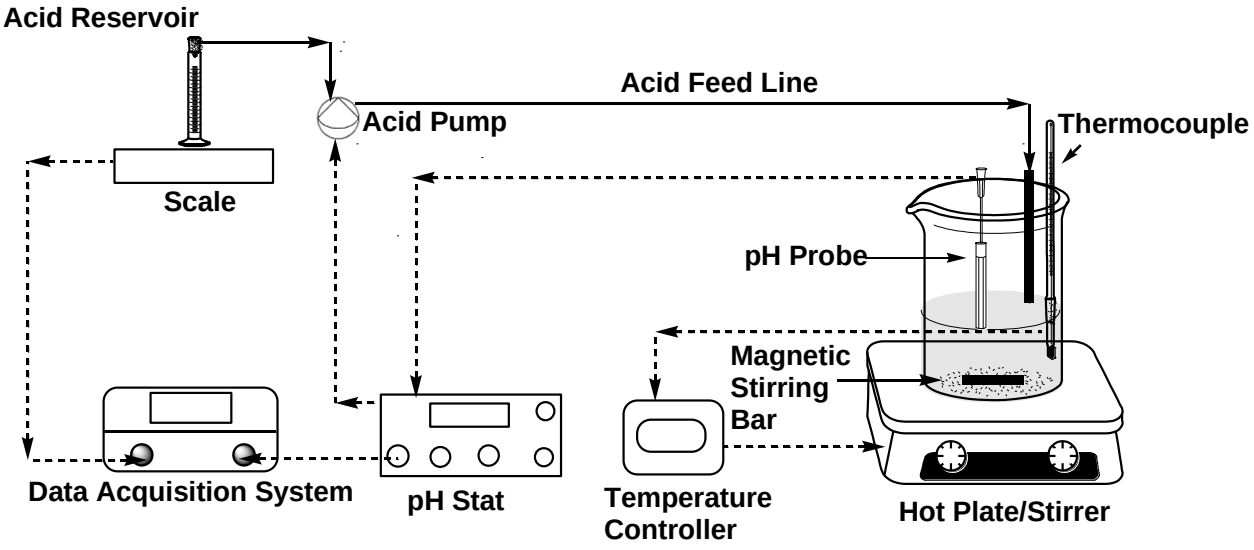

Figure 8.1. Schematic of the dissolution experimental set-up.

Pure distilled water was used in all experiments, and a pH probe was immersed in 250 mL of distilled water. The pH, temperature, and agitation speed were set to preset values and 0.145 g of magnesium hydroxide powder (reagent grade, >95% purity, average particle size = 6.0 μm, Fisher Scientific) was added to make a 0.01 M $Mg(OH)_2$ solution. The average particle sizes during the experiment were determined by taking a 10-mL sample using a laser particle size analyzer (Spectrex PC-2000). A magnetic stirrer was used to provide agitation for $Mg(OH)_2$ solution.

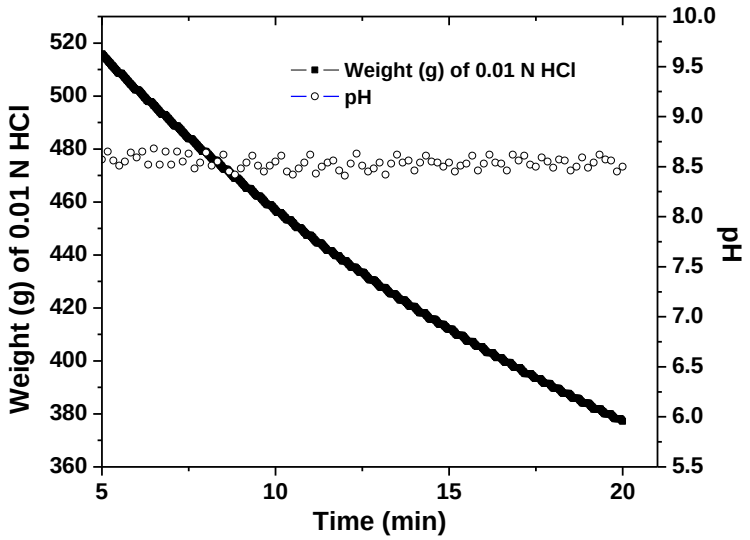

Figure 8.2. HCl consumption rate: weight of 0.01 N HCl solution and pH with respect to time.

8.3. Dissolution Model

A shrinking-core model is suitable for describing the dissolution reaction of nonporous and spherical $Mg(OH)_2$ particles in the aqueous phase (Lindman and Simonsson 1979). For this reaction, the following steps take place in series (Levenspiel 2007):

a) Diffusion of the reactant H^+ ions from the bulk liquid phase through the liquid film to the solid surface;
b) Reaction of H^+ ions with $Mg(OH)_2$ solid particle; and
c) Diffusion of the reaction products from the solid surface back into the bulk liquid phase.

The dissolution reaction can be controlled by either surface chemical reaction or liquid film diffusion. The identification of a rate-controlling mechanism is essential for the development of a fractional conversion equation using the shrinking-core model. A common approach is to plot the kinetic data of r/R (radius of particle at time t/initial radius) with respect to t/τ (time taken for a particle to reach radius of r/time taken for complete dissolution) and compare the results with model predicted curves for reaction and diffusion control, respectively.

When the chemical reaction in Eq. (8.1) controls the entire dissolution process, Eq. (8.2) can be used to predict the fractional conversion of the particle.

$$r_B = -\frac{1}{4\pi r^2}\frac{dN_B}{dt} = -\frac{1}{4\pi r^2}\frac{b\,dN_A}{dt} = b\,k^{''}C_{Al}^{n} \tag{8.2}$$

where r is the radius of the unreacted $Mg(OH)_2$ particle; dN is the moles of a reactant disappearing by the reaction; the subscripts A and B refer to HCl and $Mg(OH)_2$, respectively; b is the stoichiometric ratio of $Mg(OH)_2$ to HCl (i.e. ½); $k^{''}$ is the rate constant for the surface reaction; n is the reaction order; and C_{Al} is the concentration of H^+ ion in the aqueous phase. The number of moles of $Mg(OH)_2$ and HCl are stoichiometrically related as follows:

$$-dN_B = -b\,dN_A = -\rho_B dV = -4\pi\rho_B r^2 dr \tag{8.3}$$

where ρ_B is the molar density of $Mg(OH)_2$. The time required for the radius of the unreacted particle can be obtained by combining Eq. (8.3) with Eq. (8.2) and integrating the equation from t=0 to any time t.

$$t = \frac{2\rho_B R}{k^{''}C_{Al}^{n}}\left(1-\frac{r}{R}\right) = \tau\left(1-\frac{r}{R}\right) \tag{8.4}$$

where R is the initial particle radius, and τ is the time required for complete dissolution of the particle determined at r = 0. The fractional conversion and radius of the particle are related as shown in Eq. (8.5).

$$1 - X_B \equiv \left(\frac{\text{volume of unreacted core}}{\text{initial volume of the particle}}\right) = \left(\frac{r}{R}\right)^3 \tag{8.5}$$

From Eqs. (8.4) and (8.5),

$$\frac{t}{\tau} = t\,k_r = 1-(1-X_B)^{1/3} = 1-\left(\frac{r}{R}\right) \tag{8.6}$$

where k_r is defined as the apparent reaction rate constant in 1/time. The value of k_r can be calculated from the slope of a plot for $1-(1-X_B)^{1/3}$ with respect to time under constant pH and temperature values. The fractional conversion X_B can be obtained from HCl consumption. If the dissolution reaction is controlled by mass transfer within the liquid film for particles smaller than ~100 μm, the following conversion relationship holds (Levenspiel 2007):

$$\frac{t}{\tau} = t\,k_r = 1-(1-X_B)^{2/3} = 1-\left(\frac{r}{R}\right)^2 \tag{8.7}$$

where $\tau = \dfrac{\rho_B R^2}{C_{Al} D_A}$ and D_A = molecular diffusivity for H^+ ion

8.4 Results and Discussion

8.4.1 Effect of mixing

Mixing is critical to determining a rate-controlling regime in the $Mg(OH)_2$ dissolution reaction. Figure 8.3 illustrates the apparent rate constant, k_r, determined under both reaction and diffusion control regimes in terms of different agitation speeds under a constant pH value of 8.6 and a temperature of 52 °C. Agitation speeds below 500 rpm resulted in unstable pH control due to non-uniform particle suspension. The rate constant under both control regimes increased with an increase in the agitation speed from 500 to 700 rpm and did not increase above 700 rpm, suggesting that the mass-transfer resistance did not decrease any further.

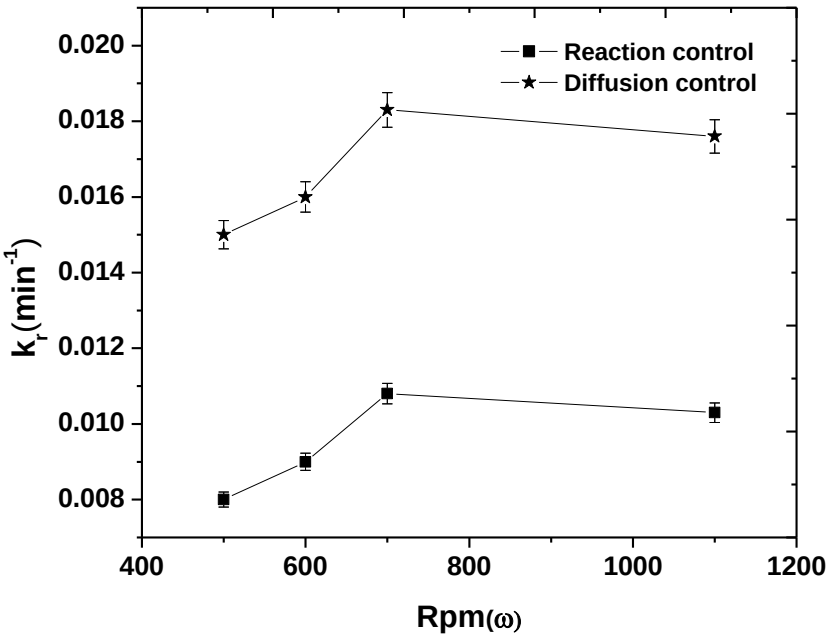

Figure 8.3. Effect of agitation speed on dissolution at 52 °C.

Based on these mixing results, the rate-controlling regime was examined in the absence of pH control at 52 °C using a 700-rpm stirring speed with 15 and 30 strokes/min of a 0.01 M HCl solution until all the particles were completely dissolved. The two flow rates cover a range of the HCl solution used for all experiments under pH control. The shrinking particle size was measured at every 5 or 10 min over the entire dissolution process in the absence of pH control as shown in Figure 8.4. In general, the dissolution results indicate that the chemical reaction is a rate-controlling step under or at 700-rpm stirring speed. Therefore, all experiments were carried out under or at 700 rpm to obtain the intrinsic dissolution kinetics. When the pH value of the magnesium solution is controlled, it eventually reaches an equilibrium state at a certain

temperature where $Mg(OH)_2$ does not dissolve and thus an additional HCl solution is not required any further. Therefore, the dissolution kinetics under a constant pH value was determined from an acid consumption rate between 5 and 20 min where chemical reaction control is warranted.

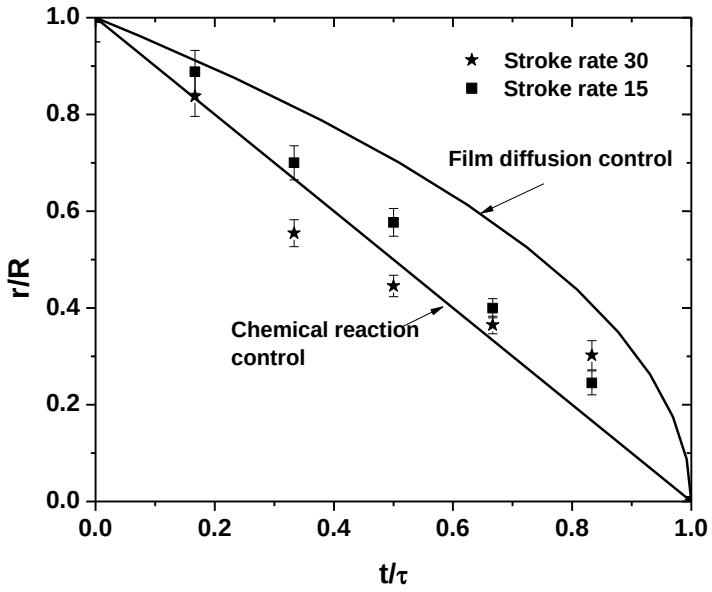

Figure 8.4. Determination of a rate-controlling step for $Mg(OH)_2$ dissolution at 52 °C and 700 rpm.

8.4.2 Effect of pH

The effect of pH was investigated between a pH range of 7.6 and 9.0 at 52 °C and 700 rpm with 0.01 M HCl and $Mg(OH)_2$ solutions as shown in Figure 8.5. It is evident from Figure 8.5 that the apparent reaction rate constant (k_r) derived from the reaction control regime increases with a decrease in pH values. It is because higher H^+ ion concentrations at lower pH values lead to faster dissolution reaction rates with $Mg(OH)_2$ particles.

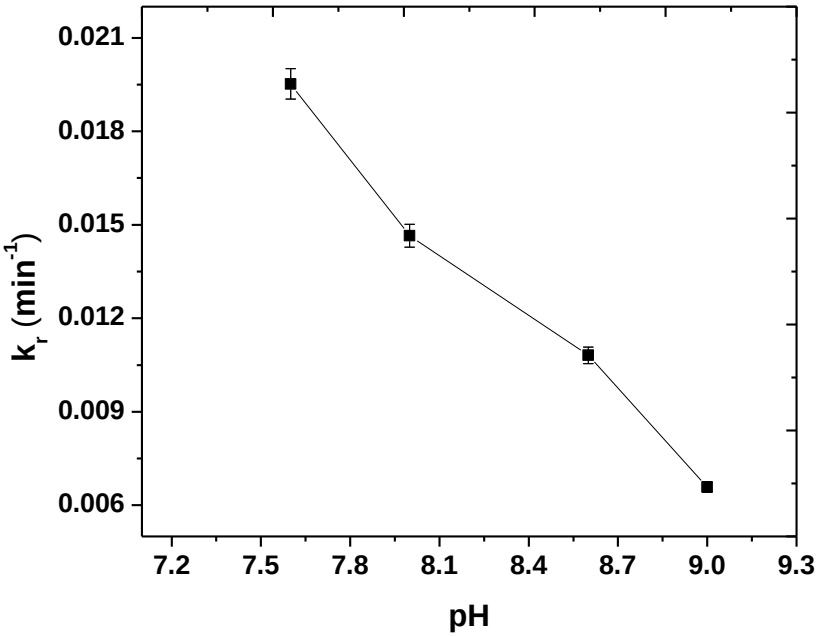

Figure 8.5. Effect of pH on dissolution at 52 °C and 700 rpm.

8.4.3 Effect of temperature

The dissolution of $Mg(OH)_2$ was studied between 22 and 52 °C at pH 8.6, 700 rpm with 0.01 M HCl and $Mg(OH)_2$ solutions. The $Mg(OH)_2$ dissolution rate dramatically increased with an increase in temperature and temperature was found to give the most significant difference in dissolution rates. When the temperature was raised from 22 to 52 °C, the apparent reaction rate constant (k_r) increased by a factor of 5.4 at pH 8.6 as shown in the Arrhenius plot in Figure 8.6. The observed activation energy determined at a pH value of 8.6 was 42±6 kJ/gmol, which is comparable with a reported value of 46 kJ/gmol at similar temperatures for magnesium-based materials obtained under the chemical reaction control regime (Rutto and Enweremadu 2011). A diffusion-controlled process is only moderately dependent on temperature because the diffusion coefficient for liquids is linearly dependent on temperature (Bird, Stewart et al. 2002). By contrast, a chemical reaction-controlled process is strongly dependent on temperature because it strongly depends on the Arrhenius law (Aydogan, Erdemoglu et al. 2007). Diffusion- and chemical reaction-controlled dissolution processes are reported to have activation energies lower than 20 kJ/gmol and between 40 to 80 kJ/gmol, respectively (Abdel-Aal 2000; Siagi and Mbarawa 2009). These previous findings also support that this dissolution study was carried out in the chemical reaction control regime.

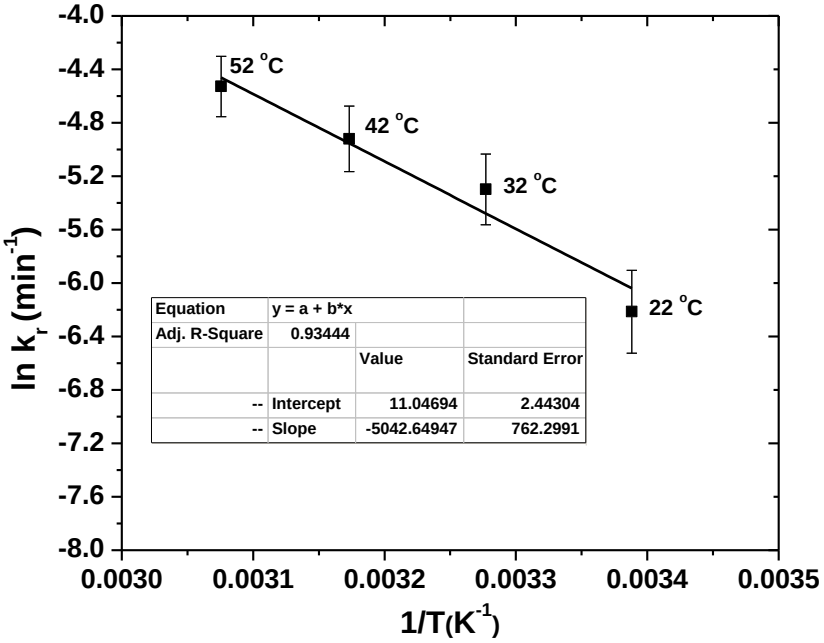

Figure 8.6. Determination of observed activation energy at pH = 8.6.

8.4.4 Intrinsic $Mg(OH)_2$ dissolution kinetics

An intrinsic kinetic expression for $Mg(OH)_2$ dissolution reaction can be determined from the apparent reaction rate constant (k_r) in Eq. (8.8) obtained under the chemical reaction control regime.

$$k_r = \frac{k'' C_{Al}^n}{2 \rho_B R} \tag{8.8}$$

When the experimental data obtained at a temperature and different constant pH values were plotted for a first-order reaction, the intrinsic reaction rate constant (k'') varied under different H^+ ion concentrations (i.e. C_{Al}). This implies that the dissolution reaction shown in Eq. (8.1) is a non-elementary reaction, and must involve a sequence of multi-step elementary reactions on the surface. Therefore, the fractional reaction order (n) was introduced to Eq. (8.8).

Little has been reported about the surface chemical reactions and species formed during $Mg(OH)_2$ dissolution. However, it was demonstrated that the three magnesium species of $MgOH^0$, $MgOH_2^+$, and MgO^- could be formed during the dissolution (Pokrovsky and Schott 2004). Among the species, $MgOH^0$ and $MgOH_2^+$ were postulated to be the predominant surface species for a pH range of 7.6–9.6 used in our study. It was also concluded that the increase of $Mg(OH)_2$ dissolution could be attributed to the protonation of $MgOH^0$ leading to the

formation of $MgOH_2^+$, a precursor surface complex. These previous study results suggest that the following two surface reactions in Eqs. (8.9) and (8.10) very likely take place in series during the dissolution.

$$MgOH^0 + H^+ \rightarrow MgOH_2^+ \tag{8.9}$$

$$MgOH_2^+ \rightarrow Mg^{2+} + H_2O \tag{8.10}$$

Taking logarithms on both sides of Eq. (8.8) gives Eq. (8.11).

$$\ln k_r = \ln\left(\frac{k''}{2\rho_B R}\right) + n \ln C_{Al} \tag{8.11}$$

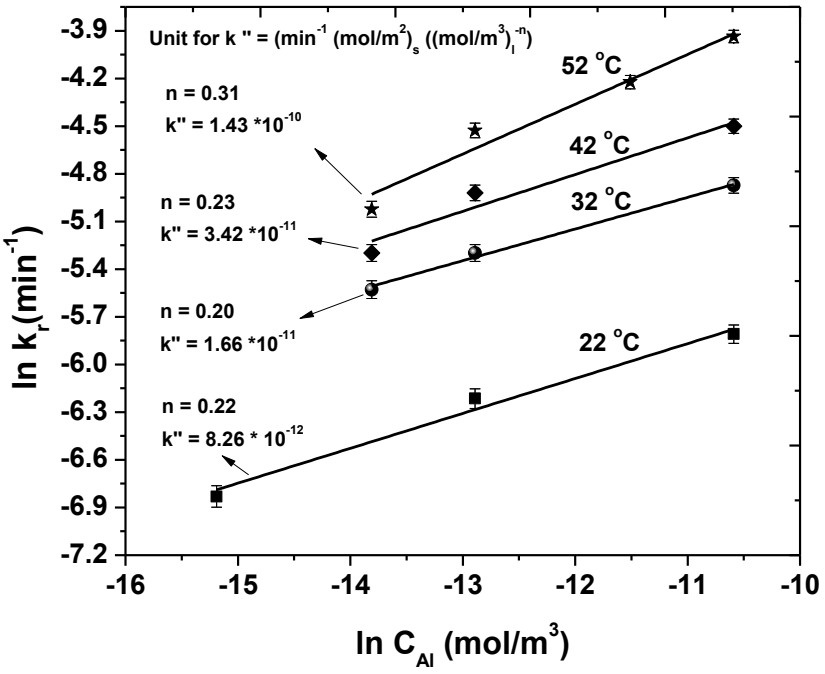

Figure 8.7. Determination of reaction order (n) and reaction rate constant (k'') between 22 and 52 °C.

The reaction order (n) was determined from the slope of the plot for k_r shown in Figure 8.7 at different temperatures of 22, 32, 42, and 52 °C and different H^+ ion concentrations between 7.6–9.6 at 22 °C and 7.6–9 at higher temperatures. The reaction order (n) values determined were 0.22 at 22 °C, 0.20 at 32 °C, 0.23 at 42 °C, and 0.31 at 52 °C, from which the arithmetic average n value was found to be 0.24. These reaction order values are within a range of the fractional

order values less than 0.7 reported for MgO dissolution (Segall, Smart et al. 1978; Wogelius, Refson et al. 1995; Raschman and Fedoročková 2008). The reaction rate constant values (k″ with a unit of $min^{-1}\cdot(gmol/m^2)_s\cdot(gmol/m^3)_l^{-n}$) determined from the intercept values were 8.26×10^{-12} at 22 °C, 1.66×10^{-11} at 32 °C, 3.42×10^{-11} at 42 °C and 1.43×10^{-10} at 52 °C. From these intrinsic reaction rate constant values, the true activation energy and frequency factor were found to be 76±11 kJ/gmol and 220 $min^{-1}\cdot(gmol/m^2)_s\cdot(gmol/m^3)_l^{-n}$ from the Arrhenius equation, respectively, as shown in Figure 8.8. This activation energy value is comparable to a value of 60±12 kJ/gmol reported for natural brucite crystals obtained between 21 and 35 °C where negligible mass-transfer resistance was not warranted . With the activation energy and frequency factor, the intrinsic $Mg(OH)_2$ dissolution reaction kinetic expression was completed as shown in Eq. (8.12).

$$r_B = bk''C_{Al}^n = b^{1-n}k''C_{Bl}^n = b^{1-n}k_0\exp\left(\frac{-E_a}{RT}\right)C_{Bl}^n$$
$$= 130\exp\left(-\frac{9{,}192}{T}\right)C_{Bl}^{0.24} \qquad (8.12)$$

where T is in K; C_{Bl} is in $gmol/m^3$; and r_B is in $gmol/(m^2\cdot min)$. The shrinking particle radius predicted by the intrinsic kinetic expression was compared with the experimentally measured particle radius during the dissolution process as shown in Figure 8.9. The model prediction result shows a good agreement with the measured data.

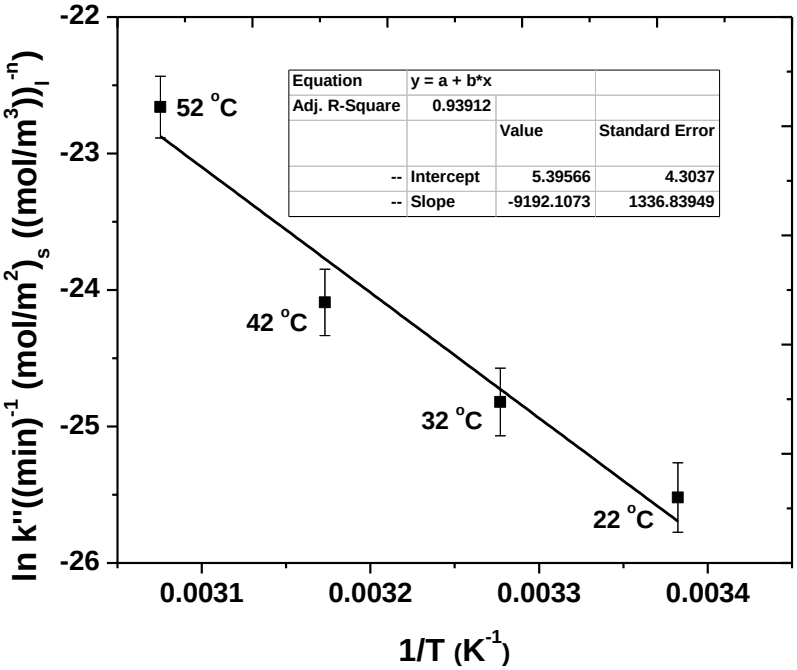

Figure 8.8. Determination of intrinsic activation energy.

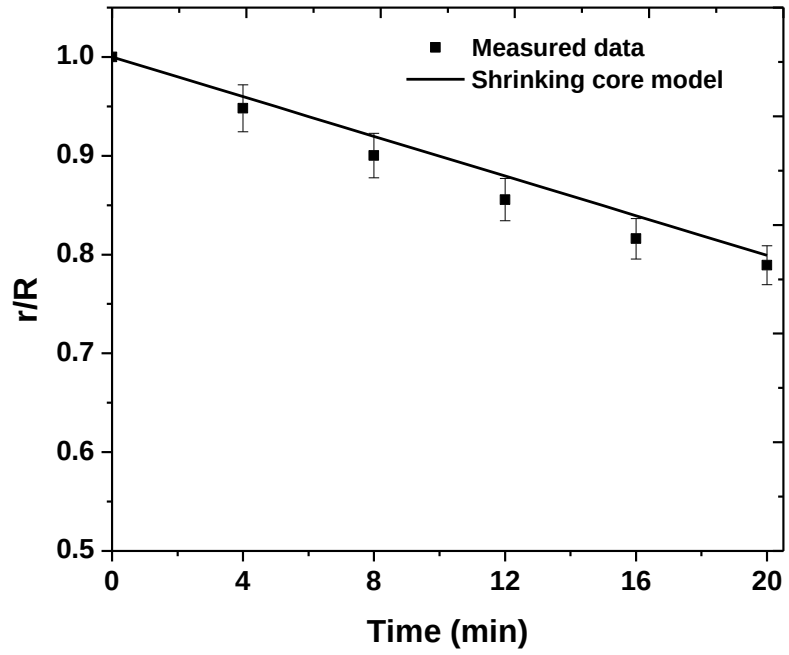

Figure 8.9. Comparison of experimental values with shrinking core model at pH = 8.6 and temperature = 52 °C.

CO_2 absorption using $Mg(OH)_2$ solution involves the multiple steps taking place in the three phases as summarized in the Introduction section. The rate of CO_2 absorption will be expressed with a combination of chemical equilibrium, mass-transfer correlations, and reaction kinetics, and will be governed by a rate-limiting step during the absorption process. This intrinsic dissolution kinetic expression in Eq. (8.12) will need to be incorporated into such an absorption model for the determination of CO_2 absorption rates. During this process, overall mass-transfer coefficients can also be determined by comparing model results with experimental results, which will eventually be used for the design of a CO_2 absorber.

9. Formation Kinetics of $MgCO_3$ Solid

Magnesium carbonate is a crystalline solid formed when magnesium hydroxide reacts with CO_2. Figures 9.1 and 9.2 show the equilibrium distribution of carbonate and magnesium species which are distributed as a function of pH.

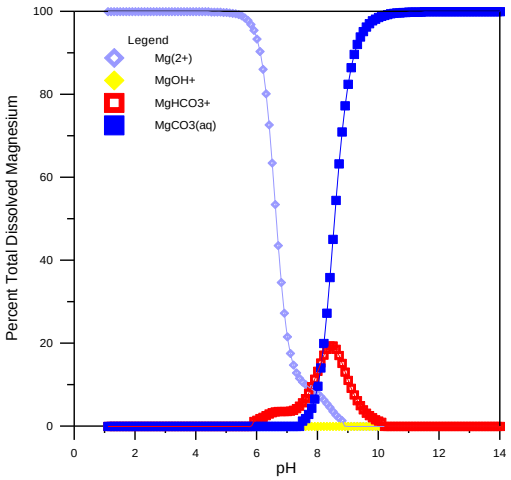

Figure 9.1. Distribution of dissolved magnesium species as a function of pH.

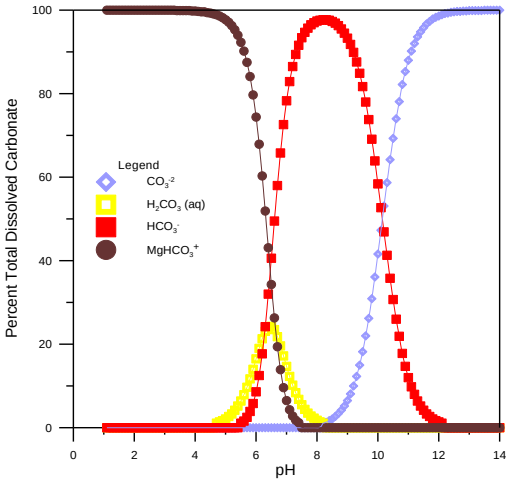

Figure 9.2. Distribution of dissolved carbonate species as a function of pH.

This was estimated by running MINEQL which is a chemical equilibrium modeling package for phase equilibrium determination. At a pH between 8 and 9 which is an optimum pH range for maximum magnesium bicarbonate formation, the ionic species are dominated by the bicarbonate ion. This would ensure that the formation of magnesium carbonate is minimized. Magnesium carbonate formation would reduce the lifetime for solvent in the chemical cycle between the absorber and the stripper. The complete release of CO_2 gas (i.e. ~52%) from the decomposition

of $MgCO_3$ would take place at >~400 °C, as shown in the following TGA diagram for pure $MgCO_3$.

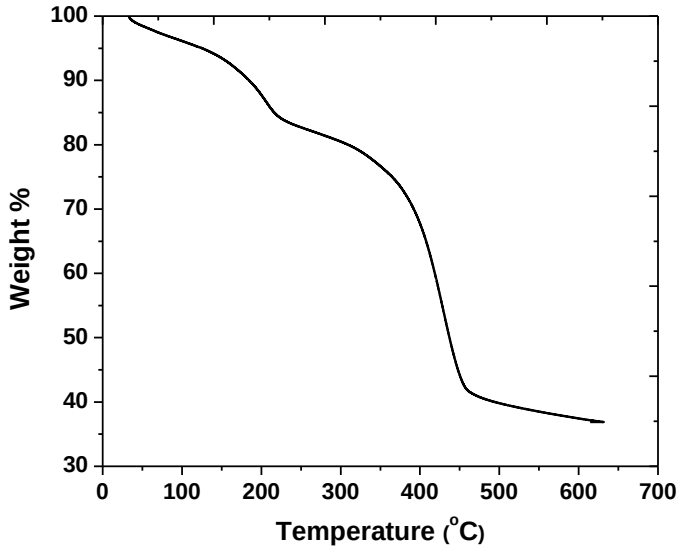

Figure 9.3. TGA curve for $MgCO_3$.

Previous studies estimated the crystal growth rate of calcium sulfite and calcium sulfite hemihydrate, which are the main reaction products of a flue gas desulphurization unit. Calcium sulfite crystallization affects several factors such SO_2 absorption, limestone dissolution, and solution composition, in a manner analogous to $MgCO_3$. Tseng and Rochelle et al. (Tseng and Rochelle 1986) studied the kinetics of calcium sulfite hemihydrate growth using a pH stat apparatus in an aqueous solution of pH 3.5 to 6.5 and found that the growth was a function of relative supersaturation and strongly inhibited by the dissolved sulfate. Boke et al. (Böke, Akkurt et al. 2004) developed a quantitative analysis using FTIR to distinguish between limestone($CaCO_3$), calcium sulfite hemihydrate ($CaSO_3 \cdot 0.5\ H_2O$) and gypsum($CaSO_4 \cdot 2H_2O$). The method employed in this study involved using TGA-MS and HCl titration to estimate the distribution of carbon among the solid and liquid phases. The effects of pH control and temperature on the kinetics of magnesium carbonate formation were investigated.

9.1 Experimental set-up and procedure

A 1 M $Mg(OH)_2$ solution was prepared by adding 29.15 g of $Mg(OH)_2$ to 500 mL water. A total inorganic concentration of X_{TIC} = 0.01 was simulated by adding 0.56 moles of sodium bicarbonate to the $Mg(OH)_2$ solution. Sodium bicarbonate ($NaHCO_3$) was used as a source of carbonate and bicarbonate ions to simulate CO_2 dissolution in the liquid phase. A pH stat with a set point of 8.6 was connected to a pump containing HCl of 1 N. The pH stat monitors the pH

value in the batch set-up and prevents it from going above 8.6. A temperature probe was used to monitor the temperature of the solution and a hot plate/stirrer was used to set the temperature of the batch system.

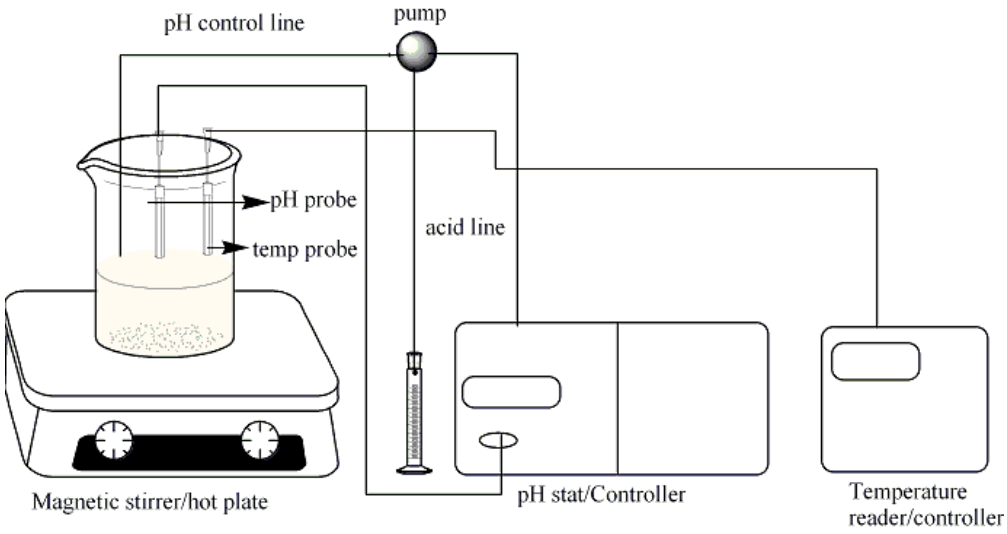

Figure 9.4. Experimental schematic used for $MgCO_3$ formation.

Samples were taken out at different time intervals and immediately centrifuged for the shortest possible time to separate the solid from the liquid. The liquid was filtered with a 0.45 μm filter and analyzed for liquid carbon concentration by HCl titration method. The solids were dried under vacuum at 60 °C for 24 hours until the solid became dry. The solids were then analyzed for carbon content using the TGA-MS.

9.2 Solid analysis using TGA-MS

The solid samples were analyzed for carbon content by using a Thermo gravimetric analyzer (TA Instruments TGA Q5000IR) coupled with a Mass Spectrometer (Pfeiffer-Vacuum Thermostar). Percent weight loss and detected mass spectra vs. temperature/time were used to quantify the CO_2 evolved from a solid sample. Oxygen gas was used as a carrier gas with a flow rate of 100 mL/min to ensure complete combustion with ~10–25 mg of sample. A ramp rate used was 5 °C/min up to a target temperature of 800 °C. The calibration curve was obtained using known samples of calcium oxalate powder. The calibration curves for CO_2 gas and the TGA-MS curves for a sample are shown in Figures 9.5–9.7, respectively.

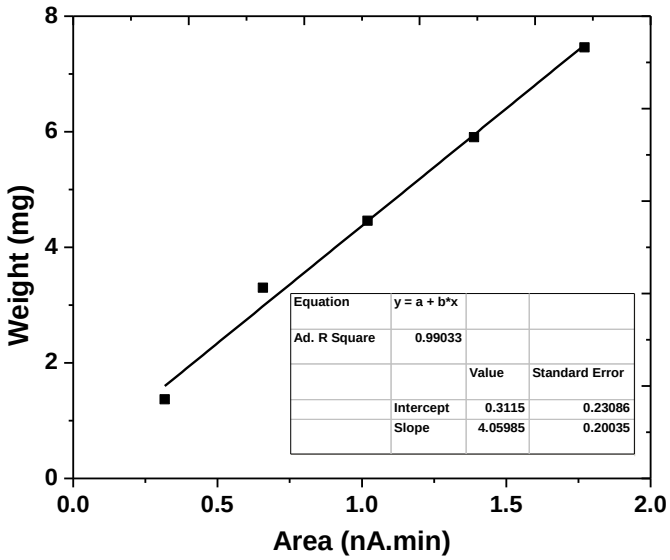

Figure 9.5 Calibration curve for CO_2 gas measurement using TGA-MS.

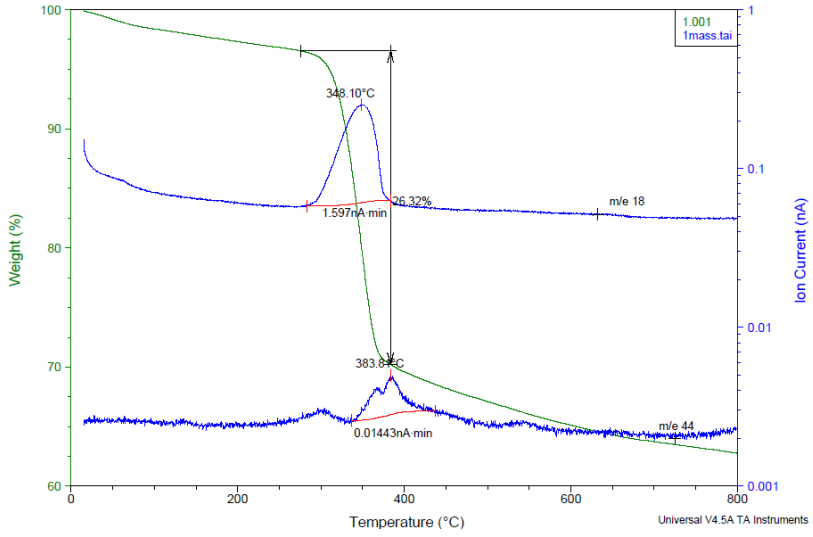

Figure 9.6 A TGA-MS curve for pH control and temperature 65 °C at 0 min.

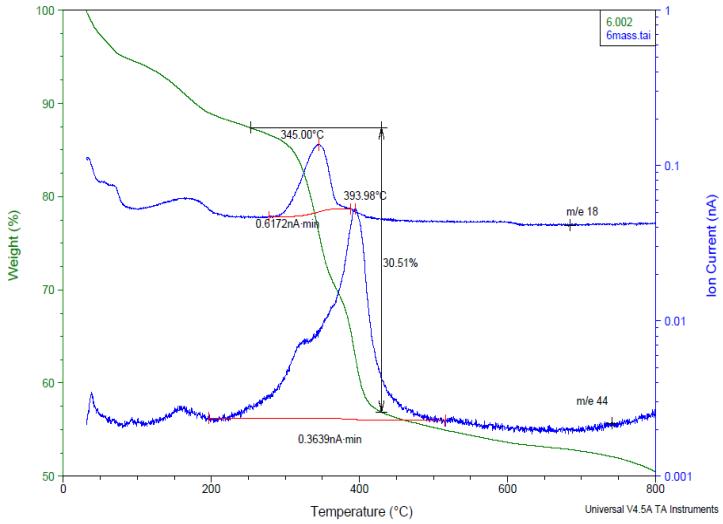

Figure 9.7 A TGA-MS curve for pH control and temperature 65 °C at 15 min.

9.3 Results and discussion

The mass balance tables with pH control using HCl and without pH control at three different temperatures are presented below. Bar graphs show the partitioning of the carbon species of bicarbonate ion in the liquid (HCO_3^-), carbonate ion in the liquid (CO_3^{2-}), and solid carbon over different time intervals.

9.3.1 Solid Formation at 52 °C

Table 9.1. Carbon mass balance obtained at 52 °C

Sample No	Time(min)	Carbon in CO_3^{2-} (g)	Carbon in HCO_3^- (g)	Solid phase Carbon(g)	Actual Mass Balance(g)
1	1	0.16	2.89	0.23	3.28
2	3	0.22	2.84	0.50	3.56
3	5	0.32	2.48	0.88	3.68
4	7	0.38	2.32	0.84	3.54
5	10	0.44	2.20	0.80	3.44
6	15	0.48	2.19	0.75	3.42

Theoretical: 3.36 g carbon input; and an error range of 2–8%

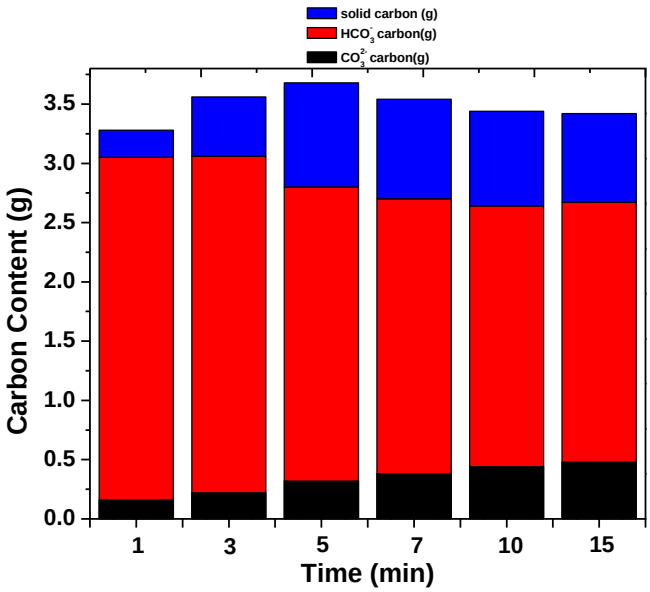

Figure 9.8. Carbon speciation with respect to time at 52 °C.

The mass balance summarized in Table 9.1 and the bar graphs shown in Figure 9.8 show an increase of carbon in the solid phase with time. A decrease in bicarbonate ion concentration from 1 to 15 min was ~20%. It is also shown that the carbonate ion concentration in the liquid phase increased with time.

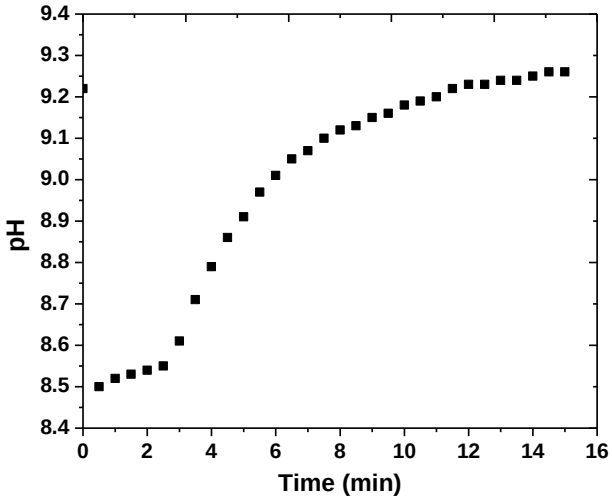

Figure 9.9. pH vs. time graph at 52 °C.

There was a decrease in an initial pH value of $Mg(OH)_2$ from ~10 to 9.2, due to an increase in temperature from 24 to 52 °C. The pH values quickly dropped in the beginning, because

sodium bicarbonate, being soluble in water, released H^+ ions and brought down the pH. Then the pH increased slowly until ~3.5 mins. In this region, the H^+ ions reacted with the OH^- ions released from the dissociation of $Mg(OH)_2$ and formed water. This region also included the initiation of solid carbon formation, which continued up to 10 min. After this period, the pH increased rapidly and went back up to the initial pH. This was mainly due to the dissolution of magnesium hydroxide, which released OH^- ions, thereby increasing the basicity of the solution.

9.3.2 Solid Formation at 65 °C

Table 9.2. Carbon mass balance obtained at 65 °C

Sample No	Time(min)	Carbon in CO_3^{2-} (g)	Carbon in HCO_3^- (g)	Solid phase Carbon(g)	Actual Mass Balance(g)
1	1	0.15	3.28	0.44	3.87
2	3	0.28	2.88	0.90	4.06
3	5	0.36	2.66	1.10	4.12
4	7	0.42	2.52	1.17	4.11
5	10	0.46	2.48	1.10	4.04
6	15	0.48	2.48	1.15	4.11

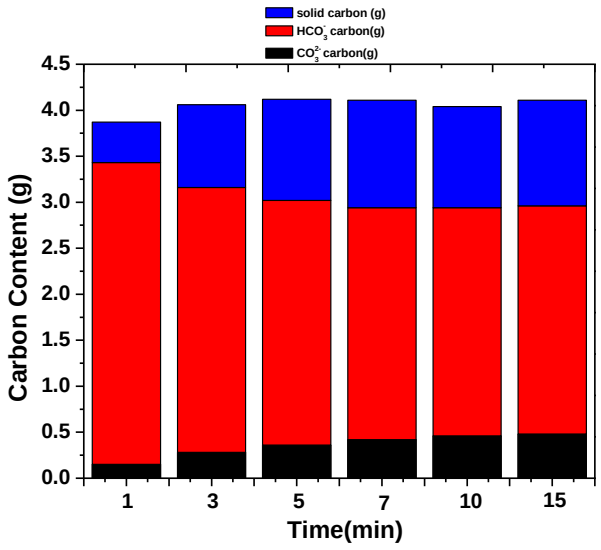

Figure 9.10. Carbon content vs. time at 65 °C.

An increase in temperature to 65 °C resulted in the accelerating the kinetics of solid carbon formation as seen in Figures 9.10 and Table 9.2. When compared to the sample taken at 3 min

for the experiment performed with the one at 52 °C, there was almost a 50% increase in the solid carbon formation for the experiment conducted at 65 °C. This effect was reduced during the entire experimental run and the percentage difference in the solid carbon formation came down to 34%, when the samples taken at 15 min were compared.

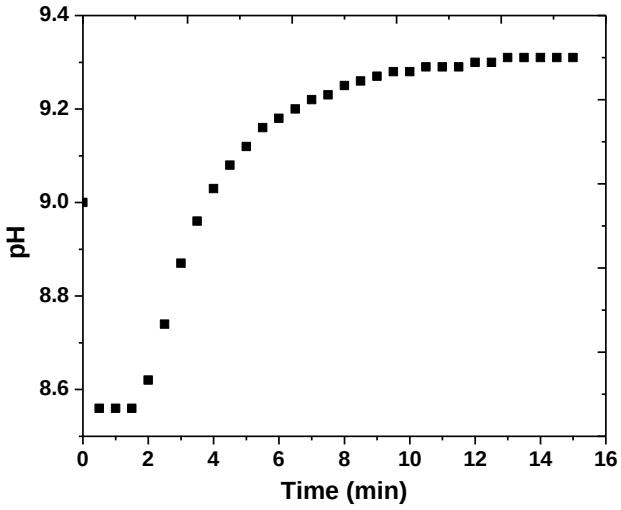

Figure 9.11. pH vs. time for no pH control at 65 °C.

When the temperature was raised from 52 to 65 °C, the initial pH value of the solution decreased from 9.2 to 9.0 as shown in Figure 9.11. The pH increase was achieved in a shorter period of time when compared at 52 °C. This is because the ionic reactions occurred almost instantaneously at the increased temperature.

9.3.3 Solid Formation at 25 °C

Table 9.3. Carbon mass balance obtained at 25 °C

Sample No	Time(min)	Carbon in CO_3^{2-} (g)	Carbon in HCO_3^- (g)	Solid phase Carbon(g)	Actual Mass Balance(g)
1	1	0.24	3.16	0.35	3.75
2	3	0.26	3.10	0.32	3.68
3	5	0.26	3.10	0.44	3.80
4	10	0.27	2.90	0.39	3.56
5	20	0.36	2.50	0.92	3.78
6	30	0.46	2.28	1.20	3.94

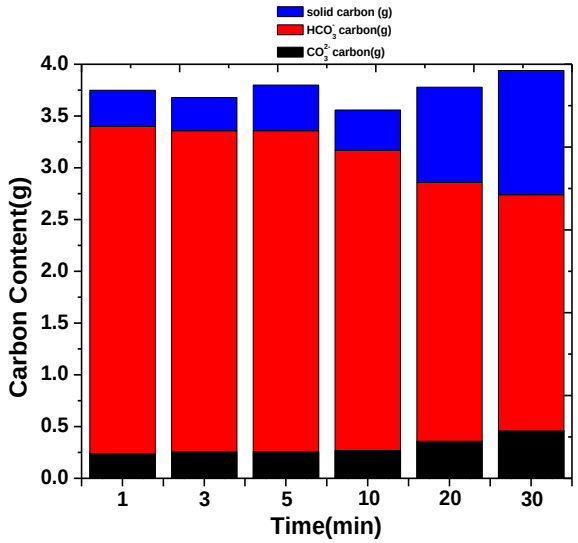

Figure 9.12. Carbon content vs. time for no pH control at 24 °C.

The rate of solid formation (Table 9.3 and Figure 9.12), when compared to the experiments run at elevated temperatures of 52 and 65 °C was slow. For example, the amount of solid carbon formed at 10 min was 64% less than solid carbon formed at 65 °C for the same time period.

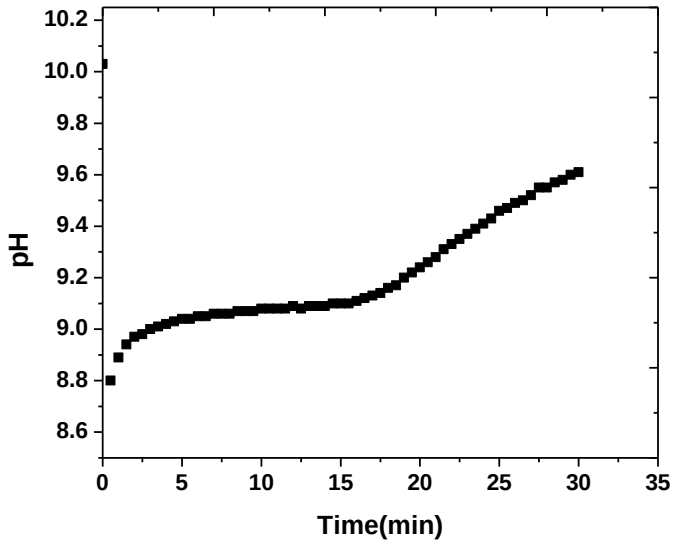

Figure 9.13. pH vs. time obtained at 25 °C.

The initial pH of $Mg(OH)_2$ slurry solution is ~10, and starts to drop due to the dissolution and equilibration of HCO_3^- in $NaHCO_3$ with CO_3^{2-} as shown in Figure 9.13. After some of

CO_3^{2-} is consumed to form $MgCO_3$ (which is warranted by a constant pH region between 5 and 20 min), OH^- starts to be released to return to the initial pH value of ~10.

10. Conclusions

A technical feasibility of using a magnesium hydroxide ($Mg(OH)_2$) solution for CO_2 capture in a coal-fired power plant has been evaluated. In comparison with a widely used MEA solvent, magnesium hydroxide solution poses a series of advantages for operation and handling as it is a non-toxic, odorless, non-flammable and less corrosive slurry. Some amount of magnesium hydroxide can be reclaimed from a limestone- and dolomite-based FGD unit.

Absorption experiments were conducted in a turbulent contact absorber (TCA) and a bubble column reactor using simulated flue gases at various operating conditions. The effects of CO_2 gas absorption were carefully evaluated with respect to parameters including liquid-to-gas ratio, residence time, magnesium hydroxide concentration, pressure drop, bed height, CO_2 gas partial pressure, bubble size, pH, and temperature. An n-CSTR model was developed to analyze the TCA absorption data. It was found that a TCA reactor used in this research can be adequately modeled when n=7. When TCA was used with a magnesium concentration ranging from 0.1 to 1 mol/L (M), a CO_2 gas removal efficiency significantly increased with an increase in magnesium hydroxide concentrations, indicating that liquid-side mass transfer is a controlling step. In the meantime, when a magnesium concentration higher than 1 M was used, a CO_2 gas removal efficiency was almost independent of the magnesium concentration, suggesting that a rate-limiting step shifts from the liquid to the gas phase. An overall mass-transfer coefficient for the TCA was determined at various L/G ratios for 0.1 and 1 M NaOH solutions. The values were found to be 0.006–0.008 and 0.014–0.018 kgmol/(m^3·sec·atm) at a L/G range of 10–30 L/m^3 for 0.1 and 1 M NaOH solutions, respectively. The L/G ratios used in the TCA was greater than those of packed tower and spray tower, but the TCA residence time was significantly shorter than sprayer tower and packed tower. However, overall the CO_2 gas removal performance of the TCA was ~<20% under the conditions, and thus the CO_2 absorber design needed to change.

In a bubble column absorber, the CO_2 gas removal efficiency depended on the gas residence time and the concentration of a $Mg(OH)_2$ solution. 0.1 M $Mg(OH)_2$ with a 9-sec gas residence time could achieve >90% CO_2 gas removal. An operating cost for the absorber highly depended on a liquid-to-gas (L/G) ratio. High CO_2 gas removal was demonstrated in a lab-scale experiment at a reasonable L/G ratio of 110 gal/1,000 acf. The CO_2 gas removal efficiency increased from 90 to 98% when the L/G ratio increased from 110 to 450 gal/1000 acf. Magnesium regeneration conditions were identified and a possible regeneration mechanism was found. $Mg(HCO_3)_2$ was quite soluble and reversible by temperature, but $MgCO_3$, when formed, is rarely soluble and energy intensive to regenerate. A temperature swing regeneration process has been shown to be effective in recovering CO_2 gas and regenerating $Mg(OH)_2$. The system could continuously maintain a 90% CO_2 gas capture efficiency and its desorption at 75 °C with ~0.008 L/sec of a fresh $Mg(OH)_2$ make-up flow rate.

A bubble column reactor model was also developed for the determination of a mass-transfer coefficient. The model incorporated the physical absorption of CO_2 gas into water, dissolution of $Mg(OH)_2$ solid particles, diffusion within the gas and liquid phases, and the chemical reactions of the ions. The overall mass-transfer coefficient was found to be a function of the hydrodynamic parameters, Henry's constant, CO_2 partial pressure in the gas phase, molecular diffusion coefficients, solid dissolution constant and temperature. The overall mass-transfer coefficient values ranged from 3.4×10^{-7} to 7.7×10^{-7} mol/(cm^3·atm·s) for 0.1 to 1 M $Mg(OH)_2$ solutions, and were comparable to those of MEA-based solutions. The film thickness was estimated to be 0.024 cm and was deemed to be reasonable.

The regeneration of a rich magnesium slurry solution is a key step to making the CO_2 gas removal process more efficient and sustainable. The regeneration includes the release of CO_2 gas from the rich solution and the recovery for a lean magnesium slurry solution. The desorption was studied under the temperatures of 70, 90, and 100 °C. It was observed that the CO_2 gas release rate from a rich magnesium solution increased with an increase in temperature. However, the formation of undesirable $MgCO_3$ solid was also accelerated with temperature, and has been identified as a major technical challenge for the magnesium-based system. A weakly basic ion exchange resin containing amine functional groups was also evaluated for the regeneration of a rich magnesium solution. However, the performance of the resin for the adsorption of bicarbonate ion was found to be insignificant.

The dissolution kinetics for magnesium hydroxide is one of the most important steps in the CO_2 scrubbing process. The rate of dissolution of $Mg(OH)_2$ was studied under different operating conditions using a pH stat apparatus. The dissolution process was modeled using a shrinking core model. The overall $Mg(OH)_2$ dissolution process was found to be controlled by the surface chemical reaction of $Mg(OH)_2$ with H^+ ions. The formation of $MgCO_3$ solid is an undesirable by-product in the CO_2 absorption process since the regeneration of $MgCO_3$ requires a large amount of energy input. The effect of temperature on $MgCO_3$ formation was investigated and the results showed that an increase in reaction temperature would lead to an increase in $MgCO_3$ formation.

From this study, >90% CO_2 gas removal using $Mg(OH)_2$ slurry solutions in a bubble column design was found to be feasible. However, the formation of $MgCO_3$ solids during the desorption step was found to be a major technical challenge. Although the undesirable $MgCO_3$ solids are separated, calcined, and re-slaked for the regeneration of $Mg(OH)_2$ slurry solutions, the energy required for the endothermic calcination process would be +28.2 kcal/(gmol $MgCO_3$) at ~400 °C. The exothermic slaking process will release the heat of -25 kcal/(gmol MgO). However, these two energies cannot be exchanged because the calcination step will require

high-temperature energy. Until this technical challenge is resolved, $Mg(OH)_2$-based CO_2 gas absorption is unlikely to be an alternative to the MEA-based CO_2 gas scrubbing technology.

This American Recovery and Reinvestment Act (ARRA) project has provided a great opportunity to engineering education in the field of carbon capture and sequestration for chemical and environmental engineering graduate students. Two chemical and environmental engineering graduate students were fully supported and a few other graduate students were partially supported during the project period. These students have participated in various and in-depth laboratory research activities in order to obtain fundamental experimental data and construct engineering models for the optimal design and operation of a CO_2 gas absorption technology. Some of these students have graduated and started to work as a trained workforce in the energy and environment area.

11. References

Abdel-Aal, E. A. (2000). "Kinetics of sulfuric acid leaching of low-grade zinc silicate ore." Hydrometallurgy **55**(3): 247-254.

Aydogan, S., M. Erdemoglu, et al. (2007). "Kinetics of galena dissolution in nitric acid solutions with hydrogen peroxide." Hydrometallurgy **88**(1-4): 52-57.

Böke, H., S. Akkurt, et al. (2004). "Quantification of CaCO3–CaSO3·0.5H2O–CaSO4·2H2O mixtures by FTIR analysis and its ANN model." Materials Letters **58**(5): 723-726.

Bird, R. B., W. E. Stewart, et al. (2002). Transport Phenomena, John Wiley & Sons, Inc.

Chen, J.-C., G.-C. Fang, et al. (2005). "Removal of carbon dioxide by a spray dryer." Chemosphere **59**(1): 99-105.

Chen, P.-C. (2012). Absorption of Carbon Dioxide in a Bubble-Column Scrubber, Greenhouse Gases - Capturing, Utilization and Reduction., InTech.

Chen, P.-C., W. Shi, et al. (2008). "Scrubbing of CO2 Greenhouse Gases, Accompanied by Precipitation in a Continuous Bubble-Column Scrubber." Industrial & Engineering Chemistry Research **47**(16): 6336-6343.

Cheng, L., T. Li, et al. (2013). "A mass transfer model of absorption of carbon dioxide in a bubble column reactor by using magnesium hydroxide slurry." International Journal of Greenhouse Gas Control **17**(0): 240-249.

Cooper, C. D. and F. C. Alley (2011). Air Pollution Control (A Design Approach), Waveland Press, Inc.

Fan, L.-S., K. Muroyama, et al. (1982). "Hydrodynamic characteristics of inverse fluidization in liquid—solid and gas—liquid—solid systems." The Chemical Engineering Journal **24**(2): 143-150.

Fan, L. S. (1989). Gas-liquid-solid fluidization engineering.

Fedoročková, A. and P. Raschman (2008). "Effects of pH and acid anions on the dissolution kinetics of MgO." Chemical Engineering Journal **143**(1–3): 265-272.

Fleischer, C., S. Becker, et al. (1996). "Detailed modeling of the chemisorption of CO2 into NaOH in a bubble column." Chemical Engineering Science **51**(10): 1715-1724.

Gao, X., R. T. Guo, et al. (2009). "Dissolution rate of limestone for wet flue gas desulfurization in the presence of sulfite." Journal of Hazardous materials **168**(2-3): 1059-1064.

Hövelmann, J., C. V. Putnis, et al. (2012). "Direct Nanoscale Observations of CO_2 Sequestration during Brucite [$Mg(OH)_2$] Dissolution." Environmental Science and Technology **46**(9): 5253-5260.

Herskowits, D., V. Herskowits, et al. (1990). "Characterization of a two-phase impinging jet absorber—II. Absorption with chemical reaction of CO2 in NaOH solutions." Chemical Engineering Science **45**(5): 1281-1287.

Javed, K. H., T. Mahmud, et al. (2010). "The CO2 capture performance of a high-intensity vortex spray scrubber." Chemical Engineering Journal **162**(2): 448-456.

Jung, K. S., T. C. Keener, et al. (2004). "A technical and economic evaluation of CO_2 separation from power plant flue gases with reclaimed $Mg(OH)_2$." Clean Technologies and Environmental Policy **6**(3): 201-212.

Kanai, Y., K.-i. Fukunaga, et al. "Mass transfer in molten salt and suspended molten salt in bubble column." Chemical Engineering Science(0).

Kuntz, J. and A. Aroonwilas (2009). "Mass-transfer efficiency of a spray column for CO2 capture by MEA." Energy Procedia **1**(1): 205-209.

Lani, B. W. (1998). Advanced ThioClear Process Testing. Final report to Ohio Coal Development Office, Dravo Lime Company and The Cincinnati Gas and Electric Company.

Levenspiel, O. (2007). Chemical Reaction Engineering, John Wiley & Sons, Inc.

Lindman, N. and D. Simonsson (1979). "On the application of the shrinking core model to liquid-solid reactions." Chemical Engineering Science **34**(1): 31-35.

Luo, X., A. Hartono, et al. (2011). "The study of numerical methods and validation of a heat and mass transfer model in CO2 -MEA system." Energy Procedia **4**(0): 1435-1442.

Maceiras, R., S. S. Alves, et al. (2008). "Effect of bubble contamination on gas–liquid mass transfer coefficient on CO2 absorption in amine solutions." Chemical Engineering Journal **137**(2): 422-427.

Maceiras, R., X. R. Nóvoa, et al. (2007). "Local mass transfer measurements in a bubble column using an electrochemical technique." Chemical Engineering and Processing: Process Intensification **46**(10): 1006-1011.

Muroyama, K. and L.-S. Fan (1985). "Fundamentals of gas-liquid-solid fluidization." AIChE Journal **31**(1): 1-34.

O'Neill, B. K., D. J. Nicklin, et al. (1972). "The hydrodynamics or gas-liquid contacting in towers with fluidised packings." The Canadian Journal of Chemical Engineering **50**(5): 595-601.

Pokrovsky, O. S. and J. Schott (2004). "Experimental study of brucite dissolution and precipitation in aqueous solutions: surface speciation and chemical affinity control." Geochimica et Cosmochimica Acta **68**(1): 31-45.

Raschman, P. and A. Fedoročková (2004). "Study of inhibiting effect of acid concentration on the dissolution rate of magnesium oxide during the leaching of dead-burned magnesite." Hydrometallurgy **71**(3–4): 403-412.

Raschman, P. and A. Fedoročková (2008). "Dissolution kinetics of periclase in dilute hydrochloric acid." Chemical Engineering Science **63**(3): 576-586.

Raschman, P. and A. Fedorockova (2006). "Dissolution of periclase in excess of hydrochloric acid: Study of inhibiting effect of acid concentration on the dissolution rate." Chemical Engineering Journal **117**(3): 205-211.

Rubia, M. D. L., A. García-Abuín, et al. (2010). "Interfacial area and mass transfer in carbon dioxide absorption in TEA aqueous solutions in a bubble column reactor." Chemical Engineering and Processing: Process Intensification **49**(8): 852-858.

Rutto, H. L. and C. Enweremadu (2011). "The Dissolution Study of a South African Magnesium Based Material from Different Sources using a pH-Stat." Chemical Industry & Chemical Engineering Quarterly **17**(4): 459-468.

Segall, R. L., R. S. C. Smart, et al. (1978). "Ionic Oxides -Distinction Between Mechanisms and Surface Roughening Effects in the Dissolution of Magnesium Oxide." Journal of the Chemical Society-Faraday Transactions 1 **74**: 2907-2912.

Sema, T., A. Naami, et al. (2012). "Comprehensive mass transfer and reaction kinetics studies of CO2 absorption into aqueous solutions of blended MDEA–MEA." Chemical Engineering Journal **209**(0): 501-512.

Shah, Y. T., B. G. Kelkar, et al. (1982). "Design parameters estimations for bubble column reactors." AIChE Journal **28**(3): 353-379.

Shih, S. M., J. P. Lin, et al. (2000). "Dissolution rates of limestones of different sources." Journal of Hazardous materials **79**(1-2): 159-171.

Siagi, Z. O. and M. Mbarawa (2009). "Dissolution rate of South African calcium-based materials at constant pH." Journal of Hazardous materials **163**(2-3): 678-682.

Smith, E. O., D. O. Swenson, et al. (1983). Lime FGD systems data book: second edition. Final report. Other Information: Portions are illegible in microfiche products**:** Medium: X; Size: Pages: 800.

Snoeyink, V. L. and D. Jenkins (1980). Water chemistry, Wiley.

Sun, B., Q. Zhou, et al. (2010). "Effect of particle size in a limestone-hydrochloric acid reaction system." Journal of Hazardous materials **179**(1–3): 400-408.

Tontiwachwuthikul, P., A. Meisen, et al. (1992). "CO2 absorption by NaOH, monoethanolamine and 2-amino-2-methyl-1-propanol solutions in a packed column." Chemical Engineering Science **47**(2): 381-390.

Treybal, R. E. (1967). Mass-transfer operations. New York,, McGraw-Hill.

Tseng, P. C. and G. T. Rochelle (1986). "Calcium Sulfite HemiHydate - Crystal-Growth Rate and Crystal Habit " Environmental Progress **5**(1): 5-11.

V. Bravo, R., R. F. Camacho, et al. (2002). "Desulphurization of SO_2–N_2 mixtures by limestone slurries." Chemical Engineering Science **57**(11): 2047-2058.

Visvanathan, C. and L. S. Leung (1985). "Design of a fluidized bed scrubber." Industrial & Engineering Chemistry Process Design and Development **24**(3): 677-683.

Vunjak-Novakovic, G. V., D. V. Vukovic, et al. (1987). "Hydrodynamics of turbulent bed contactors. 1. Operating regimes and liquid holdup." Industrial & Engineering Chemistry Research **26**(5): 958-966.

Vunjak-Novakovic, G. V., D. V. Vukovic, et al. (1987). "Hydrodynamics of turbulent bed contactors. 2. Pressure drop, bed expansion, and minimum fluidizing velocity." Industrial & Engineering Chemistry Research **26**(5): 967-972.

Wang, J., T. C. Keener, et al. (1998). "The Dissolution Rate of $Ca(OH)_2$ in Aqueous Solutions." Chemical Engineering Communications **169**(1): 167-184.

Wark, K. and C. F. Warner (1981). Air pollution: its origin and control.

Wogelius, R. A., K. Refson, et al. (1995). "Periclase Surface Hydroxylation during Dissolution." Geochimica et Cosmochimica Acta **59**(9): 1875-1881.

Wylock, C., A. Larcy, et al. (2010). "Direct numerical simulation of the transfer from spherical bubbles to and aqueous solutions with clean and fully contaminated interface." Colloids and Surfaces A: Physicochemical and Engineering Aspects **365**(1–3): 28-35.

Zhao, L., L. Sang, et al. (2009). "Aqueous Carbonation of Natural Brucite: Relevance to CO_2 Sequestration." Environmental Science and Technology **44**(1): 406-411.